UNICAMP

UNIVERSIDADE ESTADUAL DE CAMPINAS

Instituto de Matemática, Estatística e Computação Científica

LARYSSA ABDALA

Heart chamber modeling using Navier-Stokes equations

Modelo computacional de uma câmara do coração a partir das equações de Navier-Stokes

Campinas

2018

Laryssa Abdala

Heart chamber modeling using Navier-Stokes equations

Modelo computacional de uma câmara do coração a partir das equações de Navier-Stokes

Dissertação apresentada ao Instituto de Matemática, Estatística e Computação Científica da Universidade Estadual de Campinas como parte dos requisitos exigidos para a obtenção do título de Mestra em Matemática Aplicada.

Dissertation presented to the Institute of Mathematics, Statistics and Scientific Computing of the University of Campinas in partial fulfillment of the requirements for the degree of in Applied Mathematics.

Orientador: Carlos Eduardo Keutenedjian Mady

Coorientador: Maicon Ribeiro Correa

Este exemplar corresponde à versão final da Dissertação defendida pela aluna Laryssa Abdala e orientada pelo Prof. Dr. Carlos Eduardo Keutenedjian Mady.

Campinas

2018

Agência(s) de fomento e nº(s) de processo(s): FAPESP, 2016/19126-2; CAPES
ORCID: https://orcid.org/0000-0002-9461-5297

Ficha catalográfica
Universidade Estadual de Campinas
Biblioteca do Instituto de Matemática, Estatística e Computação Científica
Silvania Renata de Jesus Ribeiro - CRB 8/6592

Abdala, Laryssa, 1993-
Ab31h Heart chamber modeling using Navier-Stokes equations / Laryssa Abdala. – Campinas, SP : [s.n.], 2018.

Orientador: Carlos Eduardo Keutenedjian Mady.
Coorientador: Maicon Ribeiro Correa.
Dissertação (mestrado) – Universidade Estadual de Campinas, Instituto de Matemática, Estatística e Computação Científica.

1. Coração - Ventrículo esquerdo. 2. Método dos elementos finitos. 3. Exergia. I. Mady, Carlos Eduardo Keutenedjian, 1984-. II. Ribeiro Correa, Maicon, 1979-. III. Universidade Estadual de Campinas. Instituto de Matemática, Estatística e Computação Científica. IV. Título.

Informações para Biblioteca Digital

Título em outro idioma: Modelo computacional de uma câmara do coração a partir das equações de Navier-Stokes
Palavras-chave em inglês:
Heart - Left ventricle
Finite element method
Exergy
Área de concentração: Matemática Aplicada
Titulação: Mestra em Matemática Aplicada
Banca examinadora:
Carlos Eduardo Keutenedjian Mady [Orientador]
João Frederico da Costa Azevedo Meyer
Rogerio Gonçalves dos Santos
Data de defesa: 07-12-2018
Programa de Pós-Graduação: Matemática Aplicada

Dissertação de Mestrado defendida em 07 de dezembro de 2018 e aprovada pela banca examinadora composta pelos Profs. Drs.

Prof(a). Dr(a). CARLOS EDUARDO KEUTENEDJIAN MADY

Prof(a). Dr(a). JOÃO FREDERICO DA COSTA AZEVEDO MEYER

Prof(a). Dr(a). ROGERIO GONÇALVES DOS SANTOS

A Ata da Defesa, assinada pelos membros da Comissão Examinadora, consta no SIGA/Sistema de Fluxo de Dissertação/Tese e na Secretaria de Pós-Graduação do Instituto de Matemática, Estatística e Computação Científica.

A vocês que pariram a (minha) história.
Em especial à mamãe, vovó e Marcela.

Acknowledgements

Inicialmente, agradeço ao professor Cadu, orientador e sonhador. Foi quem plantou a semente dessa pesquisa e de ideais vêm florescendo em mim. Também foi a pessoa que me acolheu dentro da engenharia e me apoiou em decisões difíceis de diversas maneiras. Agradeço ao professor Maicon, por toda sua coragem e empenho. Foi quem compartilhou comigo experiências da análise numérica e de modelagem matemática, acompanhou de perto os desafios computacionais e se dedicou muito durante essa jornada. Além disso, para que este projeto fosse idealizado, busquei ouvir os conselhos do professor Alberto Saa, à quem sou extremamente grata por toda atenção, pelas conversas sinceras e sugestões. Vocês confiaram no meu trabalho e foram essenciais para que esse projeto acontecesse, tenho total admiração por vocês. O presente trabalho foi realizado com apoio da Coordenação de Aperfeiçoamento de Pessoal de Nível Superior - Brasil (CAPES) - Código de Financiamento 001 e com o apoio da Fundação de Amparo à Pesquisa do Estado de São Paulo (FAPESP) - Processo 2016/19126-2. Reconheço a importância desses órgãos que possibilitaram que eu me dedicasse integralmente à essa pesquisa.

Agradeço às contribuições do Felipe Silva e do Fábio Santiago, os quais me indicaram pacientemente os caminhos que percorreram para que eu encontrasse trilhas amigáveis em direção à compreensão da teoria e dos códigos. Ao Matheus Borges que teve enorme contribuição na revisão de literatura, na análise termodinâmica e trouxe vida a esse ventrículo, obrigada! Também o olhar do professor Roberto Aussas, que me ajudou a conectar ideias importantes. Aos membros da banca, professores Joni e Rogério, sou muito grata pelas discussões, correções e estímulo para o desenvolvimento do trabalho. Aproveito para valorizar todas as professoras e professores que passaram em minha vida, os quais foram fundamentais no direcionamento da minha dedicação aos estudos e contemplação da complexidade da vida, em especial Thiago Bortoli.

Às minhas maiores fontes de inspiração humana e de amor: mãe, Ma, vovó e Vivi. Foram vocês que me ensinaram o que é amar. Compartilhamos

momentos intensos e aprendemos o que é mais valioso na vida juntas. Gratidão também pelo amor do meu irmão, Felipe e pelo amparo da família Silva. Agradeço por ter nascido tão perto de vocês.

Usando as palavras de vovó, sou iluminada por ter pessoas maravilhosas na vida, que são parte da família que eu escolhi. Agradeço às primas Carol, Priscila, Aleska e respectivas famílias pelo carinho e acolhimento. Também agradeço imensamente à tia Vera, que acredita em mim desde o início dessa jornada, desde o dedinho mindinho. Agradeço à Daniela, minha conselheira acadêmica e espiritual: você me deu ferramentas inestimáveis e me emprestou seu olhar precioso. Às minhas irmãs de coração Júlia, Marinas, Gabriela, Jéssica, Isabela, Laísa, Stephania: muito obrigada por me apoiarem e escolherem cultivar esse laço lindo de amizade. À Melissa e Joy, que são companheiras de busca do autoconhecimento, agradeço por todo amor, vocês tornam a vida mais bonita e divertida. À pessoa que traz abraços sorridentes e me dá colo até por wi-fi, Gigis. E à Stellinha, amiga fiel. Agradeço também ao meu companheiro, professor, fonte de amor e confiança, Tiago, por construir esse caminho junto comigo e me apoiar.

Aos amigos do IMECC e do IFGW que acompanham essa jornada acadêmica desde 2011 e fizeram-na mais humana, em especial Abner, Arthur, Daniel, Dvd, Mel, Nina e Vlad, meu muito obrigada! E aos atuais fortes companheiros de estudos e diversão: Rodolfo, Paula, Cristian, Felipe e Demácio, os quais tornaram os dias mais cafeinados e engraçados. Aos amigos que Bergen trouxe na bela paisagem: Dan, Anna, Fábio, Jade, Thaynara, Raíssa, Yoli, Alfonso. Vocês trouxeram calor pros tempos gélidos e continuam acalentando minha vida. Adoro pensar no quão improvável foi nosso encontro e, em mesma medida, a força que isso nos trouxe.

Fazer um mestrado é tanto sobre conhecimento profissional quanto pessoal. Portanto, agradeço à Ana Carolina por ter caminhado junto comigo nas terapias, pelo suporte e gentileza. Infelizmente não é possível citar todas as pessoas que passaram pelos meus caminhos e o tornaram mais bonito, mas não tenho dúvida que aprendi e sou um pouco de cada um de vocês. Aos que compartilham os meus sonhos, agradeço por apreciarem o brilho dos meus olhos e apoiarem este trabalho, que sabem o quanto importa para mim. Sou grata à existência de todos vocês e por ter o prazer de dividir o mesmo tempo e espaço que vocês nesse Universo.

“The cosmos is within us. We are made of star-stuff.
We are a way for the universe to know itself."
(Carl Sagan)

Resumo

No presente estudo, é apresentado um modelo computacional bidimensional do fluxo sanguíneo em uma câmara de um coração saudável humano, com a particular descrição do ventrículo esquerdo. O domínio e a malha utilizados para a representação espacial são fixos, o sangue é considerado como sendo um fluido newtoniano incompressível e a variação do volume da câmara é simulada a partir da introdução de uma função de capacitância que é dependente do espaço e do tempo. Apesar de ser feita a hipótese de incompressibilidade do sangue, a função de capacitância confere ao sistema uma forma diferencial que se assemelha às equações de Navier-Stokes para fluidos compressíveis. Inicialmente é descrita a resolução do Problema de Stokes incompressível a partir do emprego de um Método de Elementos Finitos Misto estável, baseado no método de Galerkin. Em seguida, o modelo numérico é evoluído para abordar o problema completo. A partir daí, são apresentadas simulações numéricas obtidas a partir de um código elaborado em Fortran 90. Os resultados indicam uma boa aderência com a literatura médica. A partir desse modelo, foi possível aplicar as Leis da Termodinâmica a partir do qual obteve-se uma eficiência de Segunda Lei equivalente a 71%.

Palavras-chave: Coração; Ventrículo esquerdo; Navier-Stokes; Método dos Elementos Finitos; Análise exergética.

Abstract

In the present study, a bidimensional computational model of blood flow through a chamber of a healthy human heart, with a particular description of the left ventricle, is presented. The domain and mesh used for spatial representation are fixed, blood is considered to be an incompressible Newtonian fluid, and the chamber volume variation is simulated from the introduction of a capacitance function that is space and time-dependent. Although the hypothesis of blood incompressibility is made, the capacitance function gives the system a differential form that resembles the Navier-Stokes equations for compressible fluids. Initially, the resolution of the incompressible Stokes Problem is described using a stable Mixed Finite Element Method, based on the Galerkin method. Then, the numerical model is evolved to address the whole problem. Subsequently, numerical simulations obtained from a code elaborated in Fortran 90 are presented. The results indicate good adherence with the medical literature. From this model, it was possible to apply the Laws of Thermodynamics, from which a Second Law efficiency equivalent to 71% was obtained.

Keywords: Heart; Left ventricle; Navier-Stokes; Finite Element Method; Exergy analysis.

List of Figures

List of Tables

Contents

1 Introduction

From the Second Law of Thermodynamics, Boltzmann theorized that nature is moving toward the thermal death of the universe. This seems to contradict the paradigm, associated with Darwin, that biological systems are in increasing complexity and organization (MURPHY; O'NEAL, 1997). In 1943, Schrödinger gave lectures entitled "What Is Life?" at Trinity College in Dublin, in which he focused on subjects such as the nature of heredity and the thermodynamics of living beings. Schrödinger explored Boltzmann's ideas, speculating that living organisms seemed to defy the Second Law of Thermodynamics if they are considered as closed systems, but, appealing to the non-equilibrium thermodynamics, the scientist recognized that organisms are open systems, that take energy from the external environment, causing them to obtain a higher internal level of organization. Thus, from a global perspective, the system's entropy continues to increase, causing the Second Law of Thermodynamics not to be violated (MURPHY; O'NEAL, 1997). This work has initiated a new way of thinking about life and, consequently, biological systems. Moreover, it has boosted the studies on this imbalance and what causes the generation of entropy in the body. Later Prigogine e Wiame (1946) obtained that all living things tend to a state of minimum entropy generation. Therefore, it is possible to conclude that when there is a disequilibrium of the body with the environment (biological things have higher order) the entropy generation is higher.

Biological and physiological systems

An exponent study of the thermodynamics of the human body was done in 1948 by H.H. Pennes (PENNES, 1948). The author performed experiments in order to evaluate the applicability of the heat and mass transfer concepts to the forearm. To this aim it was evaluated the blood flow rate and local energy transfer associated with the metabolism. Pennes (1948) aimed at a quantitative analysis of the relationship between arterial blood and tissue temperatures for the first time,

and have originated the perfusion term introduced in the energy balance. This model treats the vessels as part of a continuum, however, the temperature depends on the position, *i.e.*, it is not a fixed representative one. In this sense, the work of Chen e Holmes (1980) summarized that the temperature of blood and tissue comes to an equilibrium, not in capillaries as previously assumed, but between the terminal arterial branches and the precapillary arterioles. This work also reveals that, the heat transfer of larger vessels must be considered individually, not in a continuum formulation. Finally, Chen e Holmes (1980) proposed a bio-heat equation including Pennes's perfusion term, and contributions of local blood perfusion velocity and thermal conductivity.

Blick e Stein (1977) presented an analysis of the heart through the First Law of Thermodynamics, which considers the control volume that surrounds the heart's exterior, but passing through the veins and arteries that are responsible for the carrying the blood in and out of the heart. This remarkable work has determined the "order of magnitude" of several modes of energy conversion processes performed by the heart, such as, kinetic energy, potential energy, flow work, heat transfer, metabolic energy, endothermic chemical reaction. Furthermore, the authors included energy due to shear work, Ohmic heating, and compression of intrathoracic structures. Nevertheless, they found these terms to be negligible when compared to the other forms of work. Figure 1 illustrates the obtained results of the energy balance obtained by the authors. It is important to point out that other means of energy were calculated, but their order are lower than the ones presented in the figure. Finally, Blick e Stein (1977) have calculated the heart efficiency as approximately 13%, which is in accordance with the medical literature.

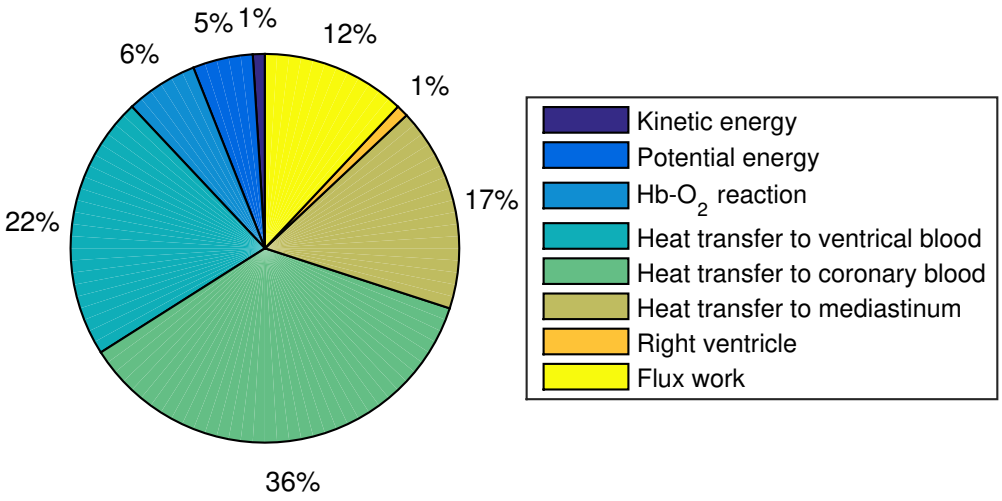

Figure 1 – Energy sinks of the normal human heart from Blick e Stein (1977).

From the combination of the First and Second Laws of Thermodynamics, Szargut (2005) was one of the first researchers to look to the concept of exergy, which is the amount of work that a certain system can perform when it is brought into thermodynamic equilibrium (mechanical, thermal, and chemical) with the environment, and, in (SZARGUT, 2005) the author adds that

> *"[...] one field may be very interesting for young researchers, namely the analysis of exergy losses in living organisms. For example, the exergetic efficiency of the vegetation of plants is very low. The reasons behind such an effect are worth investigating. In the human body, too, the exergy losses are considerable. In a mature organism, the total exergy of food is transformed into the considerably smaller exergy of waste materials or heat rejected into the environment. The reduction of these losses might be interesting from the point of view of food consumption and human health."*

On the other hand, isolated cells and small organisms have no circulatory system. Its metabolic functions can be satisfied by means of diffusion and convection processes of solutes from the external environment to the internal one. As the size and complexity of organisms increase, a circulatory system becomes an evolutionary need. This system is responsible for the distribution of nutrients between cells and

the collection of residues (BORON; BOULPAEP, 2012). According to Fung (1997), blood flow theory is the most advanced theme of biomechanics, with roots in the study of Aristotle and Huangti, with contributions from leading scientists such as Galileo, Descartes, Euler, Poiseuille, Helmholtz, and many others. This system, in particular, has been modeled by analogy to circuit physics, fluid mechanics, and thermodynamics.

The heart, in turn, has been modeled using different approaches, depending on the focus and purpose given to the research. When speaking of heart-blood dynamics, which is a fluid-structure interaction problem, the approach through the immersed boundary method (PESKIN, 2002; GAO et al., 2014) allows the volume of the cardiac chambers to vary over time. In this case, the conservation laws for blood are generally described by the incompressible Navier-Stokes equations. In the present work, the domain and the mesh are defined to be fixed, therefore, a mathematical artifice is introduced to change the heart chamber volume, namely, the capacitance function. Consequently, although the hypothesis of blood incompressibility is used, there is a compressible behavior associated with the Navier-Stokes equations.

Another important aspect of the blood flow through a heart chamber is the mechanical behavior of the fluid. A liquid containing suspended particles may have a non-Newtonian shift, which becomes significant when the particle size is large in relation to the channel through which the fluid is flowing. In the human body, this is true when blood flows through small arterioles and capillaries (OTTESEN; OLUFSEN; LARSEN, 2004), however, in the case of the heart, the Newtonian hypothesis is reliable and stems from the fact that the viscosity can be considered constant, since the cavities and valves are large in relation to the diameters of the cells. Moreover, the shear stresses are high enough so that the viscosity can be considered independent of them (OTTESEN; OLUFSEN; LARSEN, 2004).

Numerical Modeling

Towards attempting to understand physiological problems, which are often expressed mathematically through partial differential equations, scientists look for solutions of their governing equations. However, for most of these problems,

the equations can not be solved analytically, and it is necessary to use numerical approximations. In this sense, the approximate solutions can be constructed from different types of discretization. There is a vast literature on this area of study and, among other possibilities (PESKIN, 2002; GAO et al., 2014), the finite element method (FEM) is the one chosen in this work for the spatial discretization of the problem while the finite difference method (FDM) is left to the time discretization. In particular, the FEM has the advantage of being able to solve problems with complex geometries, besides being able to predict the order of approximation of the spaces used for such analyses. The basis of the numerical methodology employed in this work stands on a Stable Galerkin Mixed Finite Element Method for the Stokes problem (BREZZI; FORTIN, 2012). More specifically, the locally conservative approximation that uses biquadratic nodal interpolations for velocity and linear approximations for pressure is discussed. This choice of elements, so called Q_2P_1, is not standard, since it is not usual to approximate the pressure in a quadrilateral mesh using the space P_1 (BREZZI; FORTIN, 2012). An important observation about this element is the possibility of using a local (mapped) pressure approximation or a global (unmapped) pressure one, combined with a mapped velocity approach. Although both approaches satisfy the inf-sup condition (BOFFI; GASTALDI, 2002), in the former case, where the pressure is calculated in the parent domain, the convergence of the solution does not reach its optimal order in L^2, whereas the global approach turns out to be optimally convergent (BOFFI; BREZZI; FORTIN, 2013). Then, having these results in mind, the global pressure approach is considered for the rest of the numerical simulations of this dissertation, including the final one.

Thermodynamics

In order to perform the thermodynamic analysis it is necessary to calculate the metabolism in both energy (M) and exergy (B_M) bases. Mady e Oliveira (2013) uses stoichiometry of the reactions of oxidation, the consumption of carbohydrates, protein and lipids to calculate metabolic exergy, using two control volumes that represent the human body. The authors conclude that the approximation $B_M \approx M$, as previously reported in (BATATO et al., 1990), is valid

in basal conditions and may also hold during physical activities. Later on, Henriques et al. (2017) formulated the exergy analysis for healthy hearts and ones with aortic stenosis, considering the relation of the intensity of the stenosis and the destroyed exergy. Due to a lack of experimental data, only the left heart was analyzed. Then, the right side was accounted considering that the fraction of destroyed exergy of the heart right and left sides was equal to the fraction of its workloads (HENRIQUES et al., 2017).

Organization of the dissertation

This Master Dissertation in Applied Mathematics Program is inserted in this multidisciplinary context with the objective of proposing a computational model of a heart ventricle based on theories of fluid mechanics and thermodynamics. The purpose is to create a collaborative work that allows the use of the mathematical and numerical modeling in the thermodynamic analysis of the complex circulatory system. All the numerical codes were developed in Fortran 90 by the authors, based on the works (CORREA, 2006; CORREA; LOULA, 2009). More specifically, in this dissertation, an introduction to the mathematical model of a heart chamber is presented and a numerical model of the left ventricle is proposed. Several numerical results, from the simplified and Classical Stokes problem to a modification of the incompressible Navier-Stokes equations, are presented. Finally, a model of a heart chamber that takes into account heat exchanges with the rest of the body is presented. The energy equation is solved in its integral form in order to give a clue of its necessity in this phenomenological problem. As a closing equation, it is possible to apply the Second Law of Thermodynamics and the exergy analysis of the system, based on (MADY et al., 2012) and (MADY; OLIVEIRA, 2013).

The organization of the text follows. The heart chamber bidimensional model developed to simulate the volume variation is presented in Chapter 2, together with the governing equations: mass and linear momentum conservation, that are a modified version of the Navier-Stokes equations. The references used to stem the simplifying hypothesis are also mentioned in this part of the text, such as the reason for the blood being considered Newtonian in the present model. At the end of this chapter, the left ventricle idealized geometry is described. Numerical models of

steady-state forms of the Navier-Stokes equations are presented in Chapter 3, while Chapter 4 is entirely devoted to the description of the numerical methodology for the solution of the modified Navier-Stokes equations. Some numerical experiments are performed, in order to evaluate qualitatively the results before proceeding to the next step, which is the parameter calibration to simulate an idealized human left ventricle. In the sequence, Chapter 5 presents some cardiac cycle volume-pressure pairs for a healthy human left ventricle, and other parameters such as the blood viscosity, and specific mass. Using this data from the literature and the geometry presented at the end of Chapter 2, simulations using the authors' code are performed and its results are shown, including the PV-diagram and the velocity fields.

Putting the outcomes from the previous chapters together, the Thermodynamics analysis for the left ventricle is carried out in Chapter 6. The First and Second Laws of Thermodynamics are explored, and from them, it is performed the exergy analysis, which has a prior role in the efficiency analysis of a thermodynamic system. Then, the final considerations and conclusions are presented in Chapter 7, including possible improvements that can be implemented in future works. At last, the Appendix A give details on the implementation of the numerical simulations, such as details on the solver used to approximate the solution of the linear systems, and other simulation features.

2 Physical and Mathematical models

The aim of this chapter is to present a mathematical bidimensional model for the blood flow throughout a heart chamber. In order to introduce the volume change of the chamber, a capacitance function is defined, leading to a modified version of the incompressible Navier-Stokes equations. Additionally, the references used to state the simplifying hypotheses are presented, and the medical parameters used to represent the geometry of a human left ventricle are included in the last section.

2.1 Mathematical model

Let $I = [0, T]$ be a time interval and $\Omega \subset \mathbb{R}^2$, with boundary $\Gamma = \partial\Omega$ and unit outward normal $\mathbf{n}$, be a domain under which a fluid, with constant dynamic viscosity $\mu \in \mathbb{R}_{>0}$ and specific mass $\rho \in \mathbb{R}_{>0}$, flows with velocity $\boldsymbol{u} = (u, v) : \Omega \times I \to \mathbb{R}^2$ and hydro-static pressure $p : \Omega \times I \to \mathbb{R}$. Since the fluid is considered incompressible, a usual simplification in the modeling of blood flow in the heart chambers that will be discussed bellow, and the bidimensional domain Ω of the cavity is fixed in time, changes in volume are modeled through the introduction of a capacitance function $\varphi : \Omega \times I \to \mathbb{R}_{>0}$, which characterizes the amount of fluid mass at each point of the domain, and depends on the spatial coordinates $\boldsymbol{x} \in \Omega$ and time $t \in I$. It may also have a dependence on the hydro-static pressure p, however, this case will not be considered in this work.

In other words, each point in the domain has a weight — in the mathematical sense — at each time frame t, that can be associated with the amount of mass there. It means that every integral that takes into account the specific mass, must consider the distribution of φ over the domain. Thus, the mass contained in the domain can be expressed as

$$M = \int_\Omega \rho\varphi(\boldsymbol{x}, t) d\Omega, \tag{2.1}$$

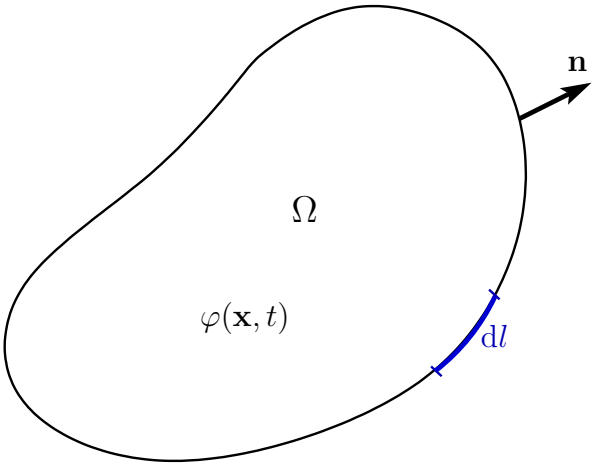

Figure 2 – Domain Ω.

where $\varphi(\boldsymbol{x}, t) = \varphi_0 + \tilde{\varphi}(\boldsymbol{x}, t)$, and $\varphi(\boldsymbol{x}, t) > 0$ for all $\boldsymbol{x} \in \Omega$ and $t \in I$. Therefore, for each $\boldsymbol{x} \in \Omega$ and $t \in I$, $\varphi(\boldsymbol{x}, t)$ assumes positive values that can be fewer or greater than the constant φ_0, indicating that the point can store less or more mass. Figure 3 illustrates what would represent the function φ in the case of a fluid flowing through a pipe of variable diameter in a one-dimensional flow model in the axis x.

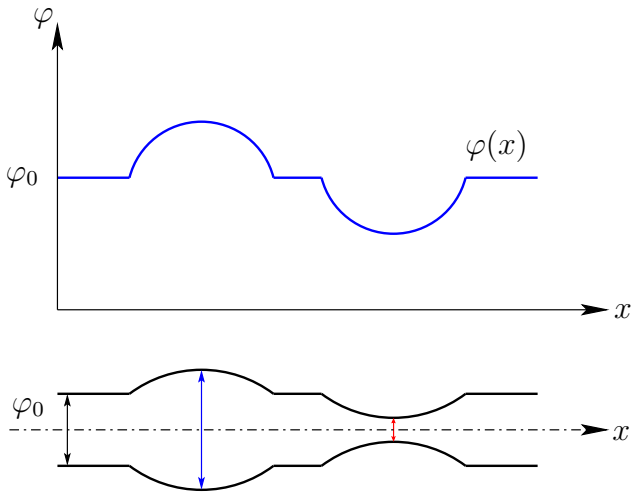

Figure 3 – One-dimensional analogy of the capacitance function φ.

Wherever possible $\varphi(\boldsymbol{x}, t)$ will be denoted simply as φ.

2.1.1 Governing equations

In this subsection, the governing equations that compose the mathematical model are presented. In this work it is assumed that the energy equation does not affect the mass conservation equation and does not influence the physical properties of the fluid (density, viscosity, etc.), however, it is assumed that the flow affects the energy equation of the system. Thus, the balance equations studied here are the equation of conservation of mass and the equation of conservation of linear momentum, under the assumption of isothermal conditions. The central hypotheses of the thermodynamic model are discussed in Chapter 6.

2.1.1.1 Conservation of mass

Consider the mass of the system shown in Figure 2, and the mass flow rate through it, represented, respectively, by

$$M = \int_{\Omega} dM = \int_{\Omega} \rho\varphi d\Omega \tag{2.2}$$

and

$$\dot{m} = \int_{\partial\Omega} \rho \boldsymbol{u} \cdot \boldsymbol{n} \varphi dl = \int_{\Omega} \boldsymbol{\nabla} \cdot (\rho \boldsymbol{u}) \varphi d\Omega, \tag{2.3}$$

where $\partial\Omega$ is the boundary of Ω. From the Reynolds transport theorem, one gets

$$\int_{\Omega} \left(\frac{\partial(\rho\varphi)}{\partial t} + \boldsymbol{\nabla} \cdot (\rho\varphi \boldsymbol{u}) \right) d\Omega = 0. \tag{2.4}$$

Since the equation (2.4) holds for all Ω, it turns out that the law of conservation of mass inside the cavity can be described as

$$\frac{\partial(\rho\varphi)}{\partial t} + \boldsymbol{\nabla} \cdot (\rho\varphi \boldsymbol{u}) = 0. \tag{2.5}$$

2.1.1.2 Conservation of momentum

Consider that the domain Ω (shown in Figure 2) is also the control volume (CV) of the actual problem. Then, the linear momentum, and moment flow rate within the CV can be written, respectively, as

$$P = \int_{\Omega} \rho \boldsymbol{u} \varphi d\Omega, \tag{2.6}$$

and

$$\dot{P} = \int_{\partial\Omega} (\rho \boldsymbol{u})\boldsymbol{u} \cdot \boldsymbol{n}\varphi dl = \int_{\partial\Omega} [(\rho \boldsymbol{u}) \otimes \boldsymbol{u}]\boldsymbol{n}\varphi dl = \int_{\Omega} \boldsymbol{\nabla} \cdot (\varphi\rho \boldsymbol{u} \otimes \boldsymbol{u}) d\Omega. \tag{2.7}$$

Consequently, considering that there are no forces acting on the fluid, the equation of conservation of momentum can be written as

$$\int_{\Omega} \left[\frac{\partial(\varphi\rho \boldsymbol{u})}{\partial t} + \boldsymbol{\nabla} \cdot (\varphi\rho \boldsymbol{u} \otimes \boldsymbol{u}) \right] d\Omega = \boldsymbol{0}. \tag{2.8}$$

Recalling that

$$\boldsymbol{\nabla} \cdot (\varphi\rho \boldsymbol{u} \otimes \boldsymbol{u}) = \boldsymbol{\nabla} \cdot (\boldsymbol{u} \otimes \varphi\rho \boldsymbol{u}) = \boldsymbol{u}\boldsymbol{\nabla} \cdot (\varphi\rho \boldsymbol{u}) + (\boldsymbol{\nabla}\boldsymbol{u})(\varphi\rho \boldsymbol{u}), \tag{2.9}$$

it turns out that Equation (2.8) can be rewritten as

$$\int_{\Omega} \left[\boldsymbol{u} \frac{\partial(\varphi\rho)}{\partial t} + \varphi\rho \frac{\partial \boldsymbol{u}}{\partial t} + \boldsymbol{u}\boldsymbol{\nabla} \cdot (\varphi\rho \boldsymbol{u}) + (\boldsymbol{\nabla}\boldsymbol{u})(\varphi\rho \boldsymbol{u}) \right] d\Omega = \boldsymbol{0}. \tag{2.10}$$

And using the Equation of conservation of mass (2.4), it yields

$$\int_{\Omega} \varphi\rho \left(\frac{\partial \boldsymbol{u}}{\partial t} + (\boldsymbol{\nabla}\boldsymbol{u})\boldsymbol{u} \right) d\Omega = \boldsymbol{0}. \tag{2.11}$$

On the other hand, the terms corresponding to the forces acting on the fluid are split as the contribution of the body forces and of the forces of contact. The first one being represented by

$$\int_{\partial\Omega} \rho \boldsymbol{f} \varphi d\Omega, \tag{2.12}$$

and the contact forces being expressed as

$$\int_{\partial\Omega} \boldsymbol{t} dl = \int_{\partial\Omega} \boldsymbol{\sigma}\boldsymbol{n} dl = \int_{\Omega} \boldsymbol{\nabla} \cdot \boldsymbol{\sigma} d\Omega, \tag{2.13}$$

where $\boldsymbol{t} = (t_1, t_2) = \boldsymbol{\sigma}\boldsymbol{n}$ is the traction vector.

Therefore, taking external forces into account, Equation (2.10) becomes

$$\int_{\Omega} \left[\varphi \frac{\partial \boldsymbol{u}}{\partial t} + \varphi(\boldsymbol{\nabla}\boldsymbol{u})\boldsymbol{u} \right] d\Omega = \int_{\Omega} \left[\varphi \boldsymbol{f} + \frac{1}{\rho} \boldsymbol{\nabla} \cdot \boldsymbol{\sigma} \right] d\Omega. \tag{2.14}$$

Eventually, since equation (2.14) holds for every Ω, the conservation of linear momentum can be expressed in the differential form:

$$\varphi \frac{\partial \boldsymbol{u}}{\partial t} + \varphi(\boldsymbol{\nabla}\boldsymbol{u})\boldsymbol{u} = \varphi \boldsymbol{f} + \frac{1}{\rho} \boldsymbol{\nabla} \cdot \boldsymbol{\sigma}. \tag{2.15}$$

2.2 Heart chamber model

Henriques et al. (2017) used the model of the heart proposed in (HENRIQUES; MADY; OLIVEIRA-JUNIOR, 2016): a model of steady-state and continuous behavior for the organ and each atrium-ventricle pair to be a cavity. In addition, the authors considered that each part of the heart has only one entry and one exit with cross-sectional areas equivalent to the sum of the cross-sectional areas of the real arteries and veins that connect to the respective part of the heart. The scheme is represented in Figure 4. The exergy balance takes into consideration the left and right workloads of the heart.

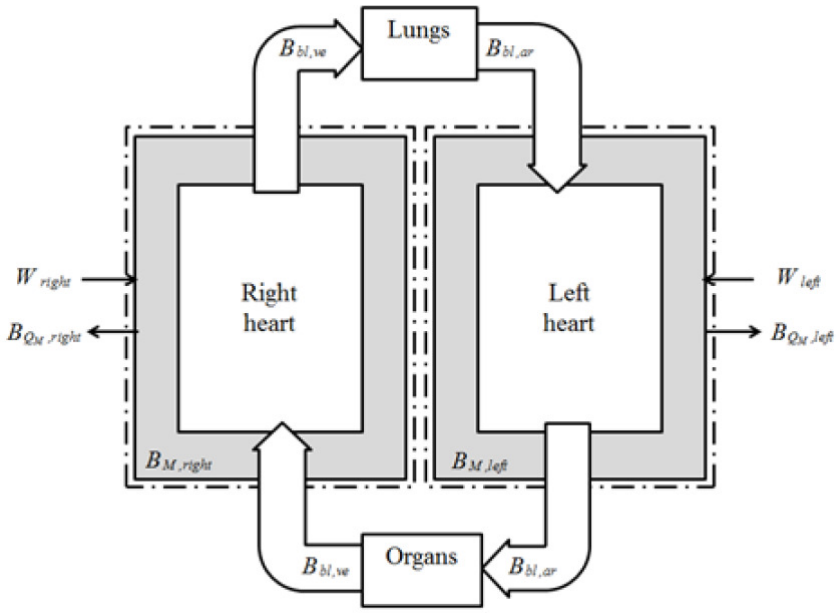

Figure 4 – Human heart model by Henriques, Mady e Oliveira-Junior (2016).

According to Ottesen, Olufsen e Larsen (2004), the mechanical behavior of a liquid containing suspended particles may have a non-Newtonian shift, which becomes significant when the particle size is large in relation to the channel through which the fluid is flowing. In the human body this is true for small arterioles and capillaries. In addition, Saltzman (2009) states that the presence of proteins and

high concentration of red cells in the blood contributes to its high viscosity — compared to water, for example.

However, in larger arteries, veins, and cavities one can assume that the blood flow is isotropic, Newtonian and incompressible (HUO; KASSAB, 2010). The hypothesis of being Newtonian stems from the fact that the viscosity can be considered constant, since the diameter of the arteries and large veins are large in relation to the diameters of the cells. Moreover, because the shear stresses are high enough that the viscosity can be considered independent of them (OTTESEN; OLUFSEN; LARSEN, 2004). Since in this work the focus is not on microcirculation, it is assumed that the blood has Newtonian behavior.

In this dissertation, a simplified model for the left ventricle of the human heart that can be straightforwardly extended to a model for the other heart cavities is proposed. It is expected that further extensions of this model allow the representation of more general models of the human heart, such as the one proposed in (HENRIQUES; MADY; OLIVEIRA-JUNIOR, 2016). The next subsections show the references used to establish simplifying hypothesis to evolve the geometry of the left heart ventricle.

2.2.1 Modified Navier-Stokes equations

From the Subsection 2.1.1 the blood flow through a cavity can be modeled by the equations (2.16).

$$\begin{aligned} \varphi \boldsymbol{\nabla} \cdot \boldsymbol{u} + \boldsymbol{u} \cdot \boldsymbol{\nabla} \varphi &= -\frac{\partial \varphi}{\partial t}, \\ \varphi \frac{\partial \boldsymbol{u}}{\partial t} + \varphi (\boldsymbol{\nabla} \boldsymbol{u}) \boldsymbol{u} &= \varphi \boldsymbol{f} + \frac{1}{\rho} \boldsymbol{\nabla} \cdot \boldsymbol{\sigma}. \end{aligned} \tag{2.16}$$

Moreover, since the fluid has a Newtonian behavior (as explained in the previous section), the constitutive law for Newtonian fluids holds:

$$\boldsymbol{\sigma} = -p\boldsymbol{I} + 2\mu\boldsymbol{\epsilon}(\boldsymbol{u}), \tag{2.17}$$

in which $\boldsymbol{\sigma}$ is the Cauchy stress tensor, and

$$\boldsymbol{\epsilon}(\boldsymbol{u}) = \frac{1}{2}(\boldsymbol{\nabla}(\boldsymbol{u}) + \boldsymbol{\nabla}(\boldsymbol{u})^T) \tag{2.18}$$

is the rate of strain tensor. Then, the equation (2.16) is rewritten as:

$$\begin{aligned} \varphi \boldsymbol{\nabla} \cdot \boldsymbol{u} + \boldsymbol{u} \cdot \boldsymbol{\nabla} \varphi &= -\frac{\partial \varphi}{\partial t}, \\ \varphi \frac{\partial \boldsymbol{u}}{\partial t} + \varphi(\boldsymbol{\nabla} \boldsymbol{u})\boldsymbol{u} &= \varphi \boldsymbol{f} - \frac{1}{\rho}\boldsymbol{\nabla} p + \frac{2\mu}{\rho}\boldsymbol{\nabla} \cdot \boldsymbol{\epsilon}(\boldsymbol{u}). \end{aligned} \tag{2.19}$$

Equations (2.19) will be referred to as the modified Navier-Stokes equations because, although the fluid is incompressible, the equations are similar to the Navier-Stokes equations for compressible fluids (they are not the same because the constitutive equation is the one for incompressible fluids).

2.2.2 Geometry

Consider that the referred heart cavity is the human left ventricle. The idealization of the domain is illustrated in Figure 5, which considers that there are only one inflow and one outflow pathways. Since, for a healthy individual, the mitral valve area (MVA) is about $4 - 6\text{cm}^2$ (OMRAN; ARIFI; MOHAMED, 2011), and the aortic valve area (AVA) of a healthy individual is around $3 - 4\text{cm}^2$ (GARCIA; KADEM, 2006), this model sets the following parameters to the left ventricle:

- MVA $= 5.0$ cm^2;
- AVA $= 3.5$ cm^2;
- Domain dimensions of the Left Ventricle (LV) $= (4 \times 8)\text{cm}^2$;
- Average capacitance function height $= 2.8$cm.

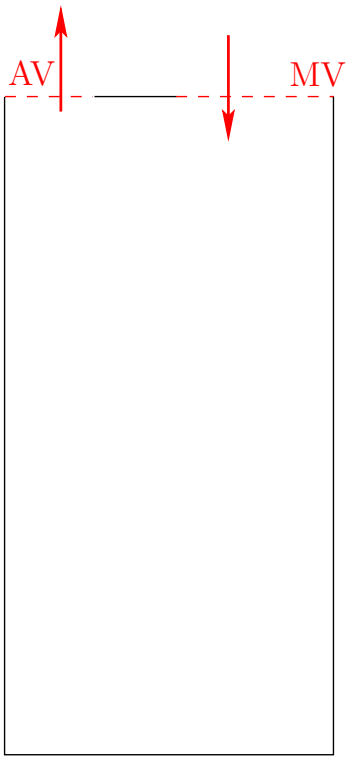

Figure 5 – Left ventricle model.

Since the mitral valve (MV) and the aortic valve (AV) are defined to be on the upper edge of the domain, the capacitance function is maintained constant $\varphi = \varphi_0$ on this part of the boundary. The same is assumed for the lower edge.

3 Finite element formulations of steady-state problems

In this chapter, the definitions and notations which will be used throughout this work are introduced, such as the choice of solution and approximation spaces for the incompressible Stokes problem. Its resulting mixed problem approximation is discussed by means of Galerkin FEM, and some relevant theoretical results for the development of the numerical method are also presented. In the last section, the incompressible Stokes problem is explored numerically from computational simulations, providing insights to numerical approaches to even more complex problems. Finally, we do one more step towards to the Navier-Stokes equations, introducing the Oseen problem, that contains an advection term.

3.1 Definitions and notations

Let Ω be a closed and limited subset of $\mathbb{R}^2$. Denote by $\partial\Omega$ the adequate boundary of Ω, *i.e.*, $\partial\Omega = \bar{\Omega} \setminus \Omega$, and $\Gamma_D, \Gamma_N \subset \partial\Omega$ denote the part in which the Dirichlet, and Neumann boundary conditions are imposed, respectively, with $\partial\Omega = \Gamma_D \cup \Gamma_N$. Firstly, we must define relevant spaces.

Definition 1 (Hilbert Spaces)**.** *For each $m \in \mathbb{N}$, $H^m(\Omega, \mathbb{R})$ will denote the Hilbert scalar field space of order m in Ω, which can be defined as*

$$H^0(\Omega, \mathbb{R}) \equiv L^2(\Omega, \mathbb{R}) := \{v; ||v||^2 < +\infty\},$$

and if $m \geq 1$, then

$$H^m(\Omega, \mathbb{R}) := \{v \in H^{m-1}(\Omega, \mathbb{R}); \frac{\partial^m v}{\partial x_1^{\alpha_1} \partial x_2^{\alpha_2}} \in L^2(\Omega, \mathbb{R}) \quad \forall \boldsymbol{\alpha} = (\alpha_1, \alpha_2) \in \mathbb{N}^2$$
$$with \quad |\boldsymbol{\alpha}| = \alpha_1 + \alpha_2 = m\}$$

being the derivatives taken in the sense of distributions. Particularly,

$$H_0^1(\Omega, \mathbb{R}) := \{v; v \in H^1(\Omega, \mathbb{R}), v|_{\partial\Omega} = 0\}.$$

Then the inner product and the norm that will be used onward can be defined:

Definition 2 (L^2 Inner product and norm)**.** *Let C be a limited subset of Ω. The inner product of $u, w \in L^2(C, \mathbb{R})$ is defined as*

$$(u, w)_C := \int_C uwd\boldsymbol{x}.$$

And when $u = (u, v), w = (w, z) \in L^2(C, \mathbb{R}^2)$

$$(\boldsymbol{u}, \boldsymbol{w}) := (u, w)_C + (v, z)_C.$$

Furthermore, the inner product for tensors $\boldsymbol{T}, \boldsymbol{S} \in L^2(C, \mathbb{R}^{2\times 2})$ is defined as

$$(\boldsymbol{S}, \boldsymbol{T}) := \sum_{i=1}^{2}\sum_{j=1}^{2}(S_{ij}, T_{ij})_C,$$

where the indexes ij indicate the tensor coordinate ij.

If $C = \Omega$ then the index will be implicit and dropped $(\cdot, \cdot) = (\cdot, \cdot)_\Omega$. Moreover, the definition of norm in L^2 derives from the definition of inner product defined above for each case. Then, if $v \in L^2(\Omega, \mathbb{R})$,

$$||v|| = ||v||_{L^2(\Omega,\mathbb{R})} = (v, v)^{1/2}.$$

The next definition is an important concept from the Fluid Mechanics theory, and it is widely used to predict flow patterns.

Definition 3 (Reynolds number)**.** *The Reynolds number of the flow (Re_L), is an dimensionless number defined as:*

$$Re_L = \frac{\rho u_{av} L}{\mu}, \tag{3.1}$$

in which ρ in the specific mass, u_{av} is a typical velocity (e.g. the average one), L is the characteristic linear dimension, and μ is the dynamic viscosity of the fluid.

3.2 Stokes Problem

Consider the general model and physical variables defined in Section 2.1. The incompressible Stokes problem is a particular case of the Navier-Stokes equations presented in Chapter 2, which take into consideration some simplifying hypotheses (CORREA, 2006):

- The flow is stationary, that is,
$$\frac{\partial \boldsymbol{u}}{\partial t} = \mathbf{0}; \tag{3.2}$$
- The flow is slow, *i.e.*, the viscous forces predominate in relation to those of inertia, in other words, the Reynolds number is low. Thus, the nonlinear term of the linear momentum conservation equation can be neglected;
- The specific mass ρ is constant.

As a consequence of these hypotheses, the conservation laws are simplifications of Equations (2.19), which can be rewritten as

$$\begin{aligned} \frac{1}{\rho}\boldsymbol{\nabla}\cdot\boldsymbol{\sigma} &= -\varphi\boldsymbol{f}; \\ \varphi\boldsymbol{\nabla}\cdot\boldsymbol{u} + \boldsymbol{u}\cdot\boldsymbol{\nabla}\varphi &= 0. \end{aligned} \tag{3.3}$$

Thus, the problem described by Equations (3.4) will be called general Stokes problem.

$$\begin{aligned} 2\mu\boldsymbol{\nabla}\cdot\boldsymbol{\epsilon}(\boldsymbol{u}) - \boldsymbol{\nabla}p &= -\varphi\rho\boldsymbol{f} && \text{in} && \Omega; \\ \varphi\boldsymbol{\nabla}\cdot\boldsymbol{u} + \boldsymbol{u}\cdot\boldsymbol{\nabla}\varphi &= 0 && \text{in} && \Omega; \\ \boldsymbol{u} &= \bar{\boldsymbol{u}} && \text{over} && \Gamma_D; \\ \boldsymbol{p} &= \bar{\boldsymbol{p}} && \text{over} && \Gamma_N. \end{aligned} \tag{3.4}$$

When $\varphi = 1$, Equations (3.3) turn out to be

$$\begin{aligned} 2\mu\boldsymbol{\nabla}\cdot\boldsymbol{\epsilon}(\boldsymbol{u}) - \boldsymbol{\nabla}p &= -\rho\boldsymbol{f} && \text{in} && \Omega; \\ \boldsymbol{\nabla}\cdot\boldsymbol{u} &= 0 && \text{in} && \Omega; \\ \boldsymbol{u} &= \bar{\boldsymbol{u}} && \text{over} && \Gamma_D; z \\ \boldsymbol{p} &= \bar{\boldsymbol{p}} && \text{over} && \Gamma_N. \end{aligned} \tag{3.5}$$

which will be called the classical Stokes problem.

3.2.1 Galerkin method

In the Galerkin method, it is assumed that the test functions belong to the same Hilbert space as the solutions, *i.e.*, $\boldsymbol{w}, \boldsymbol{u} \in \mathcal{U}$ and $q, p \in \mathcal{P}$ (BREZZI; FORTIN, 2012; CIARLET, 1978). In the following, this approach is used and, for simplicity, Dirichlet boundary conditions are homogeneous over $\partial\Omega$. In this way, the chosen function spaces are

$$\mathcal{U} = \{\boldsymbol{u} \in H_0^1(\Omega, \mathbb{R}^2)\} \tag{3.6}$$

for velocity, and

$$\mathcal{P} = \{p \in L^2(\Omega, \mathbb{R}); (p, 1)_\Omega = 0\} \tag{3.7}$$

for pressure.

3.2.1.1 Variational formulation

Multiplying the first equation of (3.4) by $q \in \mathcal{P}$, taking the inner product of the second one with $\boldsymbol{u} \in \mathcal{U}$, and integrating both on the domain Ω, one obtains the variational formulation:

Find $(\boldsymbol{u}, p) \in \mathcal{U} \times \mathcal{P}$ satisfying

$$\begin{aligned} 2\mu \int_\Omega \boldsymbol{\epsilon}(\boldsymbol{u}) : \boldsymbol{\epsilon}(\boldsymbol{w}) d\Omega - \int_\Omega p \boldsymbol{\nabla} \cdot \boldsymbol{w} d\Omega = \rho \int_\Omega \varphi \boldsymbol{f} \cdot \boldsymbol{w} d\Omega + \int_{\partial\Omega} \boldsymbol{t} \cdot \boldsymbol{w} dl, \\ \int_\Omega (\varphi \boldsymbol{\nabla} \cdot \boldsymbol{u} + \boldsymbol{u} \cdot \boldsymbol{\nabla}\varphi)\, q d\Omega = \int_\Omega 0 q d\Omega, \end{aligned} \tag{3.8}$$

for all $\boldsymbol{w} \in \mathcal{U}$, and $q \in \mathcal{P}$. The vector $\boldsymbol{t} = \boldsymbol{\sigma}\boldsymbol{n}$ is a traction vector.

Then, equation (3.8) can be written in the abstract form as

$$\begin{aligned} a(\boldsymbol{u}, \boldsymbol{w}) + b(\boldsymbol{w}, p) &= f(\boldsymbol{w}), \qquad \forall \boldsymbol{w} \in \mathcal{U}, \\ d(\boldsymbol{u}, q) &= g(q), \qquad \forall q \in \mathcal{P}, \end{aligned} \tag{3.9}$$

where $a(\cdot, \cdot) : \mathcal{U} \times \mathcal{U} \to \mathbb{R}$ and $b(\cdot, \cdot) : \mathcal{U} \times \mathcal{P} \to \mathbb{R}$ are bilinear forms, $f(\cdot) : \mathcal{U} \to \mathbb{R}$

and $g(\cdot) : \mathcal{P} \to \mathbb{R}$ are continuous linear functionals such that:

$$a(\boldsymbol{u}, \boldsymbol{w}) = 2\mu \int_\Omega \boldsymbol{\epsilon}(\boldsymbol{u}) : \boldsymbol{\epsilon}(\boldsymbol{w}) d\Omega \tag{3.10}$$

$$b(\boldsymbol{w}, p) = -\int_\Omega p \boldsymbol{\nabla} \cdot \boldsymbol{w} d\Omega, \tag{3.11}$$

$$d(\boldsymbol{u}, q) = \int_\Omega (\varphi \boldsymbol{\nabla} \cdot \boldsymbol{u} q + \int_\Omega \boldsymbol{u} \cdot \boldsymbol{\nabla} \varphi q) d\Omega \tag{3.12}$$

$$f(\boldsymbol{w}) = \rho \int_\Omega \varphi \boldsymbol{f} \cdot \boldsymbol{w} d\Omega + \int_{\partial\Omega} \boldsymbol{t} \cdot \boldsymbol{w} dl \tag{3.13}$$

$$g(q) = \int_\Omega 0 q d\Omega = 0. \tag{3.14}$$

Observe that it follows from the equation of conservation of mass (2.5) that $g \equiv 0$, which physically means that there is no source nor sinks of blood inside the ventricle.

The variational formulation for the classical Stokes problem (Equation (3.5)) is therefore represented by Equations (3.15).

$$\begin{aligned} a(\boldsymbol{u}, \boldsymbol{w}) + b(\boldsymbol{w}, p) &= f(\boldsymbol{w}), \qquad \forall \boldsymbol{w} \in \mathcal{U}, \\ b(\boldsymbol{u}, q) &= -g(q), \qquad \forall q \in \mathcal{P}. \end{aligned} \tag{3.15}$$

Since, the classical problem is a particular case of the general one, the variational formulation for the general Stokes problem (3.9) are solved in a finite dimensional context using classical Galerkin FEM, which will be carried out in Subsection 3.2.2.

3.2.2 Galerkin Approximation

In this subsection, the definitions of the mesh and the approximation spaces shall be provided. Let $\{\mathcal{T}_h\}$ be a decomposition of Ω in open subsets $\mathcal{T}_h = E$ known as elements, such that the domain closure $\bar{\Omega} = \lim_{h \to 0} \bigcup_{E \in \mathcal{T}_h} \bar{E}$. The elements E must be non-overlapping and the boundary ∂E of an element must be C^1 by parts. Index h represents the characteristic length, *i.e.*, the maximum diameter of the family of elements of Ω, over which the approximation spaces are taken (HUGHES, 2000).

Dimensional finite subspaces of H^1 are usually built from the mapping of polynomials defined in a standard element $\hat{E}$ — also called as parent domain — to each element E of the mesh $\mathcal{T}_h$. See Figure 6.

Definition 4 (Approximation spaces)**.** *Let*

$$\bar{\mathbb{P}}_k(E,\mathbb{R}) = span\{x_1^i x_2^{k-i}; i = 0,1,\ldots,k\}$$

be the set of homogeneous polynomials in E and

$$\mathbb{P}_k(E,\mathbb{R}) = \oplus_{n=0}^{k}\bar{\mathbb{P}}_n(E,\mathbb{R}) = span\{x_1^i x_2^j; i,j = 0,1,\ldots,k; i+j \leq k\}$$

be the space of polynomials in E of degree $k \geq 0$. Additionally, let

$$\mathbb{P}_{k,s}(E,\mathbb{R}) = span\{x_1^i x_2^j; i = 0,1,\ldots,r; j = 0,1\ldots,s\}$$

be the space spanned by the tensor product of two spaces $\mathbb{P}_k(E,\mathbb{R})$; if $r = s$, it will be represented as $\mathbb{Q}_k(E,\mathbb{R}) \equiv \mathbb{P}_{k,k}(E,\mathbb{R})$.

The spaces corresponding to vector polynomials in $\mathbb{R}^2$, such that each entry is in $\bar{\mathbb{P}}_n(E,\mathbb{R}), \mathbb{P}_n(E,\mathbb{R})$, and $\mathbb{P}_{k,s}(E,\mathbb{R})$ are denoted by $\bar{\mathbb{P}}_k(E,\mathbb{R}^2), \mathbb{P}_n(E,\mathbb{R}^2)$, $\mathbb{P}_{k,s}(E,\mathbb{R}^2)$ respectively.

As in the Classical Galerkin FEM, the local solutions are built in finite dimensional spaces (BREZZI; FORTIN, 2012; CIARLET, 1978) correspondent to $\mathcal{U}$ and $\mathcal{P}$, which are denoted, respectively, as $\mathcal{U}_h$ and $\mathcal{P}_h$.

Since, for non-affine meshes, the approximation of pressure affects the results for velocity, non-affine transformations are made from the standard element to the global one, which affects the optimal convergence of the approximations (ARNOLD et al., 2001a). An element that appears naturally for the actual case is Q_2Q_1 with discountinuous Q_1, nevertheless, that is not a stable element for the Stokes problem, then the approximation spaces of Equation (3.16) were proposed as a cure for the instability (BOFFI; BREZZI; FORTIN, 2013).

$$\begin{aligned} \mathcal{U}_h &= \{\boldsymbol{u_h} \in \mathcal{U}; \quad \boldsymbol{u_h}|_E \in \boldsymbol{Q}_E(\mathbb{Q}_2(\hat{E},\mathbb{R}^2)) \quad \forall E \in \mathcal{T}_h\} \\ \mathcal{P}_h &= \{p_h \in \mathcal{P}; \quad p_h|_E \in \mathbb{P}_1(E,\mathbb{R}^2) \quad \forall E \in \mathcal{T}_h\}. \end{aligned} \tag{3.16}$$

The approximation space $\mathcal{U}_h \times \mathcal{P}_h$ to which the approximate solution $(\boldsymbol{u_h}, p_h)$ belongs shall be denoted simply as Q_2P_1 which, for the classical Stokes Problem (Equation (3.15)) approximated in a quadrilateral mesh satisfies the following conditions:

1. Continuity of $a(\cdot,\cdot)$ and $b(\cdot)$: there exist constants $M_1, M_2 \in \mathbb{R}_{>0}$ such that

$$|a(\boldsymbol{u}_h, \boldsymbol{w}_h)| \leq M_1 ||\boldsymbol{u}_h||_{\mathcal{U}_h} ||\boldsymbol{w}_h||_{\mathcal{U}_h} \qquad \forall \boldsymbol{u}_h, \boldsymbol{w}_h \in \mathcal{U}_h$$
$$|b(\boldsymbol{u}_h, q_h)| \leq M_1 ||\boldsymbol{u}_h||_{\mathcal{U}_h} ||q_h||_{\mathcal{P}_h} \qquad \forall \boldsymbol{u}_h \in \mathcal{U}_h, \forall q_h \in \mathcal{P}_h$$

2. K-Coercitivity of $a(\cdot,\cdot)$: there are constants $\alpha_1, \alpha_2 > 0$ such that

$$\sup_{\boldsymbol{w_h} \in K} \frac{|a(\boldsymbol{u}_h, \boldsymbol{w}_h)|}{||\boldsymbol{w}_h||_{\mathcal{U}_h}} \geq \alpha_1 ||\boldsymbol{u}_h||_{\mathcal{U}_h} \qquad \forall \boldsymbol{u}_h \in K$$
$$\sup_{\boldsymbol{w_h} \in K} \frac{|a(\boldsymbol{u}_h, \boldsymbol{w}_h)|}{||\boldsymbol{w}_h||_{\mathcal{U}_h}} \geq \alpha_2 ||\boldsymbol{w}_h||_{\mathcal{U}_h} \qquad \forall \boldsymbol{w}_h \in K$$

   where

$$K = \{\boldsymbol{u}_h \in \mathcal{U}_h; b(\boldsymbol{u}_h, q_h) = 0, \quad \forall q_h \in \mathcal{P}_h\}$$

3. Ladyszhenskaya-Babuška-Brezzi (LBB) condition: there exists a constant $\gamma > 0$ such that

$$\inf_{q_h \in \mathcal{P}_h} \sup_{\boldsymbol{w}_h \in \mathcal{U}_h} \frac{b(\boldsymbol{w}_h, q_h)}{||q_h||_{\mathcal{P}_h} ||\boldsymbol{w}_h||_{\mathcal{U}_h}} = \gamma > 0, \qquad \forall q_h \in \mathcal{P}_h.$$

Consequently, it follows from Brezzi's theorem (BREZZI, 1974), that there is a unique solution for the classical Stokes problem (Equation (3.15)).

3.2.3 Calculations on parent and real elements

Furthermore, in order to map the coordinates, the pressure and velocity from the parent element $\hat{E}$ to each real element E of Ω, some relevant mappings are introduced:

Definition 5. *Let $\boldsymbol{T}_{\hat{E}\to E} : \hat{E} \to E$ be a biquadratic isomorphism of two limited convex quadrilaterals in $\mathbb{R}^2$. In the present context, $\hat{E} = [-1, 1]^2 \subset \mathbb{R}^2$.*

Define the function $Q_{\hat{E}\to E} : L^2(\hat{E},\mathbb{R}) \to L^2(E,\mathbb{R})$ *such that a scalar field* ϕ_1 *in* $\hat{E}$ *is mapped into another scalar field* $\phi_2 = \boldsymbol{Q}_{\hat{E}\to E}\phi_1$ *in* E *through the composition:*

$$\phi_2(\boldsymbol{x_2}) = (Q_{\hat{E}\to E})(\boldsymbol{x_2}) = \phi_1(\boldsymbol{x_1}) \tag{3.17}$$

in which $\boldsymbol{x_2} = \boldsymbol{T}_{\hat{E}\to E}(\boldsymbol{x_1})$*. Analogously, define* $\boldsymbol{Q}_{\hat{E}\to E} : H_0^1(\hat{E},\mathbb{R}) \to H_0^1(E,\mathbb{R})$ *such that a vector field* $\boldsymbol{\phi_1}$ *in* $\hat{E}$ *is mapped into another vector field* $\boldsymbol{\phi_2} = Q_{\hat{E}\to E}\boldsymbol{\phi_1}$ *in* E *through the composition:*

$$\boldsymbol{\phi_2}(\boldsymbol{x_2}) = (\boldsymbol{Q}_{\hat{E}\to E})(\boldsymbol{x_2}) = \boldsymbol{\phi_1}(\boldsymbol{x_1}) \tag{3.18}$$

in which $\boldsymbol{x_2} = \boldsymbol{T}_{\hat{E}\to E}(\boldsymbol{x_1})$*. Hereafter* $\boldsymbol{T_E}$*,* Q_E *and* $\boldsymbol{Q_E}$ *will represent* $\boldsymbol{T}_{\hat{E}\to E}$*,* $Q_{\hat{E}\to E}$*, and* $\boldsymbol{Q}_{\hat{E}\to E}$*, respectively.*

Figure 6 depicts an example of mapping between a real element and the parent domain, and also the order of the nodes of both.

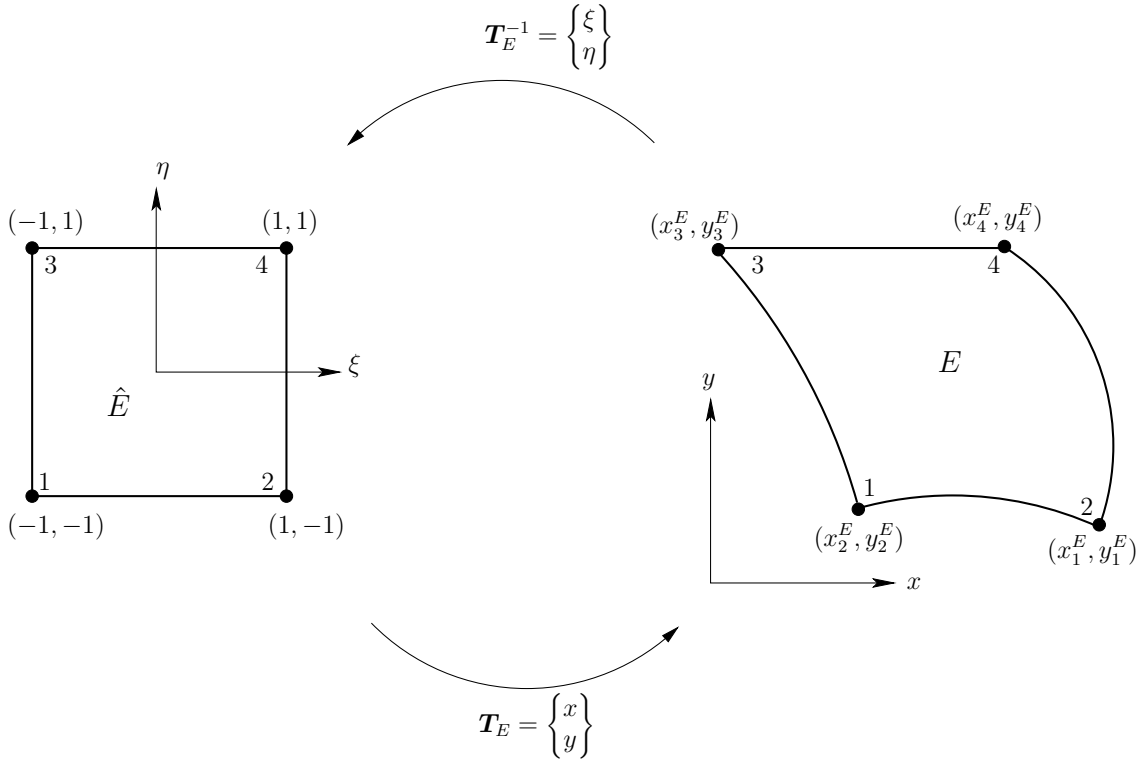

Figure 6 – Parent domain, biquadratic quadrilateral element domain, their node orderings, and mapping between them.

Now, it is useful to introduce the global/local terminology to refer to the choice of coordinate system: in the local approach, one can define local polynomials to approximate the pressure in the local coordinate system, namely, the parent domain (Figure 6), while in the global one the pressure must be approximated using shape functions defined on the global coordinate system (ARNOLD et al., 2001b), namely, in the real element.

Note that in Equation (3.16), the velocity is calculated in the parent domain $\hat{E}$ and that the pressure is calculated in the real element E of the global mesh (*unmapped pressure approach*). The unmapped pressure approach is chosen because it ensures a quadratic convergence for the pressure in $L^2(\Omega, \mathbb{R})$, which is an optimal approximation, while the local model (*mapped pressure approach*) turns out to be suboptimally convergent (BOFFI; BREZZI; FORTIN, 2013). The theory that explains this phenomenon is developed in the reference (ARNOLD; BOFFI; FALK, 2002). The authors essentially show that the space P_1 must be contained in the image of the mapping from the parent to the real element, which is guaranteed only if the map is affine. Since this is not the case of the transformations used throughout this text, which are general quadratic polynomials, the global pressure approach will be used. Some numerical results over this issue are presented in Subsection 3.2.5, and can also be found in references (BOFFI; GASTALDI, 2002), (ARNOLD et al., 2001b).

3.2.4 Basis functions

The last tools needed to express the variational formulation in terms of functions in $\mathcal{U}_h \times \mathcal{P}_h$ are the basis for each space. Then, let N_E be the number of nodes per each element E, $\beta = \{\zeta_1(x,y), \zeta_2(x,y), \ldots, \zeta_{N_E}(x,y)\}$ be a basis for $\mathcal{U}_h$ and $\alpha = \{\bar{\phi}_1(x,y), \bar{\phi}_2(x,y), \ldots, \bar{\phi}_{N_p}(x,y)\}$ be a basis for $\mathcal{P}_h$ over an arbitrary element. One can express the local solutions $\boldsymbol{u_h}$, p_h and the test functions $\boldsymbol{w_h}$, q_h

as a linear combination of those basis:

$$\begin{aligned}
\boldsymbol{u_h}(\boldsymbol{x}(\xi,\eta)) &= \sum_{j=1}^{N_E} \boldsymbol{u_j}\zeta_j(\boldsymbol{x}(\xi,\eta)) \\
\boldsymbol{w_h}(\boldsymbol{x}(\xi,\eta)) &= \sum_{i=1}^{N_E} \boldsymbol{w_i}\zeta_i(\boldsymbol{x}(\xi,\eta)) \\
p_h(\boldsymbol{x}(\xi,\eta)) &= \sum_{k=1}^{N_p} p_k\bar{\phi}_k(\boldsymbol{x}(\xi,\eta)) \\
q_h(\boldsymbol{x}(\xi,\eta)) &= \sum_{l=1}^{N_p} q_l\bar{\phi}_l(\boldsymbol{x}(\xi,\eta))
\end{aligned} \tag{3.19}$$

in which p_k and q_l are constants, N_p is the polynomial space degree used to approximate the pressure in each element E, and

$$\boldsymbol{u_i} = (u_i, v_i)^T, \quad \boldsymbol{w_i} = (w_i, z_i)^T, \tag{3.20}$$

in which all the components of $\boldsymbol{u_i}, \boldsymbol{w_i}$ are constant.

The mesh used to approximate the solution in this work is composed by quadrilateral elements — to which the element type Q_2P_1 was proposed (BOFFI; BREZZI; FORTIN, 2013) — each one with $N_E = 9$ nodes as shown in Figure 7, and the number of degrees of freedom of the space P_1 is $N_p = 3$ for each element E.

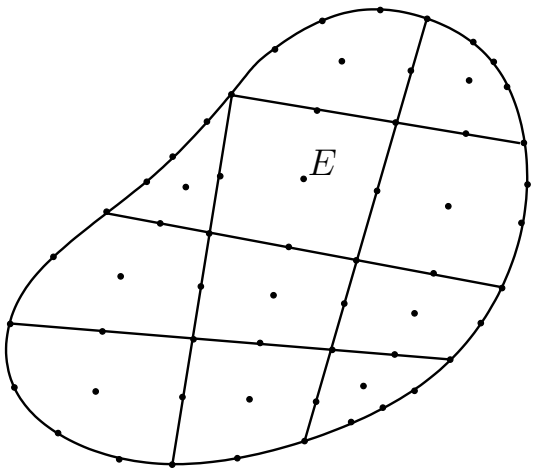

Figure 7 – Mesh.

Consider that, for each $\hat{E}$, there are $m \in \mathbb{N}$ nodes and its respective shape functions $\hat{\beta} = \{\phi_1(x,y), \phi_2(x,y), \ldots, \phi_m(x,y)\}$, which is a basis for the

standard element. Using the map $\boldsymbol{T_E}$, one gets

$$\boldsymbol{T_E}(\boldsymbol{\xi}) = \sum_{i=1}^{m} \phi_i(\boldsymbol{\xi}) \boldsymbol{x}_i^E. \tag{3.21}$$

Note that, while there are N_E nodes per element E and shape functions ϕ_k, $k = 1, \ldots, N_E$, used to approximate the velocity, the polynomial maps used to define the mesh geometry are of degree m, which may be greater, less or equal than N_E. The special case in which $m = N_E$, the map $\boldsymbol{T_E}$ is called isoparametric (BECKER; CAREY; ODEN, 1981), and this is the one used throughout the present work. For instance, $\boldsymbol{u_h}$ is expressed as

$$\boldsymbol{u_h}(\boldsymbol{\xi}) = \sum_{j=1}^{m} \phi_j(\boldsymbol{\xi}) \boldsymbol{u}_j^e. \tag{3.22}$$

Using the analogous expression for $\boldsymbol{w}_h$, and the expressions given by Equation (3.19) for p_h and q_h, it follows that the problem (3.9) is reduced to the approximation problem given by Equation (3.23).

$$\begin{aligned} a(\boldsymbol{u}_h, \boldsymbol{w}_h) + b(\boldsymbol{w}_h, p_h) &= f(\boldsymbol{w}_h), \qquad \forall \boldsymbol{w_h} \in \mathcal{U}_h, \\ d(\boldsymbol{u}_h, q_h) &= g(q_h), \qquad \forall q_h \in \mathcal{P}_h. \end{aligned} \tag{3.23}$$

3.2.4.1 Computational implementation

Methods that employ discontinuous interpolations for pressure without addition of jump terms, allow this variable to be eliminated at element level. In order to do so, a term that represents a small compressibility is added in the second equation of (3.23):

$$d(\boldsymbol{u}_h, q_h) + \frac{1}{\lambda}(p_h, q_h) = g(q_h), \tag{3.24}$$

in which λ is called penalty parameter, and is big enough so as not to perturb the solution. With the introduction of this term it is possible to achieve a condensation of the variables so that the system can be solved for the velocity and then, from a post-processing, to obtain the pressure.

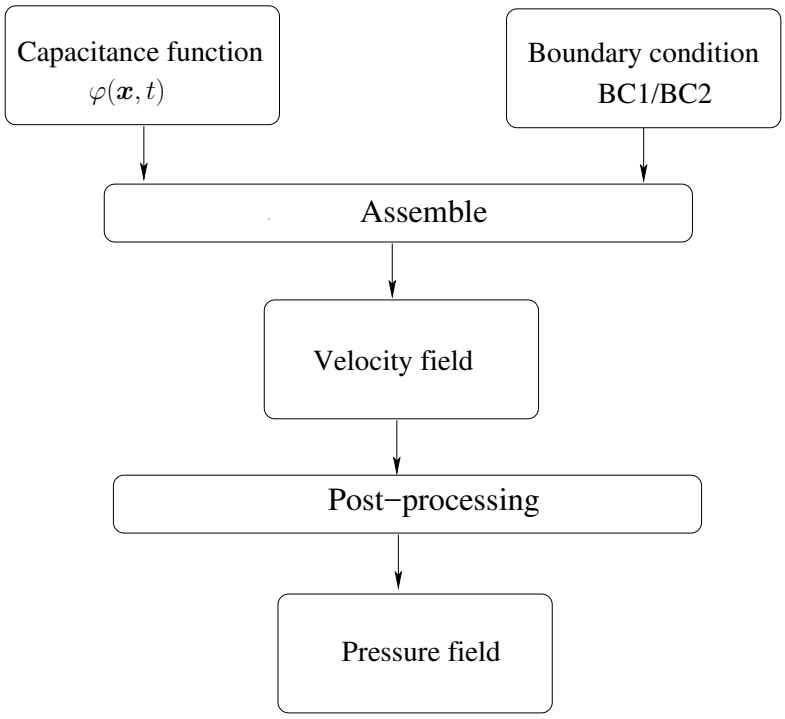

Figure 8 – Schematic diagram of routines and functions.

Thus, the form $c(\cdot,\cdot) : \mathcal{P} \times \mathcal{P} \to \mathbb{R}$ is defined to be bilinear and continuous:

$$c(p, q) = \frac{1}{\lambda}(p, q). \tag{3.25}$$

Leading to a compact form of Equation (3.24):

$$d(\boldsymbol{u}_h, q_h) + c(p_h, q_h) = g(q_h), \tag{3.26}$$

which, together with the first equation of (3.23), and using expressions from Equations (3.19) for $\boldsymbol{u_h}, \boldsymbol{w_h}, q_h, p_h$, yield a matrix form of Equation (3.9):

$$\begin{bmatrix} W_E & Q_E \end{bmatrix} \begin{bmatrix} \boldsymbol{A} & \boldsymbol{B} \\ \boldsymbol{D} & \boldsymbol{C} \end{bmatrix} \begin{bmatrix} U_E \\ P_E \end{bmatrix} = \begin{bmatrix} W_E & Q_E \end{bmatrix} \begin{bmatrix} F \\ G \end{bmatrix} \tag{3.27}$$

where W_E, U_E are the coefficient matrices of $\boldsymbol{u_i}, \boldsymbol{w_i}$ of each node of element E, respectively; and P_E, Q_E are the matrices of coefficients that multiply the basis functions of space $\mathcal{P}_h$ in element E.

Since Equation (3.27) holds for every W_E and P_E, the linear system (3.23) can be expressed as:

$$\begin{bmatrix} \boldsymbol{A} & \boldsymbol{B} \\ \boldsymbol{D} & \boldsymbol{C} \end{bmatrix} \begin{bmatrix} U_E \\ P_E \end{bmatrix} = \begin{bmatrix} F \\ G \end{bmatrix}. \tag{3.28}$$

Note that for the classical Stokes Problem this problem could be expressed as a symmetric linear system:

$$\begin{bmatrix} \boldsymbol{A} & \boldsymbol{B} \\ \boldsymbol{B}^T & \boldsymbol{C} \end{bmatrix} \begin{bmatrix} U_E \\ P_E \end{bmatrix} = \begin{bmatrix} F \\ G \end{bmatrix}. \tag{3.29}$$

The expressions for each submatrix of Equation (3.28) are listed in Subsection 3.2.4.2. Observe that from Equation (3.28), one gets:

$$\boldsymbol{A}U_E + \boldsymbol{B}P_E = F \tag{3.30}$$

$$\boldsymbol{D}U_E + \boldsymbol{C}P_E = G. \tag{3.31}$$

And, from Equation (3.31) combined with the fact that $\boldsymbol{C}$ is invertible, it follows that P_E can be expressed as:

$$P_E = \boldsymbol{C}^{-1}(-\boldsymbol{D}U_E + G). \tag{3.32}$$

Substituting the Expression (3.32) for P_E on Equation (3.30), it remains a linear system for U_E:

$$(\boldsymbol{A} - \boldsymbol{B}\boldsymbol{C}^{-1}\boldsymbol{D})U_E = -\boldsymbol{B}\boldsymbol{C}^{-1}G + F \tag{3.33}$$

which is spread in the global matrix system $\boldsymbol{A_b}U = \boldsymbol{B_b}$, from where the global approximation for velocity U is obtained. In the following, the solution U_E in each element is recovered in order to determine P_E from Equation (3.34):

$$P_E = -\tilde{\boldsymbol{A}}_{\boldsymbol{E}}U_E + \tilde{\boldsymbol{B}}_{\boldsymbol{E}}, \tag{3.34}$$

in which the matrices

$$\tilde{\boldsymbol{A}}_{\boldsymbol{E}} = \boldsymbol{C}^{-1}\boldsymbol{D},$$
$$\tilde{\boldsymbol{B}}_{\boldsymbol{E}} = \boldsymbol{C}^{-1}G,$$

were stored in the calculation process of $\boldsymbol{B}$, $\boldsymbol{D}$ and $\boldsymbol{C}^{-1}$ for each element E.

3.2.4.2 Matrix form

In Sub-subsection 3.2.4.1 the Stokes problem was reduced to a linear system given by equation (3.28). The expressions of the submatrices that make up this system are:

- $\boldsymbol{A}$: $(2m) \times (2m)$, with elements

$$A_{2i-1,2j-1} = \int_\Omega \left(2\mu \frac{\partial \phi_i}{\partial x}\frac{\partial \phi_j}{\partial x} + \mu \frac{\partial \phi_i}{\partial y}\frac{\partial \phi_j}{\partial y} \right) d\Omega \tag{3.35}$$

$$A_{2i-1,2j} = \int_\Omega \left(\mu \frac{\partial \phi_i}{\partial y}\frac{\partial \phi_j}{\partial x} \right) d\Omega \tag{3.36}$$

$$A_{2i,2j-1} = \int_\Omega \left(\mu \frac{\partial \phi_i}{\partial x}\frac{\partial \phi_j}{\partial y} \right) d\Omega \tag{3.37}$$

$$A_{2i,2j} = \int_\Omega \left(\mu \frac{\partial \phi_i}{\partial x}\frac{\partial \phi_j}{\partial x} + 2\mu \frac{\partial \phi_i}{\partial y}\frac{\partial \phi_j}{\partial y} \right) d\Omega \tag{3.38}$$

- $\boldsymbol{B}$: $(2m) \times (np)$, with elements

$$B_{2i-1,k} = -\int_\Omega \left(\frac{\partial \phi_i}{\partial x}\bar{\phi}_k \right) d\Omega \tag{3.39}$$

$$B_{2i,k} = -\int_\Omega \left(\frac{\partial \phi_i}{\partial y}\bar{\phi}_k \right) d\Omega \tag{3.40}$$

- $\boldsymbol{C}$: $(np) \times (np)$, with elements

$$C_{l,k} = \frac{1}{\lambda}\int_\Omega \left(\bar{\phi}_l \bar{\phi}_k \right) d\Omega \tag{3.41}$$

- $\boldsymbol{D}$: $(np) \times (2m)$, with elements

$$D_{l,2i-1} = \int_\Omega \left[\varphi \frac{\partial \phi_i}{\partial x} + \phi_i \frac{\partial \varphi}{\partial x} \right] \bar{\phi}_k d\Omega; \tag{3.42}$$

- F: $(2m) \times 1$, with elements

$$F^e_{2j-1,k} = \int_\Omega (\varphi f_1 \phi_j)\, d\Omega + \int_{\partial\Omega} (t_1 \phi_j)\, dl \tag{3.43}$$

$$F^e_{2j,k} = \int_\Omega (\varphi f_2 \phi_j)\, d\Omega + \int_{\partial\Omega} (t_2 \phi_j)\, dl \tag{3.44}$$

- G: $(np) \times 1$, with elements

$$G^e_{k,1} = \int_\Omega \left(g\bar{\phi_k}\right) d\Omega \tag{3.45}$$

with $l, k = 1, \ldots, np$; $j, i = 1, \ldots, m$.

3.2.5 Error analysis and numerical experiments

In this subsection, the efficiency of the approximations obtained using the Galerkin Finite Element Method in an orthogonal quadrilateral mesh, and the results obtained from code validation will be discussed.

Towards performing the code validation, some known solutions for the Stokes problem were used, verifying if convergence and expected order of approximation were reached for the space Q_2P_1. The obtained numerical solution $\boldsymbol{u_h}$ is compared to the exact one $\boldsymbol{u}$, as well as the numerical result for pressure p_h is compared to the theoretical p, using the L^2 norm. The expected estimates are given by Equations (3.46) (BOFFI; GASTALDI, 2002).

$$\begin{aligned} ||\boldsymbol{u} - \boldsymbol{u_h}|| &= Ch^3 \\ ||\boldsymbol{\nabla u} - \boldsymbol{\nabla u_h}|| &= Ch^2 \\ ||p - p_h|| &= Ch^2. \end{aligned} \tag{3.46}$$

In the following, there are several numerical experiments, all of them are made using a uniform discretization of elements Q_2P_1 in quadrilateral meshes with the same number 2^n of elements in x and y directions. The number n was taken as 1, 2, 3,4, and 5. The method order was calculated from Equations (3.46) using the errors obtained for two consecutive approximations $\boldsymbol{u_h}$, and $\boldsymbol{u_{2h}}$. Thus,

$$\frac{||\boldsymbol{u} - \boldsymbol{u_h}||}{||\boldsymbol{u} - \boldsymbol{u_{2h}}||} = \frac{Ch^3}{C(2h)^3} \tag{3.47}$$

Simplifying and applying the logarithm, one obtains

$$\frac{\ln(||\boldsymbol{u} - \boldsymbol{u_{2h}}||) - \ln(||\boldsymbol{u} - \boldsymbol{u_h}||)}{\ln(2)} = 3. \tag{3.48}$$

In the next subsections some simulations of the Stokes problem are performed in order to validate the code.

3.2.5.1 Simulation 1

The method validation was done considering the domain $\Omega = [-1, 1]^2$, viscosity $\mu = 1.0$, and the penalty parameter $\lambda = 10^8$. The capacitance function was set constant $\varphi = 1$, and the analytic solution:

$$\boldsymbol{u}(x, y) = \pi \begin{bmatrix} \cos(\pi x)\text{sen}(\pi y) \\ -\text{sen}(\pi x)\cos(\pi y) \end{bmatrix}, \quad \text{and} \quad p = (1 + 2\pi^2)\text{sen}(\pi x)\text{sen}(\pi y) \tag{3.49}$$

is given, considering the Dirichlet boundary conditions on all domain edges.

The convergence rates obtained for the sequence of trapezoidal meshes described in (BOFFI; GASTALDI, 2002) are presented in Table 1. The velocity profiles in directions x and y, and the pressure field are presented in Figures 9a, 9b and 10a, respectively.

The convergence results for the (pathological) case where the space for the pressure is mapped from the reference element

$$\bar{\mathcal{P}}_h := \{p_h \in \mathcal{P};\ p_h|_E \in Q_E(\mathbb{P}_{k-1}(\hat{E}, \mathbb{R}^2))\},$$

are presented in Table 2. It can be seen that, by using the space $\mathcal{U}_h \times \bar{\mathcal{P}}_h$, the convergence order for the pressure approaches 1.0 and for the velocity drops to 2.0, as the mesh is refined. For the sake of comparison, the mapped pressure profile is shown in Figure 10b. The velocity profiles (not shown) are basically the same of the unmapped case. Because of this sub-optimal convergence, already mentioned in the literature (BOFFI; GASTALDI, 2002), (BOFFI; BREZZI; FORTIN, 2013), the chosen space for the pressure in Equation (3.16) was $\mathcal{P}_h$, the global one.

Table 1 – Results obtained for the incompressible Stokes Problem with unmapped pressure.

2^n	$\|\|\boldsymbol{u} - \boldsymbol{u_h}\|\|$	Order	$\|\|\boldsymbol{\nabla}(\boldsymbol{u} - \boldsymbol{u_h})\|\|$	Order	$\|\|p - p_h\|\|$	Order
2	0.1262E+01	2.5032	0.8282E+01	1.5569	0.1301E+02	1.3716
4	0.2226E+00	3.0650	0.2815E+01	2.0214	0.5029E+01	1.9258
8	0.2660E-01	3.0363	0.6933E+00	2.0492	0.1324E+01	1.9739
16	0.3243E-02	3.0064	0.1675E+00	2.0171	0.3369E+00	1.9962
32	0.4035E-03	2.9854	0.41385E-01	2.0030	0.8446E-01	1.9997

Table 2 – Results obtained for the incompressible Stokes Problem with mapped pressure.

2^n	$\|\|\boldsymbol{u} - \boldsymbol{u_h}\|\|$	Order	$\|\|\boldsymbol{\nabla}(\boldsymbol{u} - \boldsymbol{u_h})\|\|$	Order	$\|\|p - p_h\|\|$	Order
2	0.1267E+01	2.4898	0.8306E+01	1.5552	0.1303E+02	1.3949
4	0.2255E+00	2.8284	0.2826E+01	1.8757	0.4956E+01	1.7489
8	0.3175E-01	2.5395	0.7701E+00	1.7080	0.1475E+01	1.6396
16	0.5461E-02	2.2103	0.2357E+00	1.3423	0.4733E+00	1.3331
32	0.1180E-02	2.0580	0.9297E-01	1.1119	0.1878E+00	1.1166

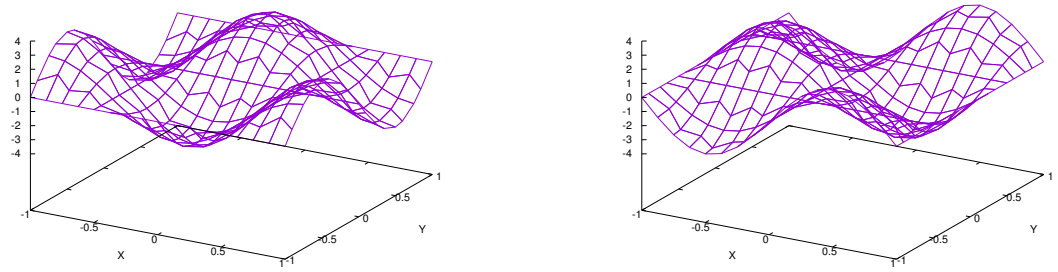

(a) Velocity profile in x direction. (b) Velocity profile in y direction.

Figure 9 – Speed profiles for incompressible Stokes.

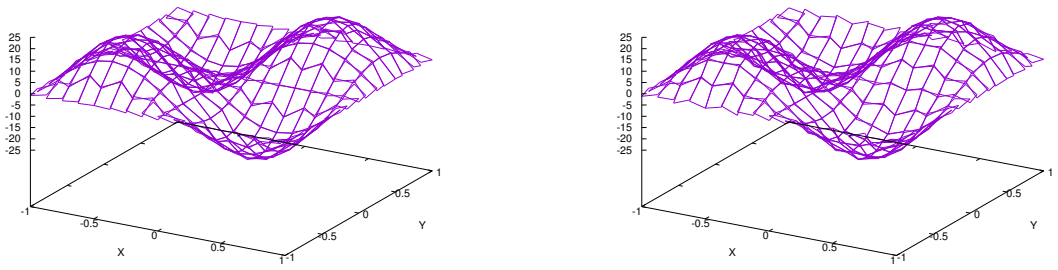

(a) Unmapped pressure profile. (b) Mapped Pressure Profile.

Figure 10 – Pressure profiles for incompressible Stokes.

3.2.5.2 Simulation 2

Another study of convergence was done in a domain $\Omega = [0, 1]^2$, with viscosity $\mu = 1.0$, and the penalty parameter $\lambda = 10^8$. The capacitance function

was set to be $\varphi = 1 + 0.5\text{sen}(\pi x)\text{sen}(\pi y)$, and the analytic solution

$$\boldsymbol{u} = \begin{bmatrix} \text{sen}(\pi x)\text{sen}(\pi y) \\ 0 \end{bmatrix} \quad p = \text{sen}(\pi x)\text{sen}(\pi y), \tag{3.50}$$

is given. A homogeneous Dirichlet condition was imposed on the upper and lower edges, and, on the lateral edges, a mixed boundary condition: the x-velocity component $u = 0$ was imposed strongly, in other words, the arrays were modified to introduce the solution on the boundary, whereas the traction component $t_2(\boldsymbol{x}) = -p(\boldsymbol{x})$ was imposed weakly, *i.e.*, it is added inside the boundary integral that appears on the variational formulation (Equation (3.8)).

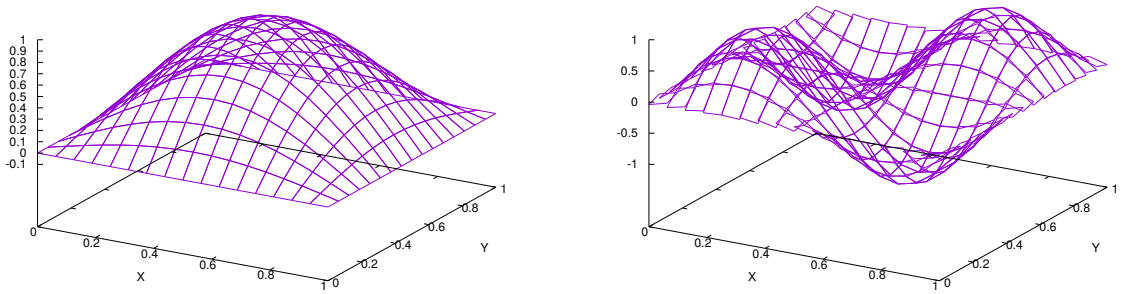

(a) (b)

Figure 11 – (a) Velocity profile in x direction. (b) Global pressure profile.

Table 3 – Results obtained for the incompressible Stokes Problem with global pressure.

n	$\|\|\boldsymbol{u} - \boldsymbol{u_h}\|\|$	Order	$\|\|\boldsymbol{\nabla}(\boldsymbol{u} - \boldsymbol{u_h})\|\|$	Order	$\|\|p - p_h\|\|$	Order
2	0.1555E-01	-	0.2065E+00	-	0.3056E+00	-
4	0.2642E-02	2.5575	0.6542E-01	1.6585	0.1134E+00	1.4301
8	0.2970E-03	3.1531	0.1514E-01	2.1111	0.3035E-01	1.9017
16	0.3503E-04	3.0836	0.3452E-02	2.1328	0.7633E-02	1.9913
32	0.4377E-05	3.0008	0.8237E-03	2.0673	0.1905E-02	2.0022

3.2.5.3 Simulation 3: Poiseuille flow

The Poiseuille flow is a classical problem in fluid mechanics that mathematically describes a characteristic pipe flow (WHITE, 2011). To simulate it, consider the domain $\Omega = [-1, 1]^2$, the viscosity $\mu = 1.0$, and the penalty parameter

$\lambda = 10^8$. The capacitance function was set to be $\varphi = 1 + 0.5\text{sen}(\pi x)\text{sen}(\pi y)$, and the analytic solution

$$\boldsymbol{u} = \begin{bmatrix} 0 \\ \dfrac{1 - y^2}{2\mu} \end{bmatrix} \quad p = y + 1, \tag{3.51}$$

was given. Since the functions above belong to the space of solutions, the error in the first iteration with the coarsest mesh reached the order 10^{-7}, as was expected.

A homogeneous Dirichlet condition was imposed on the lateral edges, and, on the upper and lower ones, the same mixed boundary condition was considered for simulation 2 (Subsection 3.2.5.2).

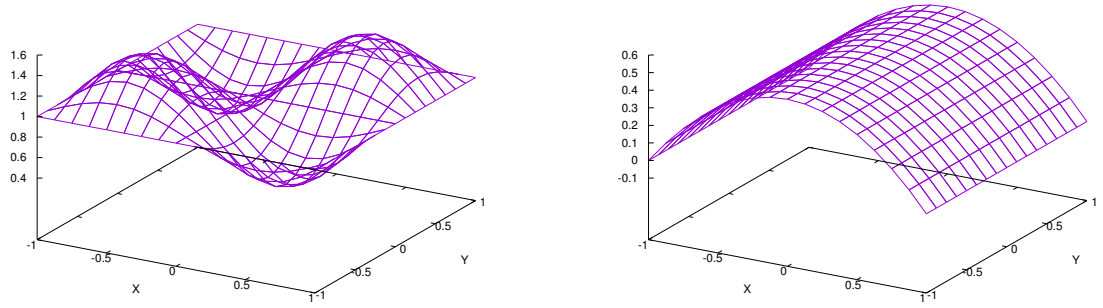

(a) (b)

Figure 12 – (a)Capacitance function profile. (b)Velocity profile in y direction.

Figures 12b and 13b show the velocity profile and the velocity field of the flow respectively. Figures 12a, and 13a illustrate its capacitance function and pressure profile.

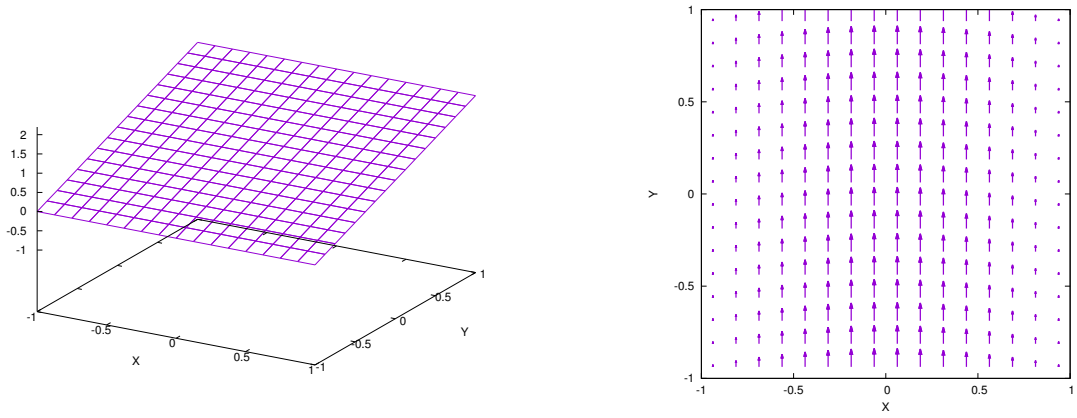

(a) (b)

Figure 13 – (a) Pressure profile. (b) Velocity field.

3.3 Oseen equations

The Oseen problem is also a simplification of the problem described by Equations (2.19), in a stationary regime. The difference from the Stokes problem is that here there is an advection term, and it is represented by equations:

$$\begin{aligned} 2\mu\boldsymbol{\nabla}\cdot\boldsymbol{\epsilon}(\boldsymbol{u}) - \boldsymbol{\nabla}p + (\boldsymbol{\nabla}\boldsymbol{u})\boldsymbol{a} &= -\varphi\rho\boldsymbol{f} && \text{in} && \Omega; \\ \varphi\boldsymbol{\nabla}\cdot\boldsymbol{u} + \boldsymbol{u}\cdot\boldsymbol{\nabla}\varphi &= 0 && \text{in} && \Omega; \\ \boldsymbol{u} &= \bar{\boldsymbol{u}} && \text{over} && \Gamma_D; \\ \boldsymbol{p} &= \bar{\boldsymbol{p}} && \text{over} && \Gamma_N. \end{aligned} \tag{3.52}$$

where $\boldsymbol{a}$ is a known vector field. The classical Oseen Problem is represented by (3.52) when $\varphi = 1$. It may present instabilities if the Reynolds number is high, and stabilization methods are frequently needed (CONCEICAO, 2006).

3.3.1 Variational formulation

Analogously to the Stokes problem, the variational formulation for the Oseen one can be expressed as:

Find the pair $(\boldsymbol{u}, p) \in \mathcal{U} \times \mathcal{P}$ such that

$$\begin{aligned} \int_\Omega \Big\{ 2\mu\boldsymbol{\epsilon}(\boldsymbol{u}) : \boldsymbol{\epsilon}(\boldsymbol{w}) + [(\boldsymbol{\nabla}\boldsymbol{u})\boldsymbol{a}] \cdot \boldsymbol{w} \Big\} d\Omega - \int_\Omega p\boldsymbol{\nabla} \cdot \boldsymbol{w} d\Omega = \rho \int_\Omega \varphi \boldsymbol{f} \cdot \boldsymbol{w} d\Omega, \\ \int_\Omega \left(\varphi \boldsymbol{\nabla} \cdot \boldsymbol{u} + \boldsymbol{u} \cdot \boldsymbol{\nabla}\varphi\right) q d\Omega = \int_\Omega 0 q d\Omega \end{aligned} \tag{3.53}$$

hold for all $\boldsymbol{w} \in \mathcal{U}$, and $q \in \mathcal{P}$. Or, in the abstract form:

$$\begin{aligned} a(\boldsymbol{u}, \boldsymbol{w}) + b(\boldsymbol{w}, p) &= f(\boldsymbol{w}), \quad \forall \boldsymbol{w} \in \mathcal{U}; \\ d(\boldsymbol{u}, q) &= g(q), \qquad \forall q \in \mathcal{P}. \end{aligned} \tag{3.54}$$

In which $a(\cdot,\cdot) : \mathcal{U} \times \mathcal{U} \to \mathbb{R}$, $b(\cdot,\cdot) : \mathcal{U} \times \mathcal{P} \to \mathbb{R}$, and $d(\cdot,\cdot) : \mathcal{U} \times \mathcal{P} \to \mathbb{R}$ are bilinear forms, $f(\cdot) : \mathcal{U} \to \mathbb{R}$, and $g(\cdot) : \mathcal{P} \to \mathbb{R}$ are continuous linear functionals such that

$$a(\boldsymbol{u}, \boldsymbol{w}) = \int_\Omega \Big\{ 2\mu\boldsymbol{\epsilon}(\boldsymbol{u}) : \boldsymbol{\epsilon}(\boldsymbol{w}) + [(\boldsymbol{\nabla}\boldsymbol{u})\boldsymbol{a}] \cdot \boldsymbol{w} \Big\} d\Omega \tag{3.55}$$

$$b(\boldsymbol{w}, p) = -\int_\Omega p\boldsymbol{\nabla} \cdot \boldsymbol{w} d\Omega, \tag{3.56}$$

$$d(\boldsymbol{u}, q) = \int_\Omega (\varphi \boldsymbol{\nabla} \cdot \boldsymbol{u} q + \boldsymbol{u} \cdot \boldsymbol{\nabla}\varphi q) d\Omega \tag{3.57}$$

$$f(\boldsymbol{w}) = \rho \int_\Omega \boldsymbol{f} \cdot \boldsymbol{w} d\Omega + \int_{\partial\Omega} \boldsymbol{t} \cdot \boldsymbol{w} dl \tag{3.58}$$

$$g(q) = \int_\Omega 0 q d\Omega = 0. \tag{3.59}$$

3.3.2 Matrix form

In order to approximate the Oseen problem, the function and approximation spaces are the same as the ones defined in Subsections 3.2.1, and 3.2.2 respectively. The matrix form resulting from these choices is just as in the case of the Stokes problem, except for a small modification in matrix A:

- $\boldsymbol{A}$: $(2m) \times (2m)$, with elements

$$
\begin{aligned}
A_{2i-1,2j-1} &= \int_\Omega \left[2\mu \frac{\partial \phi_i}{\partial x}\frac{\partial \phi_j}{\partial x} + \mu \frac{\partial \phi_i}{\partial y}\frac{\partial \phi_j}{\partial y} + \left(\frac{\partial \phi_j}{\partial x} a_1 + \frac{\partial \phi_j}{\partial y} a_2 \right) \phi_i \right] d\Omega \\
A_{2i-1,2j} &= \int_\Omega \left(\mu \frac{\partial \phi_j}{\partial y}\frac{\partial \phi_i}{\partial x} \right) d\Omega \\
A_{2i,2j-1} &= \int_\Omega \left(\mu \frac{\partial \phi_j}{\partial x}\frac{\partial \phi_i}{\partial y} \right) d\Omega \\
A_{2i,2j} &= \int_\Omega \left[\mu \frac{\partial \phi_i}{\partial x}\frac{\partial \phi_j}{\partial x} + 2\mu \frac{\partial \phi_i}{\partial y}\frac{\partial \phi_j}{\partial y} + \left(\frac{\partial \phi_j}{\partial x} a_1 + \frac{\partial \phi_j}{\partial y} a_2 \right) \phi_i \right] d\Omega
\end{aligned}
$$

4 Navier-Stokes Problem

In this chapter, the general problem of approximating the modified Navier-Stokes equations (2.19) is addressed. The algorithm for linearization, and to approximate the variation in time is presented. The variational problem is formulated, and then the space discretizations lead to a matrix form of the problem, which is the last step before performing the numerical simulations.

4.1 Nonlinear Variational Formulation

From the strong form of the conservation principles presented in Section 2.2, the derivation of the variational formulation corresponding to these equations will be presented in this section. Consider the partition of the time interval I in time steps

$$\Delta t^n = t^{n+1} - t^n, \quad \text{with} \quad \sum_n \Delta t^n = T. \tag{4.1}$$

For the sake of simplicity in what follows a uniform partition is assumed with $\Delta t^n = \Delta t$. It is important to note that the final scheme holds for nonuniform partitions, though.

The first step is to integrate the second equation of (2.19),

$$\int_{t_n}^{t_{n+1}} \left[\rho\varphi(\boldsymbol{x},\tau)\frac{\partial \boldsymbol{u}}{\partial \tau} + \rho\varphi(\boldsymbol{x},\tau)(\boldsymbol{\nabla u})\boldsymbol{u}\right] d\tau = \int_{t_n}^{t_{n+1}} [\rho\varphi(\boldsymbol{x},\tau)\boldsymbol{f} + \boldsymbol{\nabla}\cdot\boldsymbol{\sigma}]\, d\tau, \tag{4.2}$$

adopting an implicit Euler scheme to approximate the integrals, with φ evaluated in time step t^{n+1}. This leads to the following equation discrete in time

$$\begin{aligned}\rho\varphi^{n+1}(\boldsymbol{u}^{n+1} - \boldsymbol{u}^n) + \Delta t\rho(\boldsymbol{\nabla}\varphi^{n+1}\boldsymbol{u}^{n+1})\boldsymbol{u}^{n+1} = \Delta t\rho\varphi^{n+1}\boldsymbol{f}^{n+1} + \Delta t\boldsymbol{\nabla}\cdot\boldsymbol{\sigma}^{n+1} \\ +\mathcal{O}((\Delta t)^2),\end{aligned} \tag{4.3}$$

where $\boldsymbol{u}^{n+1}$ and $\boldsymbol{u}^n$ stand for the velocity vector fields at times t^{n+1} and t^n, respectively and $\varphi^{n+1} = \varphi(\boldsymbol{x}, t^{n+1})$. By dropping the $\mathcal{O}((\Delta t)^2)$ error, multiplying (4.3) by a test function $\boldsymbol{w} \in \mathcal{U}$ and integrating on Ω, one gets the semidiscrete

(discrete in time, continuous in space) equation

$$\begin{aligned}\int_\Omega \rho\varphi^{n+1}(\boldsymbol{u}^{n+1}-\boldsymbol{u}^n)\cdot\boldsymbol{w}d\Omega+\Delta t\int_\Omega \rho\varphi^{n+1}[(\boldsymbol{\nabla}\boldsymbol{u}^{n+1})\boldsymbol{u}^{n+1}]\cdot\boldsymbol{w}d\Omega\\ =\Delta t\int_\Omega \rho\varphi^{n+1}\boldsymbol{f}^{n+1}\cdot\boldsymbol{w}d\Omega+\Delta t\int_\Omega(\boldsymbol{\nabla}\cdot\boldsymbol{\sigma}^{n+1})\cdot\boldsymbol{w}d\Omega.\end{aligned} \tag{4.4}$$

The term of the Cauchy stress tensor can be written as

$$\begin{aligned}\int_\Omega(\boldsymbol{\nabla}\cdot\boldsymbol{\sigma}^{n+1})\cdot\boldsymbol{w}d\Omega &= \int_\Omega\boldsymbol{\nabla}\cdot((\boldsymbol{\sigma}^{n+1})^t\boldsymbol{w})d\Omega-\int_\Omega\boldsymbol{\sigma}^{n+1}:\boldsymbol{\nabla}\boldsymbol{w}d\Omega\\ &= \int_{\partial\Omega}(\boldsymbol{\sigma}^{n+1}\boldsymbol{n})\cdot\boldsymbol{w}d\Gamma-\int_\Omega\boldsymbol{\sigma}^{n+1}:\boldsymbol{\nabla}\boldsymbol{w}d\Omega\\ &= \int_{\partial\Omega}\boldsymbol{t}^{n+1}\cdot\boldsymbol{w}d\Gamma-\int_\Omega\boldsymbol{\sigma}^{n+1}:\boldsymbol{\nabla}\boldsymbol{w}d\Omega\end{aligned}$$

where integration by parts, the symmetry of the stress tensor, the divergence theorem and the definition of the traction vector $\boldsymbol{t}=\boldsymbol{\sigma}\boldsymbol{n}$ were used. By using the constitutive equation (2.17), one can write the last integral in terms of the velocity and the pressure, as

$$\int_\Omega\boldsymbol{\sigma}^{n+1}:\boldsymbol{\nabla}\boldsymbol{w}d\Omega=2\mu\int_\Omega\boldsymbol{\epsilon}(\boldsymbol{u}^{n+1}):\boldsymbol{\epsilon}(\boldsymbol{w})d\Omega-\int_\Omega p^{n+1}\boldsymbol{\nabla}\cdot\boldsymbol{w}d\Omega \tag{4.5}$$

Thus, the first weak equation of the system is given by

$$\begin{aligned}\int_\Omega\rho\varphi^{n+1}\boldsymbol{u}^{n+1}\cdot\boldsymbol{w}d\Omega+\Delta t\int_\Omega\rho\varphi^{n+1}[(\boldsymbol{\nabla}\boldsymbol{u}^{n+1})\boldsymbol{u}^{n+1}]\cdot\boldsymbol{w}d\Omega\\ +2\mu\Delta t\int_\Omega\boldsymbol{\epsilon}(\boldsymbol{u}^{n+1}):\boldsymbol{\epsilon}(\boldsymbol{w})d\Omega-\Delta t\int_\Omega p^{n+1}\boldsymbol{\nabla}\cdot\boldsymbol{w}d\Omega-\Delta t\int_{\partial\Omega}\boldsymbol{t}^{n+1}\cdot\boldsymbol{w}d\Gamma\\ =\int_\Omega\rho\varphi^{n+1}\boldsymbol{u}^n\cdot\boldsymbol{w}d\Omega+\Delta t\int_\Omega\rho\varphi^{n+1}\boldsymbol{f}^{n+1}\cdot\boldsymbol{w}d\Omega\end{aligned} \tag{4.6}$$

The second equation follows by evaluating the first equation of (2.19) at $t=t^{n+1}$, multiplying it by $q\in\mathcal{P}$, and integrating on the domain Ω, leading to

$$\int_\Omega\varphi^{n+1}\boldsymbol{\nabla}\cdot\boldsymbol{u}^{n+1}qd\Omega+\int_\Omega\boldsymbol{u}^{n+1}\cdot\left(\boldsymbol{\nabla}\varphi^{n+1}\right)qd\Omega=-\int_\Omega\dot{\varphi}^{n+1}qd\Omega. \tag{4.7}$$

where $\dot{\varphi}^{n+1}$ stands for the time derivative of the capacitance function at $t=t^{n+1}$.

Equations (4.6) and (4.7) form the following nonlinear variational formulation posed in terms of the unknowns $\boldsymbol{u}^{n+1}$ and p^{n+1}:

Nonlinear problem *Given* $\boldsymbol{u}^n$ *find* $\boldsymbol{u}^{n+1} \in \mathcal{U}$ *and* $p^{n+1} \in \mathcal{P}$ *such that*

$$\begin{aligned}\int_\Omega \rho\varphi^{n+1}\boldsymbol{u}^{n+1}\cdot\boldsymbol{w}d\Omega &+ \Delta t\int_\Omega \rho\varphi^{n+1}[(\boldsymbol{\nabla}\boldsymbol{u}^{n+1})\boldsymbol{u}^{n+1}]\cdot\boldsymbol{w}d\Omega \\ &+ 2\mu\Delta t\int_\Omega \boldsymbol{\epsilon}(\boldsymbol{u}^{n+1}):\boldsymbol{\epsilon}(\boldsymbol{w})d\Omega \\ &- \Delta t\int_\Omega p^{n+1}\boldsymbol{\nabla}\cdot\boldsymbol{w}d\Omega - \Delta t\int_{\partial\Omega}\boldsymbol{t}^{n+1}\cdot\boldsymbol{w}d\Gamma \\ &= \Delta t\int_\Omega \rho\varphi^{n+1}\boldsymbol{f}^{n+1}\cdot\boldsymbol{w}d\Omega \\ &\quad + \int_\Omega \rho\varphi^{n+1}\boldsymbol{u}^n\cdot\boldsymbol{w}d\Omega \quad \forall\ \boldsymbol{w}\in\mathcal{U} \end{aligned} \tag{4.8}$$

and

$$\int_\Omega \varphi^{n+1}\boldsymbol{\nabla}\cdot\boldsymbol{u}^{n+1}qd\Omega + \int_\Omega \boldsymbol{u}^{n+1}\cdot\boldsymbol{\nabla}\varphi^{n+1}qd\Omega = -\int_\Omega \dot{\varphi}^{n+1}qd\Omega \quad \forall\ q\in\mathcal{P}. \tag{4.9}$$

The algorithm employed to solve this nonlinear problem is described in the next section.

4.2 Sequential Iterative Algorithm

In order to solve the **Nonlinear problem**, the term $(\boldsymbol{\nabla}\boldsymbol{u}^{n+1})\boldsymbol{u}^{n+1}$ is linearized in the form

$$(\boldsymbol{\nabla}\boldsymbol{u}^{n+1})\boldsymbol{u}^{n+1} = (\boldsymbol{\nabla}\boldsymbol{u}^{n+1,k+1})\boldsymbol{u}^{n+1,k} \tag{4.10}$$

where the index k denotes the iteration. Thus, by setting the unknowns $\boldsymbol{u} = \boldsymbol{u}^{n+1,k+1}$ and $p = p^{n+1,k+1}$, one step of the iterative algorithm is defined by the following linear variational formulation:

Linearized problem *Given* $\boldsymbol{u}^n$ *and* $\boldsymbol{u}^{n+1,k}$ *find* $\boldsymbol{u} = \boldsymbol{u}^{n+1,k+1} \in \mathcal{U}$ *and* $p = p^{n+1,k+1} \in \mathcal{P}$ *such that*

$$\begin{aligned}\int_\Omega \rho\varphi^{n+1}\boldsymbol{u}\cdot\boldsymbol{w}d\Omega &+ \Delta t\int_\Omega \rho\varphi^{n+1}[(\boldsymbol{\nabla u})\boldsymbol{u}^{n+1,k}]\cdot\boldsymbol{w}d\Omega \\ &+ 2\mu\Delta t\int_\Omega \boldsymbol{\epsilon}(\boldsymbol{u}):\boldsymbol{\epsilon}(\boldsymbol{w})d\Omega \\ &- \Delta t\int_\Omega p\boldsymbol{\nabla}\cdot\boldsymbol{w}d\Omega - \Delta t\int_{\partial\Omega}\boldsymbol{t}^{n+1}\cdot\boldsymbol{w}d\Gamma \\ &= \Delta t\int_\Omega \rho\varphi^{n+1}\boldsymbol{f}^{n+1}\cdot\boldsymbol{w}d\Omega \\ &\quad + \int_\Omega \rho\varphi^{n+1}\boldsymbol{u}^n\cdot\boldsymbol{w}d\Omega \quad \forall\,\boldsymbol{w}\in\mathcal{U} \end{aligned} \tag{4.11}$$

$$\int_\Omega \varphi^{n+1}\boldsymbol{\nabla}\cdot\boldsymbol{u}qd\Omega + \int_\Omega \boldsymbol{u}\cdot\boldsymbol{\nabla}\varphi^{n+1}qd\Omega = -\int_\Omega \dot{\varphi}^{n+1}qd\Omega \quad \forall\, q\in\mathcal{P}. \tag{4.12}$$

Thus, the step from t^n to t^{n+1}, follows by setting $\boldsymbol{u}^{n+1,0} = \boldsymbol{u}^n$ and solving the **Linearized problem** iteratively until convergence in k is reached. It is described by the following algorithm:

Algorithm 1 (Sequential Iterative Algorithm)

Step 1 Set the iteration index $k = 0$ and $\boldsymbol{u}^{n+1,k} = \boldsymbol{u}^n$.

Step 2 Given $\boldsymbol{u}^n$ and $\boldsymbol{u}^{n+1,k}$ find $\boldsymbol{u}^{n+1,k+1}$ and $p^{n+1,k+1}$ by solving the **Linearized Problem** (4.11)-(4.12)

Step 3 Check for convergence. If converged, set $\boldsymbol{u}^{n+1} = \boldsymbol{u}^{n+1,k+1}$ and $p^{n+1} = p^{n+1,k+1}$; otherwise advance $k = k + 1$ and go to step 2.

The convergence test, for given tolerances $\epsilon_{\boldsymbol{u}} > 0$ and $\epsilon_p > 0$, can verified through the conditions

$$||\boldsymbol{u}^{n+1,k+1} - \boldsymbol{u}^{n+1,k}|| < \epsilon_{\boldsymbol{u}} \tag{4.13}$$

and

$$||p^{n+1,k+1} - p^{n+1,k}|| < \epsilon_p, \tag{4.14}$$

or

$$||\boldsymbol{u}^{n+1,k+1} - \boldsymbol{u}^{n+1,k}|| < \epsilon_{\boldsymbol{u}}||\boldsymbol{u}^{n+1,k+1}|| \tag{4.15}$$

and

$$||p^{n+1,k+1} - p^{n+1,k}|| < \epsilon_p||p^{n+1,k+1}||, \tag{4.16}$$

designating the absolute and the relative errors, respectively.

4.3 Abstract variational problem

The variational formulation (Equations (4.11), and (4.12)) for the modified Navier-Stokes problem (Equation (2.19)) can be rewritten in the abstract form:

$$\begin{aligned} a(\boldsymbol{u}, \boldsymbol{w}) + b(\boldsymbol{w}, p) &= f(\boldsymbol{w}), \qquad \forall \boldsymbol{w} \in \mathcal{U}, \\ d(\boldsymbol{u}, q) &= g(q), \qquad \forall q \in \mathcal{P}, \end{aligned} \tag{4.17}$$

in which $a(\cdot,\cdot) : \mathcal{U} \times \mathcal{U} \to \mathbb{R}$, $b(\cdot,\cdot) : \mathcal{U} \times \mathcal{P} \to \mathbb{R}$, and $d(\cdot,\cdot) : \mathcal{U} \times \mathcal{P} \to \mathbb{R}$ are bilinear forms, $f(\cdot) : \mathcal{U} \to \mathbb{R}$ and $g(\cdot) : \mathcal{P} \to \mathbb{R}$ are linear continuous functionals given by

$$\begin{aligned} a(\boldsymbol{u}, \boldsymbol{w}) &= \int_\Omega \tilde{\varphi}\boldsymbol{u} \cdot \boldsymbol{w} d\Omega + \Delta t \int_\Omega \tilde{\varphi}[(\boldsymbol{\nabla u})\boldsymbol{u}_k] \cdot \boldsymbol{w} d\Omega + 2\mu\Delta t \int_\Omega \boldsymbol{\epsilon}(\boldsymbol{u}) : \boldsymbol{\epsilon}(\boldsymbol{w}) d\Omega \\ b(p, \boldsymbol{w}) &= -\Delta t \int_\Omega p\boldsymbol{\nabla} \cdot \boldsymbol{w} d\Omega \\ f(\boldsymbol{w}) &= \Delta t \int_\Omega \tilde{\varphi}\boldsymbol{f} \cdot \boldsymbol{w} d\Omega + \int_\Omega \tilde{\varphi}\boldsymbol{u}_a \cdot \boldsymbol{w} d\Omega + \Delta t \int_{\partial\Omega} \boldsymbol{t} \cdot \boldsymbol{w} d\Gamma \\ d(\boldsymbol{u}, q) &= \int_\Omega \tilde{\varphi}\boldsymbol{\nabla} \cdot \boldsymbol{u} q d\Omega + \int_\Omega \boldsymbol{u} \cdot (\boldsymbol{\nabla}\tilde{\varphi})\, q d\Omega \\ g(q) &= -\int_\Omega \dot{\tilde{\varphi}}^{n+1} q d\Omega, \end{aligned} \tag{4.18}$$

where $\boldsymbol{u}_k = \boldsymbol{u}^{n+1,k}$, $\boldsymbol{u}_a = \boldsymbol{u}^n$ and $\tilde{\varphi} = \rho\varphi^{n+1}$.

As in the Stokes problem approach (Chapter 2), the mixed approach and the introduction of a small compressibility scheme is also used here, and its implementation is analogous to the one explained in Sub-subsection 3.2.4.1. Thus, it is possible to express Equation (4.18) as a matrix form, as follows in the next section.

4.4 Matrix form

Using the function and approximation spaces defined in Subsections 3.2.1, and 3.2.2, respectively, and the linear expansions from Equation (3.19), it is possible to express Equations (4.17) as a linear system:

$$\begin{bmatrix} \boldsymbol{A} & \boldsymbol{B} \\ \boldsymbol{D} & \boldsymbol{C} \end{bmatrix} \begin{bmatrix} U_E \\ P_E \end{bmatrix} = \begin{bmatrix} F \\ G \end{bmatrix} \tag{4.19}$$

In which the submatrices of the continuity equation are:

- $\boldsymbol{C}$: $(np) \times (np)$, with elements

$$C_{l,k} = \frac{1}{\lambda} \int_\Omega \left[\bar{\phi}_l \bar{\phi}_k \right] d\Omega; \tag{4.20}$$

- $\boldsymbol{D}$: $(np) \times (2m)$, with elements

$$D_{l,2i-1} = \int_\Omega \left[\tilde{\varphi} \frac{\partial \phi_i}{\partial x} + \phi_i \frac{\partial \tilde{\varphi}}{\partial x} \right] \bar{\phi}_k d\Omega; \tag{4.21}$$

$$D_{l,2i} = \int_\Omega \left[\tilde{\varphi} \frac{\partial \phi_i}{\partial y} + \phi_i \frac{\partial \tilde{\varphi}}{\partial y} \right] \bar{\phi}_k d\Omega; \tag{4.22}$$

- G: $(np) \times 1$, with elements

$$G^e_{l,1} = -\int_\Omega \frac{\partial \tilde{\varphi}}{\partial t} \bar{\phi}_l d\Omega. \tag{4.23}$$

And the submatrices corresponding to the linear momentum conservation equation:

- $\boldsymbol{A}$: $(2m) \times (2m)$, with elements

$$A_{2i-1,2j-1} = \int_\Omega \Big[\tilde{\varphi} \phi_i \phi_j + \tilde{\varphi} \Delta t \left(\boldsymbol{u}_{k_1} \frac{\partial \phi_j}{\partial x} + \boldsymbol{u}_{k_2} \frac{\partial \phi_j}{\partial y} \right) \phi_i \tag{4.24}$$

$$+ \mu \Delta t \left(2 \frac{\partial \phi_i}{\partial x} \frac{\partial \phi_j}{\partial x} + \frac{\partial \phi_i}{\partial y} \frac{\partial \phi_j}{\partial y} \right) \Big] d\Omega; \tag{4.25}$$

$$A_{2i-1,2j} = \mu \Delta t \int_\Omega \frac{\partial \phi_j}{\partial y} \frac{\partial \phi_i}{\partial x} d\Omega; \tag{4.26}$$

$$A_{2i,2j-1} = \mu\Delta t \int_\Omega \frac{\partial\phi_j}{\partial x}\frac{\partial\phi_i}{\partial y} d\Omega; \tag{4.27}$$

$$A_{2i,2j} = \int_\Omega \Big[\tilde{\varphi}\phi_i\phi_j + \tilde{\varphi}\Delta t \left(\boldsymbol{u}_{k_1}\frac{\partial\phi_j}{\partial x} + \boldsymbol{u}_{k_2}\frac{\partial\phi_j}{\partial y}\right)\phi_i \tag{4.28}$$

$$+ \mu\Delta t \left(2\frac{\partial\phi_i}{\partial y}\frac{\partial\phi_j}{\partial y} + \frac{\partial\phi_i}{\partial x}\frac{\partial\phi_j}{\partial x}\right)\Big] d\Omega; \tag{4.29}$$

- $\boldsymbol{B}$: $(2m) \times (np)$, with elements

$$B_{2i-1,k} = -\Delta t \int_\Omega \frac{\partial\phi_i}{\partial x}\bar{\phi}_k d\Omega; \tag{4.30}$$

$$B_{2i,k} = -\Delta t \int_\Omega \frac{\partial\phi_i}{\partial y}\bar{\phi}_k d\Omega; \tag{4.31}$$

- F: $(2m) \times 1$, with elements

$$F^e_{2j-1,k} = \int_\Omega \Big[\tilde{\varphi}\Delta t f_1\phi_j + \tilde{\varphi}\boldsymbol{u}_{a_1}\phi_j\Big] d\Omega + \int_{\partial\Omega} (t_1\phi_j)\, dl; \tag{4.32}$$

$$F^e_{2j,k} = \int_\Omega \Big[\tilde{\varphi}\Delta t f_2\phi_j + \tilde{\varphi}\boldsymbol{u}_{a_2}\phi_j\Big] d\Omega + \int_{\partial\Omega} (t_2\phi_j)\, dl; \tag{4.33}$$

with $l, k = 1, \ldots, np$; $j, i = 1, \ldots, m$.

4.5 Numerical experiments

In this section, qualitative simulations are presented. They incorporate important components to simulate the blood flow through a heart chamber during a cardiac cycle, such as filling and ejection of fluid given through the variation of the capacitance function φ. In the first part, two different boundary conditions are explored, and some conclusions are outlined. Then, a problem with analytic solution is carried out, which is a relevant test before proceeding to the left ventricle case. All the simulations were made with mesh of 20×20 Q_2P_1 elements, density $\rho = 1$, viscosity $\mu = 1$, penalty parameter $\lambda = 10^8$, and time interval $I = [0, 1]$. In all the numerical experiments it was used the condition (4.15) with $\epsilon_{\boldsymbol{u}} = 10^{-2}$.

4.5.1 Study of boundary conditions

In this subsection the suitability of two types of boundary conditions (BCs) to be imposed on the mitral and aortic valves is discussed. The study of stability of BCs for the Navier-Stokes equations is a vast and intricate area in the literature. For example, it is known that prescribing only the pressure on the boundary is an ill-posed problem (FOUCHET-INCAUX, 2014). The mixed (Dirichlet-Neumann) boundary condition is often used, but its stability is not guaranteed for physiological problems (FOUCHET-INCAUX, 2014), (GRAVEMEIER et al., 2012), (HEYWOOD; RANNACHER; TUREK, 1996). This approach is particularly interesting for the problems addressed in this work, since it is necessary to impose artificial conditions on the chamber in order to simulate the real pressure inside it.

In what follows, a Poiseuille-type problem is simulated, by considering the flow between two flat plates separated by a distance $\bar{x}$. The domain is defined to be $\Omega = [0, \bar{x}] \times [0, 1]$ and the capacitance is set to be $\varphi = 1$. The time interval $I = [0, 1]$ was subdivided in 10 time steps. On the lateral edges of the domain, the homogeneous Dirichlet boundary condition $\boldsymbol{u} = \mathbf{0}$ was imposed, while on the upper and lower edges the pressure is $\bar{p}(x) = 11.0$ and $\bar{p}(x) = 1.0$, respectively.

On the upper and lower edges, two different mixed Dirichlet/traction conditions are tested. In the first boundary condition (BC1), the x-component of the velocity is (strongly) imposed as $u = 0$, and, the y-component of the traction vector is (weakly) set as

$$t_2(\boldsymbol{x}) = -\bar{p}(\boldsymbol{x}) n_y, \tag{4.34}$$

where $\bar{p}$ is the given pressure on the boundary and n_y is the y-component of the outward unit normal vector. The second boundary condition (BC2) differs from the first one by considering the full y-component of the traction vector

$$t_2(\boldsymbol{x}) = -\bar{p}(\boldsymbol{x}) n_y + 2\mu \frac{\partial v}{\partial y} n_y. \tag{4.35}$$

While the first part, associated to the pressure, is weakly imposed and goes to the right hand side of the system (source vector on the right hand side of the linear system (4.19)), the second part, associated to the y-component of the velocity, is

implicit and goes to the stiffness matrix, in the right hand side of the linear system (Equation (4.19)). It is similar to the imposition of Robin boundary conditions.

Figure 14 show the y-component velocity results for $x = 1.00$, $x = 0.10$, and $x = 0.01$ using BC1 and BC2. Note that when BC1 was used, the velocity profile was similar to the Poiseuille flow one (Subsection 3.2.5.3) in all the cases tested. However, when $x = 1.00$, the velocity profile resulted from the use of BC2 was totally different from the one using the former approach, and it approximates the Poiseuille flow profile as the distance between the plates diminishes.

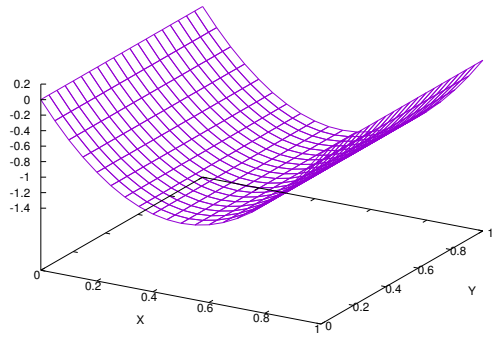

(a) $x = 1.00$.

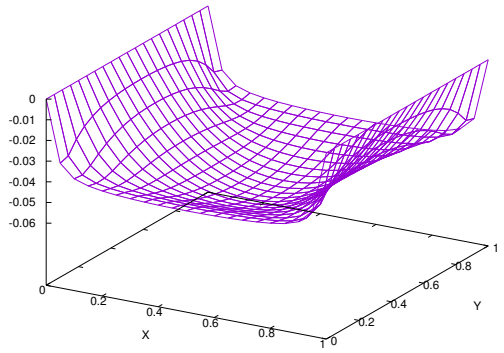

(b) $x = 1.00$.

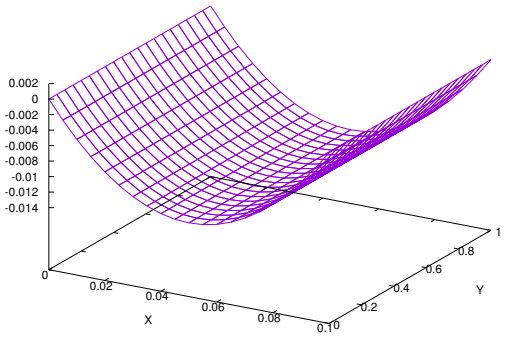

(c) $x = 0.10$.

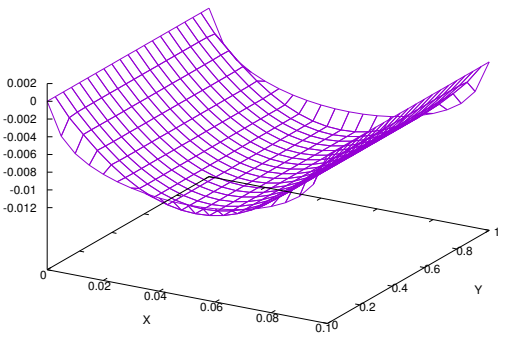

(d) $x = 0.10$.

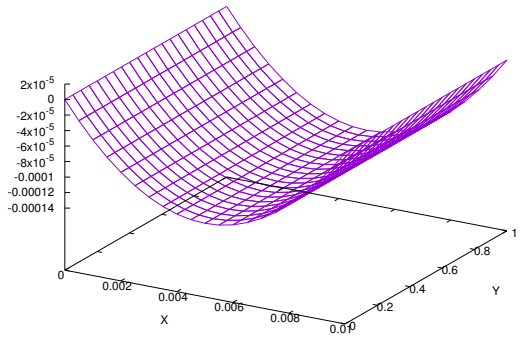

(e) $x = 0.01$.

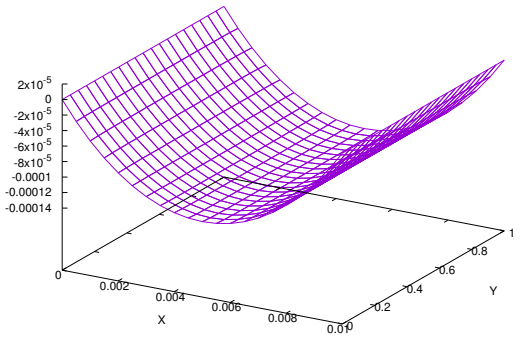

(f) $x = 0.01$.

Figure 14 – Flow between two flat plates separated by a distance x using BC1 (left), and BC2 (right): velocity profile in y direction.

4.5.2 Capacitance function varying in space and time

This test was specially constructed in order to compare the approximated solution in a case where the capacitance function varies in space and time and there is an analytic (exact) solution. To this end, consider Equations (2.16) in the domain $\Omega = [0,1]^2$, the time interval $I = [0,1]$, the capacitance function

$$\varphi = 1 - 0.9\text{sen}(\pi x)\text{sen}(\pi y)\text{sen}(\pi t), \tag{4.36}$$

and the sources

$$\boldsymbol{f} = \begin{bmatrix} -\pi\text{sen}(\pi x)\cos(\pi x)\left(1+3\cos^2\left(\frac{\pi y}{2}\right)\right) + \frac{4\pi^2}{\varphi}\cos(\pi x)\cos\left(\frac{\pi y}{2}\right) \\ \frac{\pi}{2}\text{sen}(\frac{\pi y}{2})\cos\left(\frac{\pi y}{2}\right)\left(1+3\cos^2(\pi x)\right) + \frac{\pi^2}{2\varphi}\text{sen}(\pi x)\text{sen}\frac{\pi y}{2} \end{bmatrix} \tag{4.37}$$

and

$$\begin{aligned} g = & -0.9\pi\cos(\pi t)\text{sen}(\pi x)\text{sen}(\pi y) \\ & + \cos\left(\frac{\pi y}{2}\right)(-2\pi\text{sen}(\pi x) - 1.8\pi\cos(2\pi x)\text{sen}(\pi t)\text{sen}(\pi y)) \\ & + \cos(\pi x)\left(-0.9\pi^2\cos(\pi y)\text{sen}(\pi t)\text{sen}(\pi x)\text{sen}\left(\frac{\pi y}{2}\right)\right. \\ & \left. + \cos\left(\frac{\pi y}{2}\right)\left(\frac{\pi^2}{2} - 0.45\pi^2\text{sen}(\pi t)\text{sen}(\pi x)\text{sen}(\pi y)\right)\right), \end{aligned} \tag{4.38}$$

where g is introduced in the right hand side of the first Equation of (2.19). This problem has the following analytic solution:

$$\boldsymbol{u} = \begin{bmatrix} 2\cos(\pi x)\cos\left(\frac{\pi y}{2}\right) \\ \pi\cos(\pi x)\text{sen}(\frac{\pi y}{2}) \end{bmatrix}, \quad p = \text{sen}(\pi t). \tag{4.39}$$

The simulation was done with the boundary condition type BC1 (refer to Subsection 4.5.1) on the upper edge of the domain, and on the remaining edges the homogeneous Dirichlet BC was imposed. The number of time steps was set to be 50. Figures 15a and 15b show the simulation results for velocity in x and y directions, respectively. Observe that, even though pressure and volume change with time, the velocity profiles are maintained static.

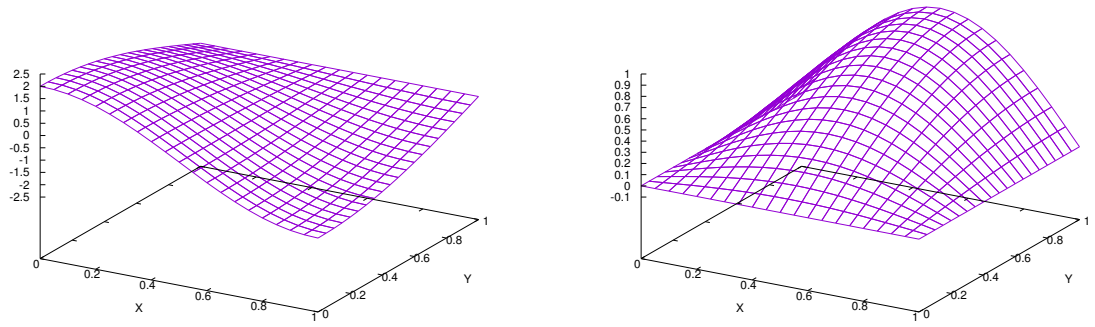

(a) Velocity profile in x direction (b) Velocity profile in y direction.

Figure 15 – Capacitance function varying in space and time with BC1: velocity profiles.

The resulting velocity field at $t = 1$ can be seen in Figure 16a, which is side-by-side to the pressure profile at $t = 1$ shown in Figure 16b. Note that pressure changes with time, but, at the last time step it is identically null.

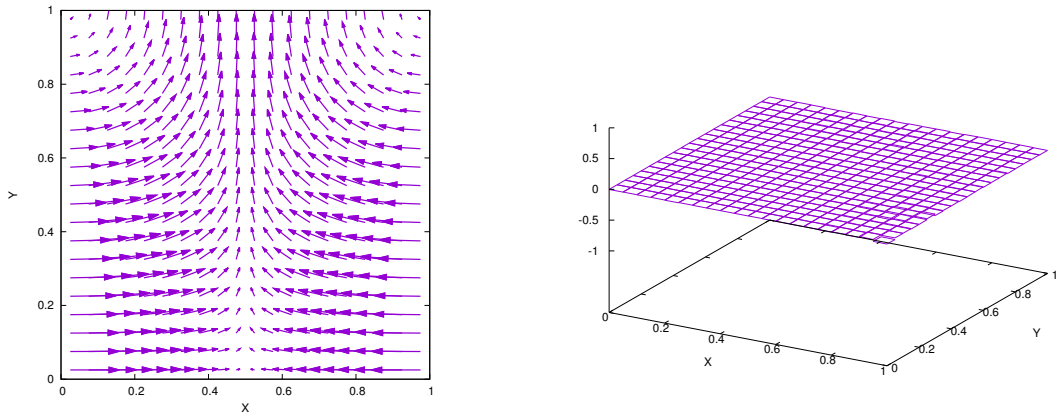

(a) Velocity field at $t = 1.0$. (b) Pressure profile at $t = 1.0$.

Figure 16 – Capacitance function varying in space and time with BC1: velocity field and pressure profile.

Figure 17a depicts the volume variation result using the Expression (4.36) for the capacitance function. Figure 17b shows the pressure variation with

time. Note that the average of pressure on the domain coincides with the pressure prescribed on the boundary using BC1.

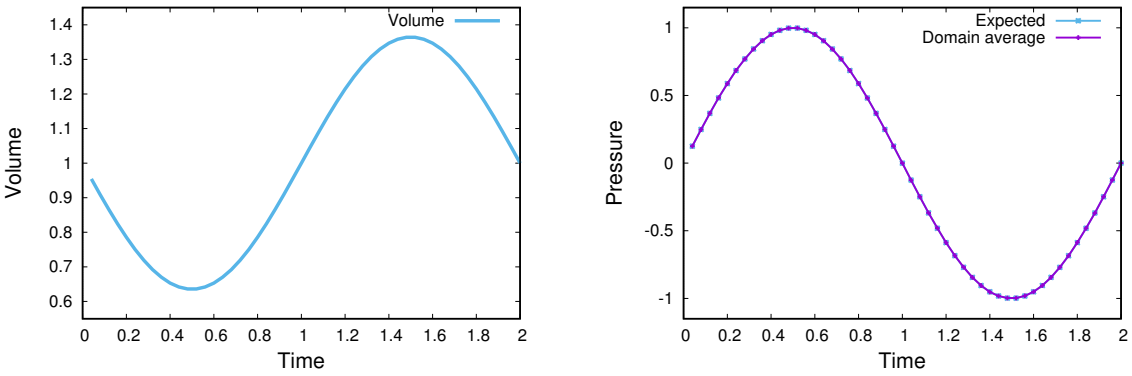

(a) Volume vs. time graph.

(b) Pressure vs. time graph.

Figure 17 – Capacitance function varying in space and time with BC1: volume vs. time and pressure vs. time graphs.

5 The Human Left Ventricle Simulation

In this chapter the model composed by the modified bidimensional Navier-Stokes equations, presented in Chapter 2, and the numerical methodology described in Chapters 3 and 4 will be used in the simulation of a healthy human left ventricle. All the hypotheses and experimental data are displayed at first, and then the results from the computational code simulation are shown and discussed.

Figure 18a shows the heart with its four chambers. Two atria and two ventricles, responsible for pumping blood into the pulmonary and systemic circulation. To do so, the heart goes through the so-called cardiac cycle, which is the period between the beginning of a heartbeat to the moment just before the next beat (HALL; GUYTON, 2011). The cardiac cycle is usually referred to using the left ventricle as a reference (Figure 18b), but the process is analogous for the four chambers. The cycle can be divided into two phases, an active phase and a passive one. In the active phase, the ventricular muscles contract from an electrical stimulus. Thus, the ventricular pressure increases isovolumetrically, and when it equals to the blood aortic pressure, the aortic valve opens causing the blood to flow through the artery. In this process, called systole, the pressure increases significantly, until the maximum systolic pressure (when blood ejection is still occurring), and, at the moment the pressure reaches values below those of blood pressure, the valve closes. Then, the isovolumetric phase of relaxation begins, and, soon, the mitral valve opens allowing the blood to flow from the atrium to the ventricle. This phase, just after the blood ejection, is called diastole (GUYTON; HALL, 2006). The $P \times V$ diagram of the cardiac cycle is indicated by red arrows in Figure 18b.

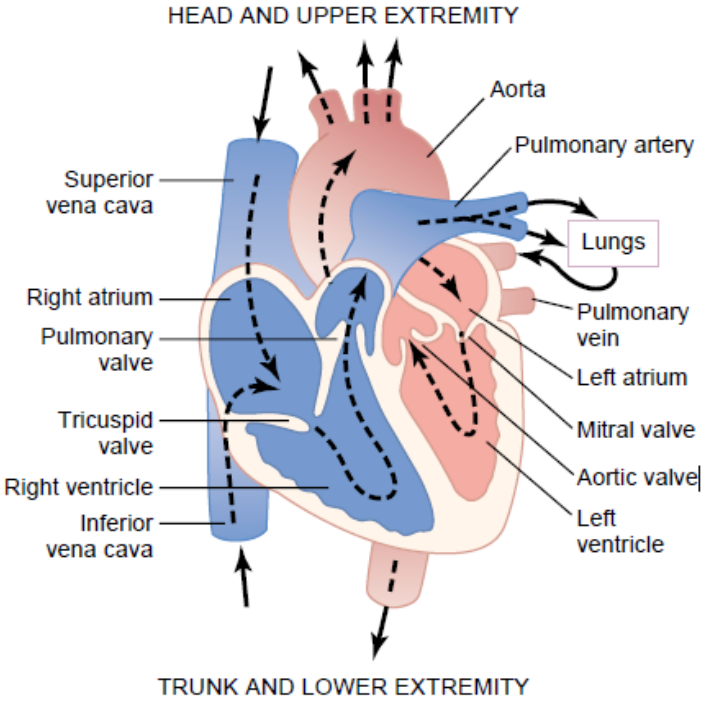

(a) Heart.

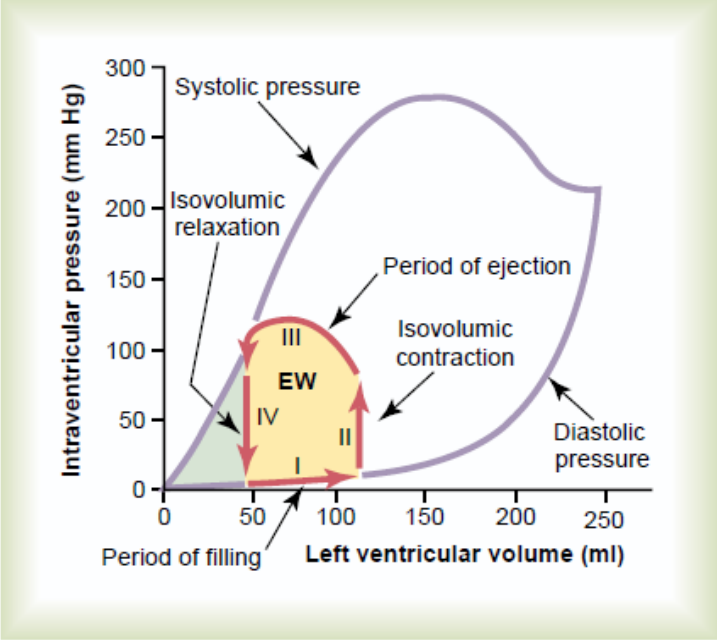

(b) Cardiac Cycle.

Figure 18 – Human heart and the cardiac cycle. From (GUYTON; HALL, 2006).

5.1 Cardiovascular parameters

According to American Heart Association (2018),the usual resting heart rate (RHR) ranges in general from 60 to 90 beats per minute. The simulations performed in this section consider that the heart frequency is 1Hz, *i.e.*, the RHR is equal 60 beats per minute. Furthermore, the simulations used the volume and pressure data for the left ventricle displayed in Table 4, that were taken from (BORON; BOULPAEP, 2012). The corresponding time scale was set to mimic a real cardiac cycle.

The end-diastolic volume is set to be 120 ml, and the stroke volume, 70 ml. In other words, the maximum volume is 120ml and the minimum volume that remains inside the ventricle (after the blood pump) is 50ml.

Table 4 – Data for a healthy human left ventricle from (BORON; BOULPAEP, 2012).

i	t_i (s)	P_i (mmHg)	V_i (ml)	Cardiac Phase $[t_i - 1, t_i)$
0	0.00	10	120	
1	0.05	80	120	Systole: Isovolumetric pressurization
2	0.20	120	75	Systole: Ejection
3	0.30	100	50	Systole: Ejection
4	0.45	7	50	Diastole: Isovolumetric relaxation
5	0.60	5	70	Diastole: Filling
6	1.00	10	120	Diastole: Filling

The notation settled for the ejection time interval is $I_{AV} = [t_1, t_3)$, and the filling one is $I_{MV} = [t_4, t_6)$. The indices AV and MV indicates the interval over which the valve is opened. The blood specific mass was set to be $\rho = 1059$ m^{-3}kg (WERNER; BUSE, 1988), and the dynamic viscosity, $\mu = 4 * 10^{-3}$Pa·s (BLICK; STEIN, 1977).

5.2 Results from the left ventricle simulation

Consider the ideal geometry for the left ventricle presented in Subsection 2.2.2, and set an uniform mesh of 20×20 quadrilateral elements. The number of

time steps for the ejection was set to be 40, whereas for the filling it was 50. Again, in all the numerical experiments it was used the condition (4.15) with $\epsilon_{\boldsymbol{u}} = 10^{-2}$. It is important to remark that, for this configuration, the number of iterations in k (Section 4.2) in each time step was always less than 5. Furthermore, in order to verify that the mass is numerically conserved, it was verified that the difference between the volumetric flow rate on the valves and the change in volume inside the chamber was about 0.27%.

During the isovolumetric processes — ventricle compression and relaxation — the velocity field was not solved, since it is expected that there is no flow during these periods. Then, the pressure was prescribed to be linear during both moments, as it is represented in the literature (BORON; BOULPAEP, 2012). In the ejection and filling processes, the pressure and volume functions where set to interpolate quadratically the data points shown in Table 4. The boundary conditions were set to be homogeneous Dirichlet $\boldsymbol{u} = \mathbf{0}$ on the fixed walls, from which there is no flux. On the valves, the pressure was prescribed using BC2 (refer to 4.5.1), but the following results are similar to the ones obtained when using BC1.

Figure 19b depicts the pressure versus time graph with the pressure prescribed on the boundary ("expected"), its average on the chamber, on the mitral and aortic valves. Figure 19a illustrates the volume versus time graph, which was simulated from the variation of the capacitance function φ. Both are similar to the ones from literature (HALL; GUYTON, 2011). Figure 20a shows the $P \times V$ diagram, with the prescribed and average pressure inside the chamber, and, on its side, there is a diagram from the literature (HALL; GUYTON, 2011).

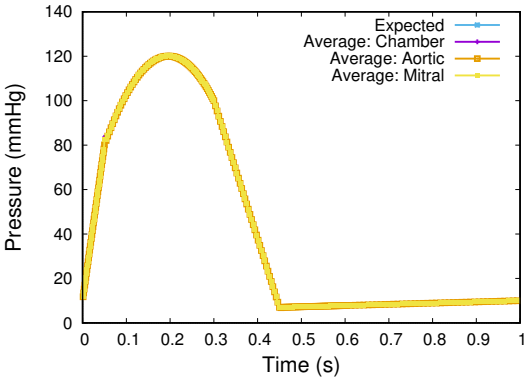

(a) $P \times t$ graph from author's code.

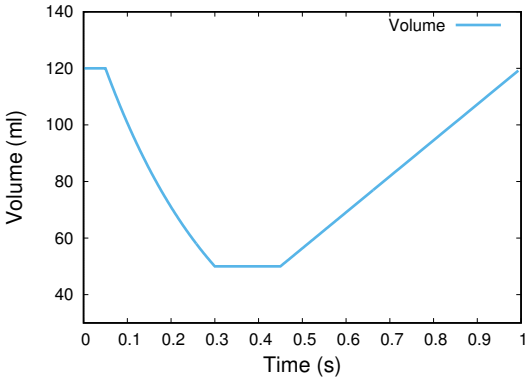

(b) $V \times t$ graph from author's code.

Figure 19 – Volume and pressure varying on time graphs during one cardiac cycle.

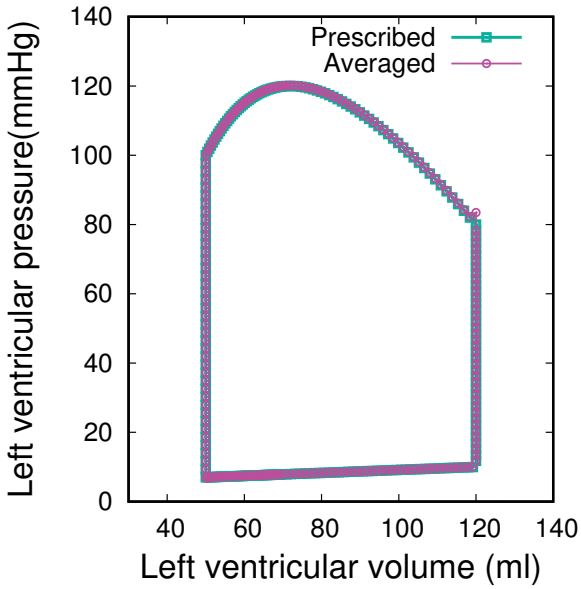

(a) From the author's code.

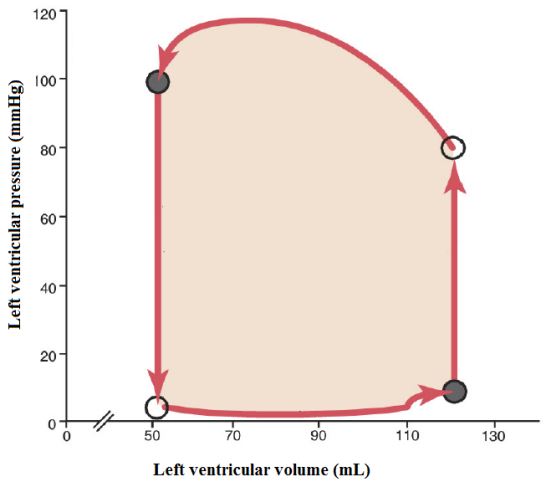

(b) From (HALL; GUYTON, 2011).

Figure 20 – Pressure vs. volume diagrams comparison.

The next figures compare the results obtained through the present model with simulation results from a model proposed on (OTTESEN; OLUFSEN; LARSEN, 2004), and with data from (JACOBSEN et al., 2001). In both models, the origin of time coincides with the beginning of the isovolumetric compression process, followed by the ejection, and so on (see Figure 23). However, the data

presented by Jacobsen et al. (2001) have the time origin defined at the beginning of the ventricle filling process, which explains the "shift" of time between the plots of blood velocity on the left ventricle valves (Figures 21 and 22).

The representative blood velocity pattern on the aortic and mitral annulus from the author's simulation are shown in Figure 21a, and 22a respectively. Note that, in both cases, the valve opening is subtle, which is represented in the figures as a dramatic growth/decay. Observe that in the case of the mitral valve, the velocity profile is flat. That happens because the capacitance function φ is close to a linear function of time during the filling process, another reason is that the pressure growth is minimal and slow (it takes 0.55 s). In the case of the aortic valve, the pressure change is more significant during the ejection, then the volume decay is close to a linear profile.

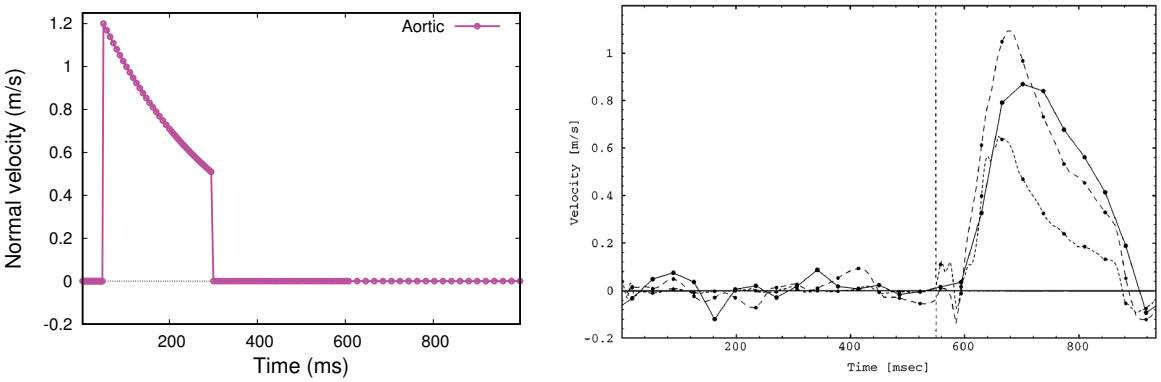

(a) From the author's code

(b) From (JACOBSEN et al., 2001).

Figure 21 – Blood velocity at the aortic valve vs. time comparison.

On the other hand, in Figures 21b, and 22b, Jacobsen et al. (2001) show relevant curves that serves as reference, from three different sources: Magnetic Ressonance data (solid curve), center velocity from a simulation (long-dashed curve), and mean velocity in that simulation (short-dashed curve).

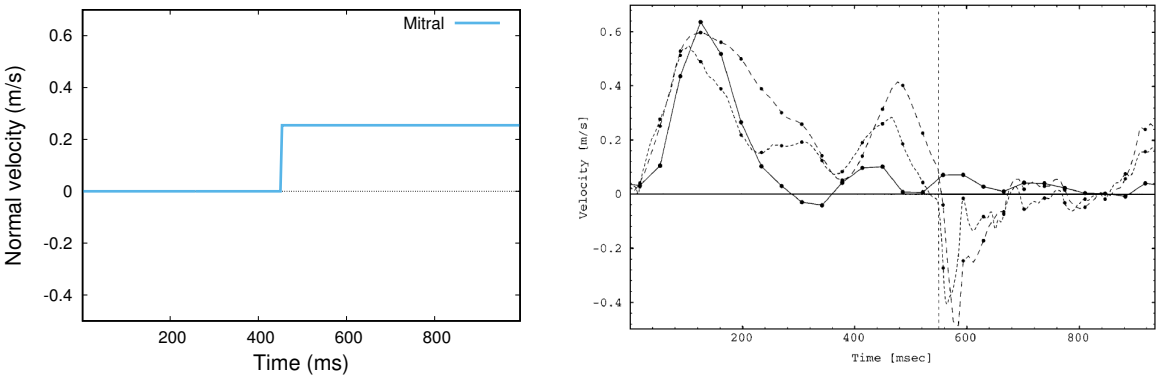

(a) From the author's code.

(b) From (JACOBSEN et al., 2001).

Figure 22 – Blood velocity at the mitral valve vs. time comparison.

Figure 23b shows the aortic outflow from a simulation reported in (OTTESEN; OLUFSEN; LARSEN, 2004), which considers a normal human ventricle ejecting blood into the arterial load. In this model, the end-diastolic volume is 125 ml, the stroke volume is 78 ml, and RHR is 1 Hz. These values are slightly different from the ones set to the present simulation (refer to Section 5.1), but the outflow magnitudes are of the same order. The function's shapes are distinct since the process of opening and closing the valves in the present work are subtle, while the code simulation from (OTTESEN; OLUFSEN; LARSEN, 2004) is from a model describing the heart as a pressure source depending on volume, time, and flow.

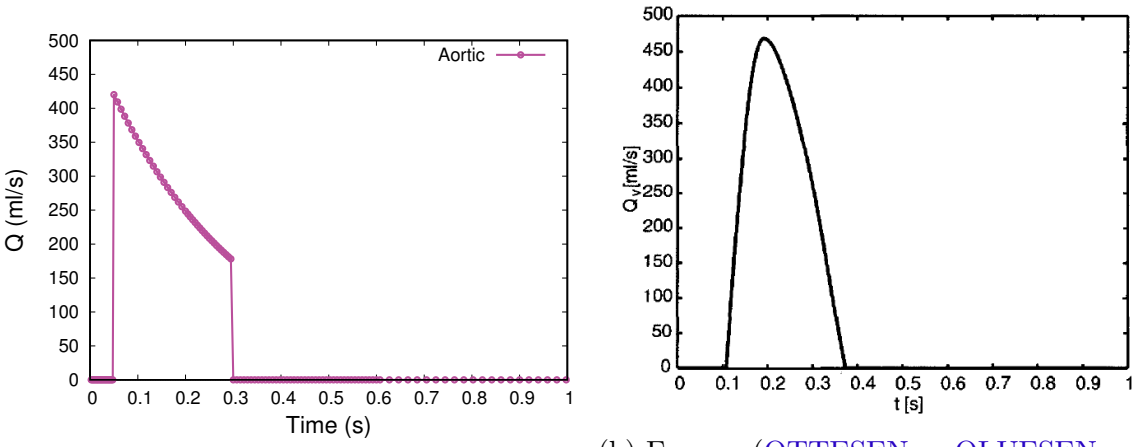

(a) From the author's code.

(b) From (OTTESEN; OLUFSEN; LARSEN, 2004).

Figure 23 – Aortic outflow vs. time graphs comparison.

Lets calculate the Reynolds number (Equation (3.1)). Define the typical velocity to be:

$$u_{av} = \frac{1}{(\Delta t)_V}\frac{1}{(\Delta x)_V}\int_{I_V}\left(\int_{\Gamma_V} \boldsymbol{u}\cdot\boldsymbol{n}dx\right)dt, \tag{5.1}$$

where Γ_V and $(\Delta x)_V$ are the boundary part that represents the referred valve and its length, respectively. In addition, I_V and $(\Delta t)_V$ are the interval over which there is outflow/inflow through it and its length, respectively. The results are shown in Table 5.

Table 5 – Reynolds number calculation in each left ventricle valve.

	Average velocity (m/s)	Valve length (m)	Reynolds number
AV	0.7926	0.0125	2623
MV	0.2569	0.0179	1217

The figures shown onward in this chapter resulted from the computational simulations. The physical unities used in their scales are in SI, *i.e.*, the velocity is expressed in meters per second, the Pressure in Pascal, and the capacitance function in meters.

Figure 24 shows the rectangular two-dimensional domain, defined in the Subsection 2.2.2, in perspective . The blood velocity field is illustrated on it at

different moments of the simulation, being respectively: at $t = 0.04$s and $t = 0.06$s (just before and soon after the beginning of the chamber ejection), at $t = 0.3$s (end of the ejection/just before the beginning of the isovolumetric compression), at $t = 0.44$s and $t = 0.46$s (just before and soon after the beginning of the chamber filling); and, finally, at $t = 0.98$s (at the end of the chamber filling). It is possible to see details of the velocity field at four different time frames in Figure 25, and in Figure 26 their corresponding magnitudes.

Recalling that the capacitance function φ was proposed in the Chapter 2 in order to allow the chamber volume variation on a fixed domain and mesh. In the present simulation, its profile is shown above the domain in Figure 24, which resembles a diaphragm.

At each time frame, the spatial pressure variation is minimal, but it is enough to cause the fluid to flow and to generate vortexes. The profile of velocity streamlines are illustrated on the domain of Figure 27. In the same figure, the pressure profile is represented as a plane that varies on the z axis at the same time frames mentioned for the velocity. Figure 28 shows the pressure magnitude in four different moments of the cycle. Note that the pressure magnitude is scaled over one cardiac cycle, that is, its upper limit is defined by the highest possible pressure value during a cardiac cycle. The same goes for the lower limit. This explains why the pressure seems to be a flat surface in Figure 27, and, in Figure 28, as one homogeneous color. However, when the pressure profile is scaled on each fixed time frame of Figure 28, it is possible to see the small variations over the domain. See Figure 29.

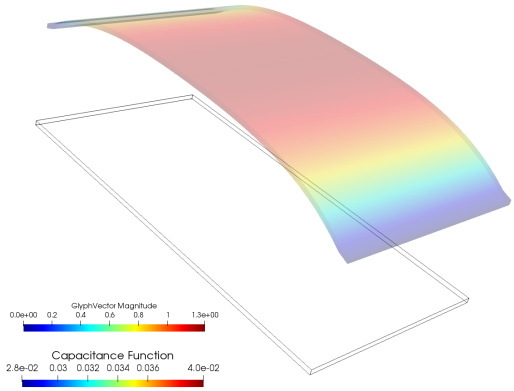

(a) $t = 0.04$s.

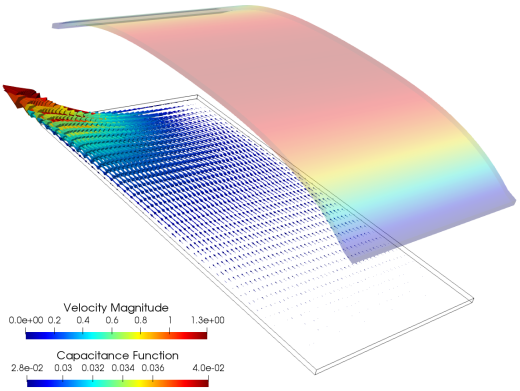

(b) $t = 0.06$s.

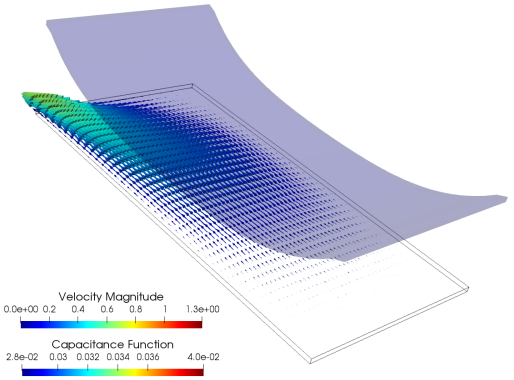

(c) $t = 0.30$s.

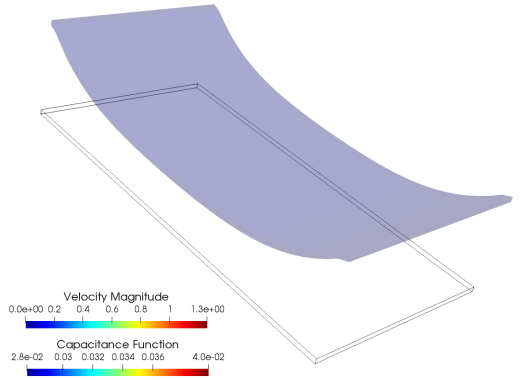

(d) $t = 0.44$s.

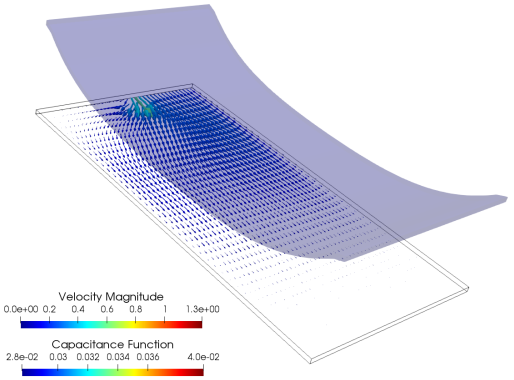

(e) $t = 0.46$s.

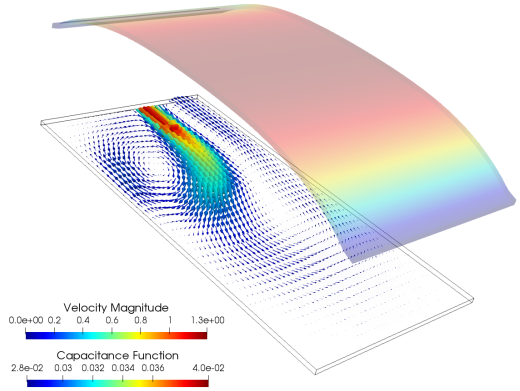

(f) $t = 0.98$s.

Figure 24 – Blood velocity field and the capacitance function at six time frames of the cardiac cycle.

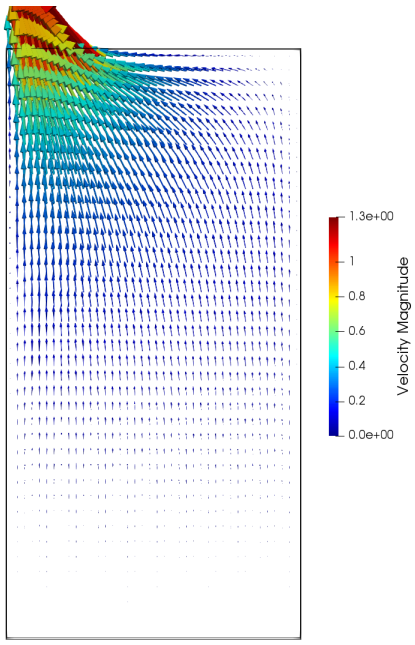

(a) $t = 0.06$s.

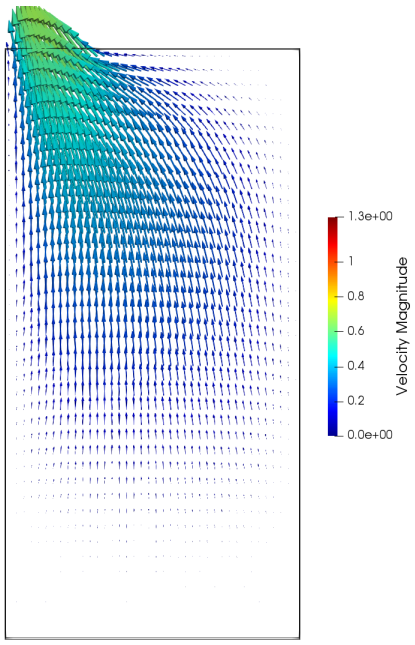

(b) $t = 0.30$s.

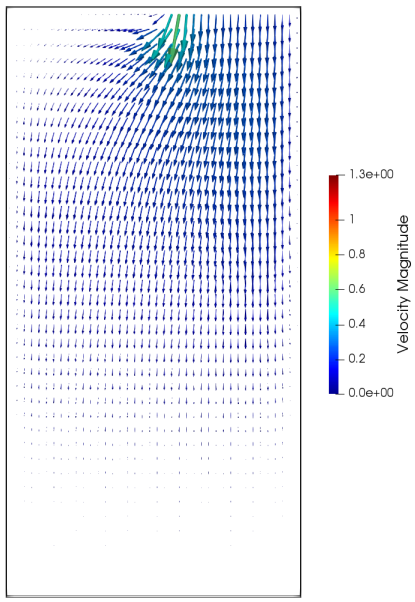

(c) $t = 0.46$s.

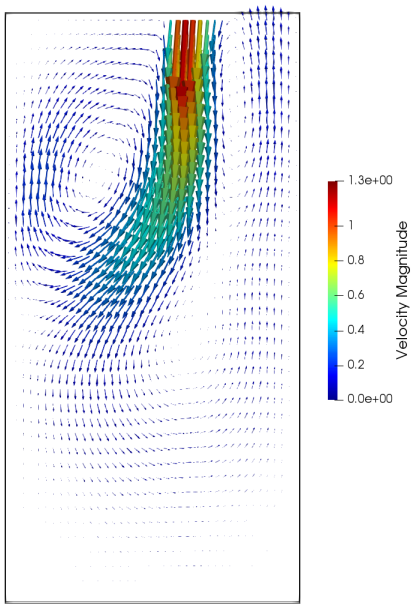

(d) $t = 0.98$s.

Figure 25 – Blood velocity field detailed in four different time frames of the cardiac cycle.

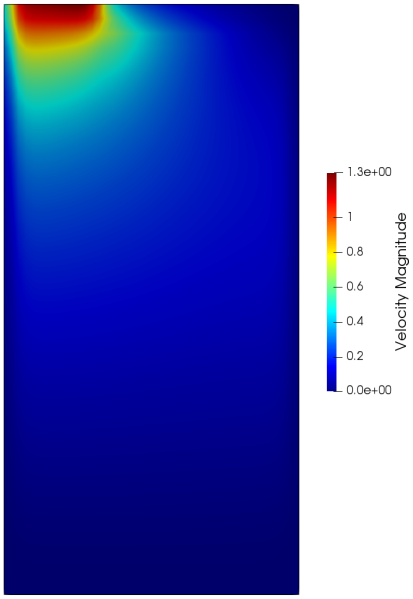

(a) $t = 0.06$s.

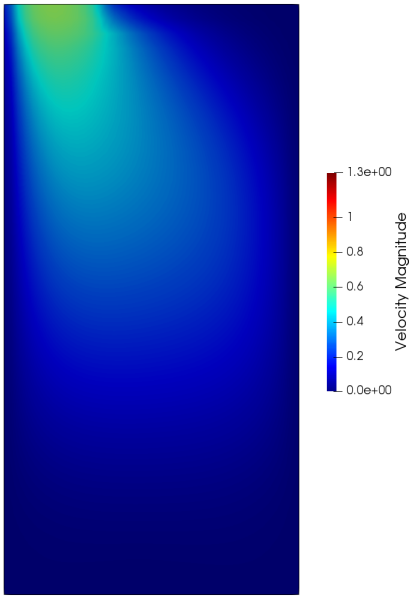

(b) $t = 0.30$s.

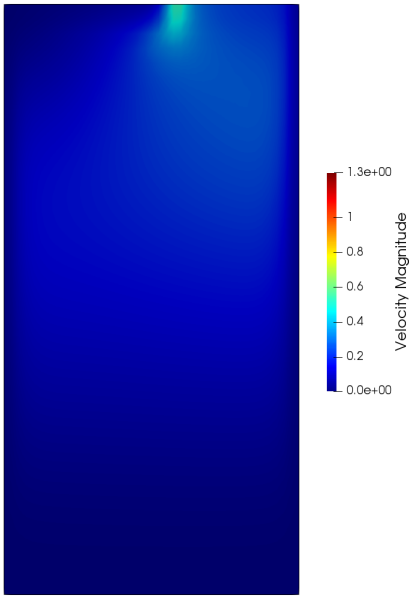

(c) $t = 0.46$s.

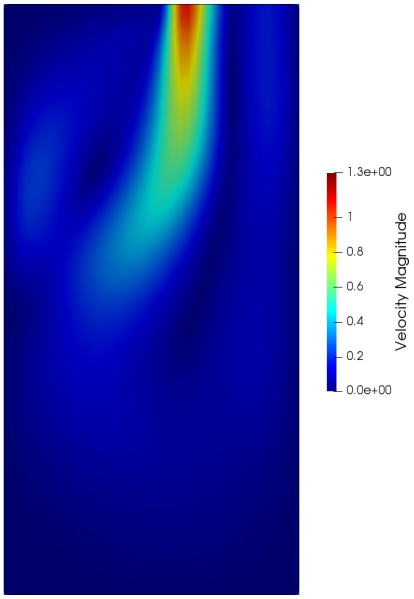

(d) $t = 0.98$s.

Figure 26 – Blood velocity magnitude detailed in four different time frames of the cardiac cycle.

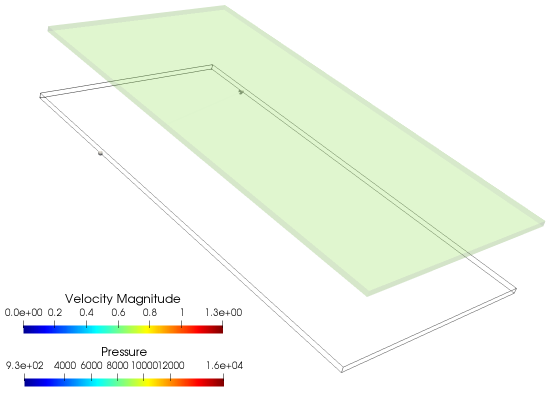

(a) $t = 0.04$s.

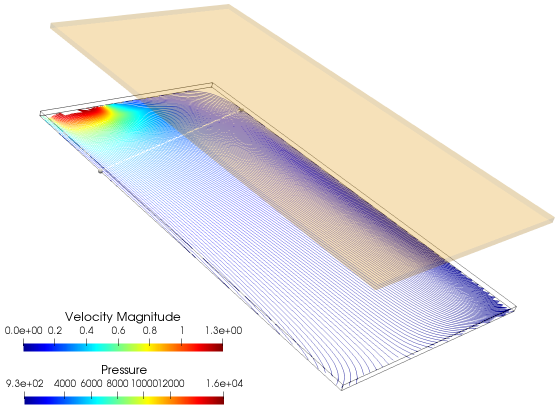

(b) $t = 0.06$s.

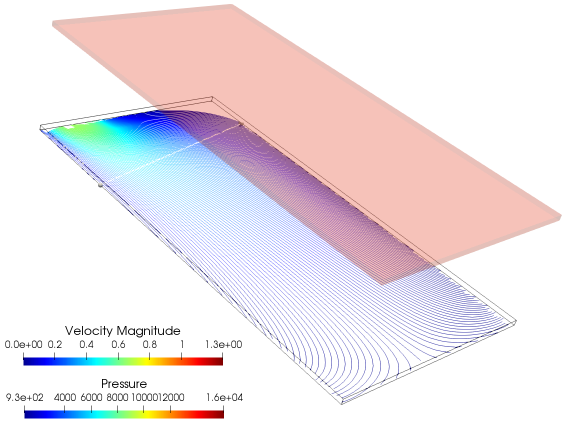

(c) $t = 0.30$s.

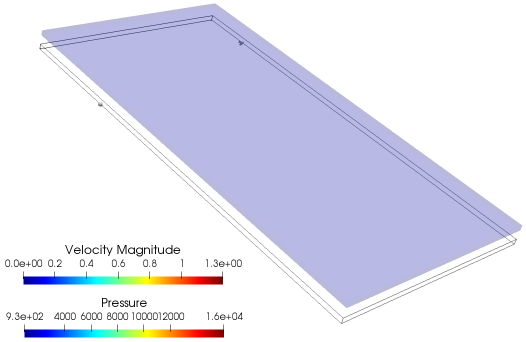

(d) $t = 0.44$s.

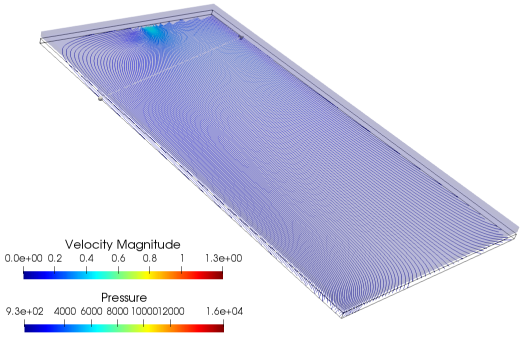

(e) $t = 0.46$s.

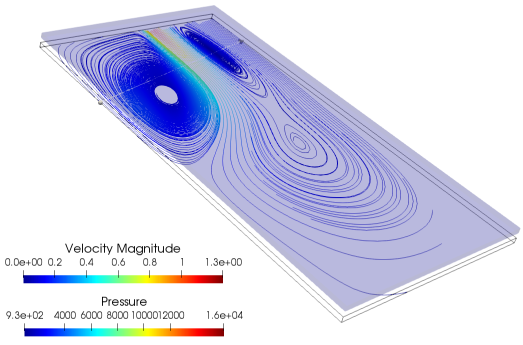

(f) $t = 0.98$s.

Figure 27 – Profile of velocity streamlines and the pressure profile at six time frames of the cardiac cycle.

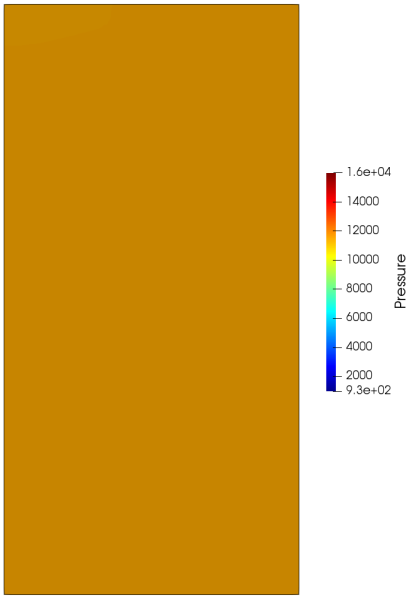

(a) $t = 0.06$s.

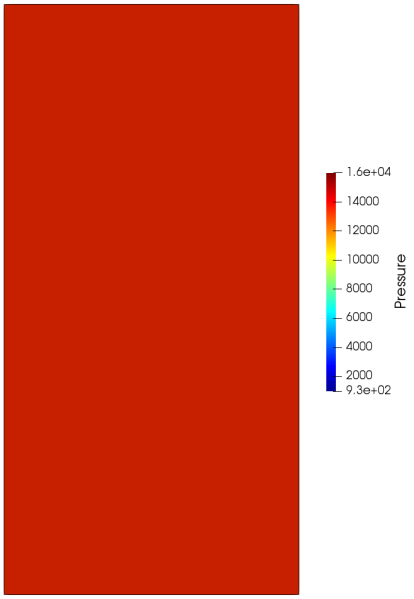

(b) $t = 0.30$s.

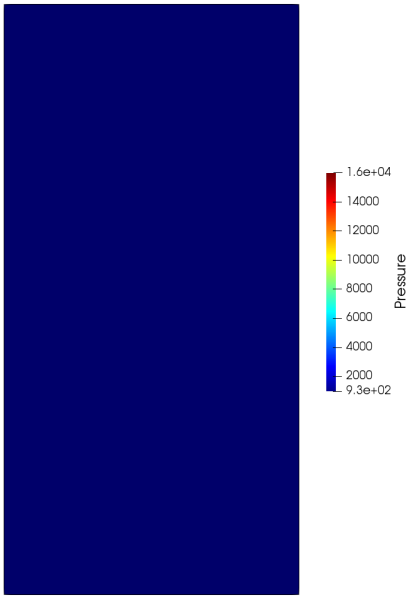

(c) $t = 0.46$s.

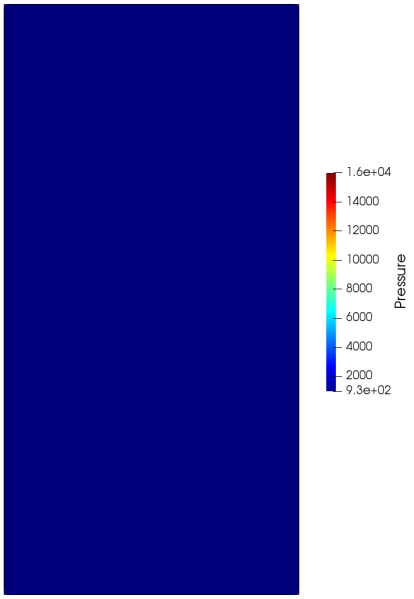

(d) $t = 0.98$s.

Figure 28 – Pressure magnitude scaled over the cardiac cycle in four different time frames of the cardiac cycle.

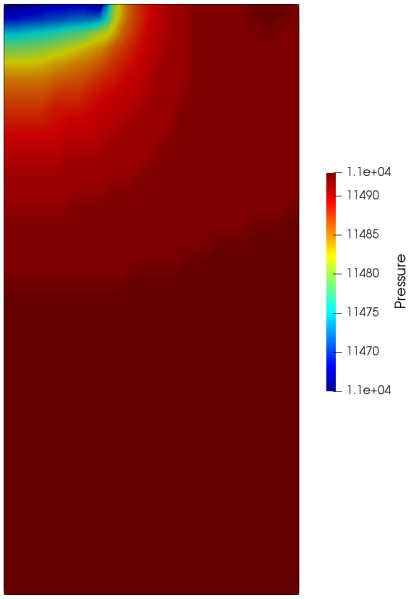

(a) $t = 0.06$s.

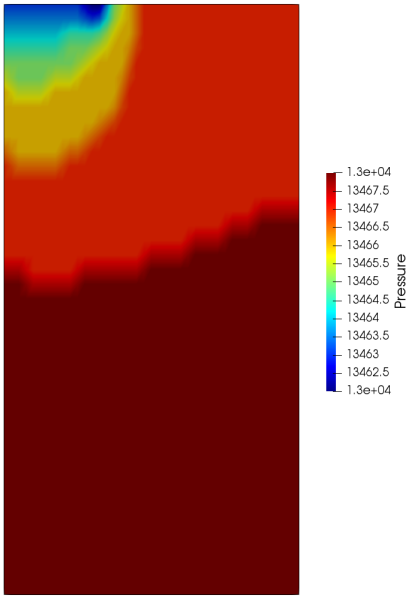

(b) $t = 0.30$s.

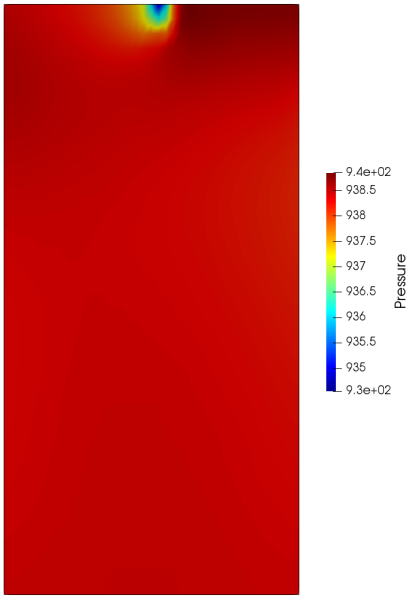

(c) $t = 0.46$s.

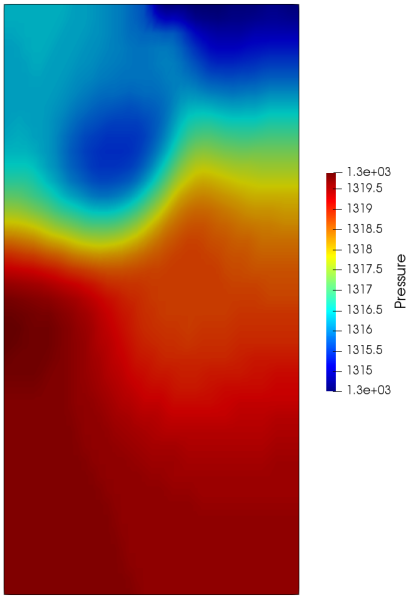

(d) $t = 0.98$s.

Figure 29 – Pressure magnitude scaled over the time frame in four different time frames of the cardiac cycle.

6 Thermodynamics analysis

In this chapter a thermodynamic model for the left ventricle is proposed, considering the cavity geometry presented in Subsection 2.2.2, and the calibration of parameters carried out in Chapter 5. As explained in Chapter 2, it is assumed that the thermodynamics does not affect the mass conservation equation and the physical properties of the fluid, but the flow does affect the energy balance. Thus, in this Chapter the First and Second Laws of Thermodynamics are applied to the model and the exergy analysis is applied in order to evaluate the quality of the energy conversion process in the human heart. Henceforth, the velocity magnitude is denoted as $\bar{u}$ in order to avoid an ambiguous notation with the internal energy u.

6.1 Thermodynamic model

From the left ventricle geometry of Figure 5, the thermodynamic model illustrated in Figure 30 is introduced. It comes up with a control volume (CV), which is placed outside the heart walls to take the heart metabolism M into account, then the cardiac muscle is considered to be inside the CV (HENRIQUES; MADY; OLIVEIRA-JUNIOR, 2016). The work W is considered to be performed on the CV since it is a result of external electrical stimulus (to contract the cardiac muscle). However, such a definition needs to be further discussed, because there is not a proper concept in the literature regarding the performed power by the cardiac muscle. Some key experiments can be found in (CAVAGNA; KANEKO, 1977; SMITH; BARCLAY; LOISELLE, 2005). The remaining energy is released as heat Q_M to the body.

This scheme is mathematically expressed in Equations (6.1), and (6.2) (MADY; OLIVEIRA-JUNIOR, 2013). The first expression indicates the energy conversion process in the metabolism, therefore, all the energy in the nutrients are converted into work or heat. From this process the energy is converted into flow work, internal energy variation and kinetic energy. Equation (6.2) represents the

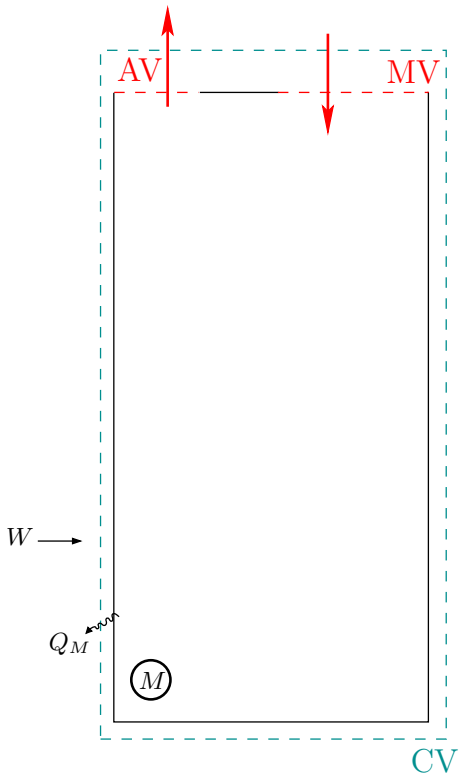

Figure 30 – Left ventricle thermodynamic model.

exergy analysis in the whole control volume, where it is clear that the part of the chemical exergy of the nutrients (B_M) is converted in a variation of the physical exergy, work, heat and the remain destroyed.

$$M = Q_M + W, \tag{6.1}$$

$$B_d = -\Delta B + B_M - B_{Q_M} - W. \tag{6.2}$$

6.1.1 Metabolism on an energy and exergy basis

Mady e Oliveira (2013) proposed Equations (6.3) to calculate the metabolism in energetic and exergy basis (in Joules) using thermodynamic properties obtained by Haynie (2008) as functions of oxygen consumption, carbon dioxide production, and nitrogen excreted from urine m_{O_2}, m_{CO_2}, m_N respectively.

$$\begin{aligned} M &= 1000(11371m_{O_2} + 2366m_{CO_2} + 6891m_N) \\ B_M &= 1000(9501m_{O_2} + 3963m_{CO_2} + 6979m_N) \end{aligned} \tag{6.3}$$

However, according to Mady e Oliveira (2013) for a healthy person in basal conditions or under physical activities, the oxidation of proteins can be disregarded (maximum contribution of 3%). Since the term of m_N comes from the oxidation of proteins, its value is negligible. Then the following expression will be carried out to calculate the metabolism in energy and exergy bases:

$$\begin{aligned} M &= 1000(11371m_{O_2} + 2366m_{CO_2}) \\ B_M &= 1000(9501m_{O_2} + 3963m_{CO_2}) \end{aligned} \tag{6.4}$$

The authors conclude that the approximation $B_M \approx M$, as previously reported in (BATATO et al., 1990), is valid in basal conditions and may also hold during physical activities. One point that was evaluated, and which is not analyzed in the literature, is the entropy variation of reaction of oxidation. The values of absolute entropy of glucose and palmitic acid were obtained from Annamalai e Silva (2012). Hence, it results that

$$S_M = 1000(-5.9029m_{O_2} + 5.2790m_{CO_2}). \tag{6.5}$$

Another relevant result was obtained by Takaoka et al. (1992) from human experimental data: a linear relationship between the myocardial oxygen consumption (V_{O_2}) and the systolic pressure-volume area (PVA), which is the shaded area shown in Figure 31. From the value determined for PVA, it is possible to calculate m_{O_2} using the specific mass of O_2 at $T = 37°\text{C}$ and $p = 1\text{atm}$, while m_{CO_2} can be calculated using the respiratory quotient (RQ), which is the ratio of the carbon dioxide production to oxygen consumption (on a molar or volumetric basis). This parameter is 1 for glucose, 0.7 for palmitic acid, and 0.83 for amino acids. The assumption that RQ is 0.83 for basal conditions is reliable according to Mady e Oliveira-Junior (2013), nevertheless it is well established in medical literature that the myocardial (biggest heart muscle) consumes 70% of lipids and 30% of glucose (HALL; GUYTON, 2011).

It is important to highlight that the metabolism of the blood (hemoglobin and leukocytes) was neglected in this analysis, because, according to (DALAND; ISAACS, 1927), this amount is not representative for healthy individuals.

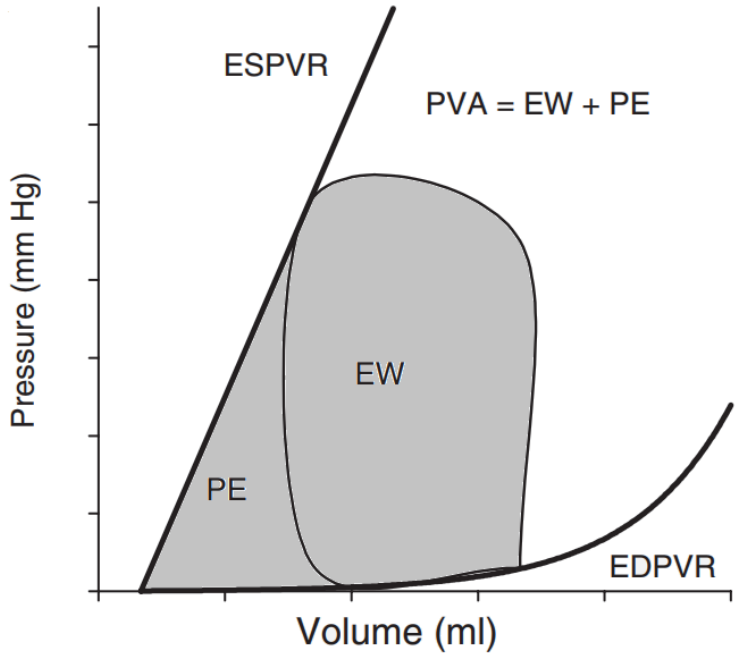

Figure 31 – Systolic pressure-volume area (PVA). From (STEENDIJK; ELLEN, 2008).

6.2 Thermodynamics laws

In the next two subsections, the First and Second Laws will be carried out using the results from numerical simulations. From the First Law it will be possible to figure out if the blood is heated during the moment it is inside the ventricle, and, then, from the Second Law, by mean of the exergy analysis, the destroyed exergy (or quality of energy conversion process) can be evaluated.

Besides, in Thermodynamics there is a convention that if the physical quantity is a property, — *i.e.*, it is a function of point, and, consequently, does not depend on the path — the traditional notation is used for its derivative, and if the derivative is taken over time, it is represented as an overdot $\dot{x} \equiv \frac{dx}{dt}$. Nevertheless, heat and work are types of energy transfer from the control volume to the environment, they path functions, and therefore, depends on the path in which the energy conversion process occurs. Then their derivatives are often called material derivatives. In order to facilitate the notation, the latter derivatives over

time will also be denoted as an overdot, such as, $\dot{W} \equiv \frac{\delta W}{dt}$.

6.2.1 The First Law of Thermodynamics

During the cardiac cycle, each heart activity must be in permanent regime, because there is no resting heart rate (RHR) increase, neither of volume nor temperature, that is, it is expected that there is no energy variation of the heart over the time. Then, the First Law of Thermodynamics can be expressed as:

$$\begin{aligned} 0 = \frac{dU_{VC}}{dt} &= \sum_i \dot{m}_i(h_i + \frac{\bar{u}_i^2}{2} + gz_i) - \sum_e \dot{m}_e(h_e + \frac{\bar{u}_e^2}{2} + gz_e) + \dot{M} + \dot{W} \\ &= \sum_i \dot{m}_i(h_i + \frac{\bar{u}_i^2}{2} + gz_i) - \sum_e \dot{m}_e(h_e + \frac{\bar{u}_e^2}{2} + gz_e) + \dot{M} + \dot{W}, \end{aligned} \tag{6.6}$$

in which $\dot{m}$ is the mass flow rate, h is the specific enthalpy, $\bar{u}$ is the magnitude of blood velocity, g is the gravitational acceleration, and z is the height of flow rate. The indices i and e indicates when there is an inflow and outflow (exit) of a mass associated with the referred property.

Furthermore, the input comes through the mitral valve (MV) and the output goes through the aortic valve (AV), then the terms of potential energy cancel out.

Thus, Equation (6.6) can be rewritten as:

$$\begin{aligned} 0 &= \dot{m}_i(h_i + \frac{\bar{u}_i^2}{2}) - \dot{m}_e(h_e + \frac{\bar{u}_e^2}{2}) + \dot{M} + \dot{W} \\ &= \dot{m}_i(u_i + \frac{p_i}{\rho} + \frac{\bar{u}_i^2}{2}) - \dot{m}_e(u_e + \frac{p_e}{\rho} + \frac{\bar{u}_e^2}{2}) + \dot{M} + \dot{W} \end{aligned} \tag{6.7}$$

Then, integrating it over time,

$$\begin{aligned} m(u_e - u_i) = &\frac{1}{\rho}\left(\int_{I_{MV}} \dot{m}_i p_i dt - \int_{I_{AV}} \dot{m}_e p_e dt\right) \\ &+ \frac{1}{2}\left(\int_{I_{MV}} \dot{m}_i \bar{u}_i^2 dt - \int_{I_{AV}} \dot{m}_e \bar{u}_e^2 dt\right) + M + W, \end{aligned} \tag{6.8}$$

where m is the mass of the stoke volume, *i.e.*, the total mass that comes in the ventricle during the filling process, that is the same amount that leaves during the ejection process.

Usually, incompressible fluids passing though expansion valves with low pressure difference have not only the isenthalpic behavior, but also isothermal behavior, since for the blood $dh = cdT$, where c is the blood specific heat, considered as $c = 3850$ J °C^{-1}kg^{-1} (WERNER; BUSE, 1988), and T is its temperature. Therefore, it was considered that the temperature of the blood does not change in the MV and AV during the filling and ejection process. Finally, the First Law of thermodynamics for this system is:

$$\begin{aligned} mc(T_e - T_i) = \frac{1}{\rho}\left(\int_{I_{MV}} \dot{m}_i p_i dt - \int_{I_{AV}} \dot{m}_e p_e dt\right) \\ + \frac{1}{2}\left(\int_{I_{MV}} \dot{m}_i \bar{u}_i^2 dt - \int_{I_{AV}} \dot{m}_e \bar{u}_e^2 dt\right) + M + W. \end{aligned} \tag{6.9}$$

Observe that, the work W is the area enclosed by the diagram $P \times V$ shown in Figure 20a:

$$W = \int_{V_4}^{V^6} p(V) dV, \tag{6.10}$$

where V_4 and V_6 where defined in Section 5.1. Besides, all the terms on the right side of the equation (6.9) are available from the solution of the Navier-Stokes equations within the geometry of Figure 30. Thus, defining a temperature of blood inflow, it is possible to determine the exit temperature T_e.

6.2.2 The Second Law of Thermodynamics

Consider that there is no variation of the entropy property of the heart during one cardiac cycle, the Second Law of Thermodynamics can be written as:

$$0 = \frac{dS_{VC}}{dt} = -\dot{S}_M + \dot{m}_i s_i - \dot{m}_e s_e + \frac{\dot{Q}_M}{T_0} - \frac{\dot{Q}_M}{T_{ml}} + \dot{\sigma}, \tag{6.11}$$

in which σ stands for the entropy generated due to irreversibilities, s_i, and s_e are the inlet and outlet specific entropies, respectively, T_0 is set to be the environmental temperature $T_0 = 25$°C, and

$$T_{ml} = \frac{T_e - T_i}{\ln(T_e/T_i)}$$

is the logarithmic mean temperature, that is the representative temperature at which a heat exchange process leads to no irreversibility, *i.e.*, $\sigma = 0$ (NEVERS;

SEADER, 1980). In the present case, $\sigma \neq 0$ because there are irreversibilities, such as the heat exchange between T_0 and T_{ml}. Now, isolating $\dot{\sigma}$ in (6.11):

$$\dot{\sigma} = \dot{S}_M + \dot{m}_e s_e - \dot{m}_i s_i - \dot{Q}_M \left(\frac{1}{T_0} - \frac{1}{T_{ml}} \right), \tag{6.12}$$

where $Q_M > 0$.

From the Gibbs relation,

$$\dot{m}_e s_e - \dot{m}_i s_i \approx c(\dot{m}_e \ln(T_e) - \dot{m}_i \ln(T_i)) - \frac{1}{\rho T_e} \dot{m}_e p_e + \frac{1}{\rho T_i} \dot{m}_i p_i. \tag{6.13}$$

Then, integrating Equation (6.12) on time, one gets:

$$\begin{aligned} \sigma = S_M + mc \ln \left(\frac{T_e}{T_i} \right) - \frac{1}{\rho T_e} \int_{I_{AV}} \dot{m}_e p_e dt \\ + \frac{1}{\rho T_i} \int_{I_{MV}} \dot{m}_i p_i dt - Q_M \left(\frac{1}{T_0} - \frac{1}{T_{ml}} \right). \end{aligned} \tag{6.14}$$

6.3 Exergy analysis

The equation for exergy is a combination of equations for the First and Second Laws of Thermodynamics (KOTAS, 1985). Multiplying Equation (6.14) by $-T_0$ and summing the result with Equation (6.9), one obtains:

$$\begin{aligned} \Delta B &= B_e - B_i \\ &= mc \left[T_e - T_i - T_0 \ln \left(\frac{T_e}{T_i} \right) + T_0 \left(\frac{1}{\rho T_e} \int_{I_{AV}} \dot{m}_e p_e dt - \frac{1}{\rho T_i} \int_{I_{MV}} \dot{m}_i p_i dt \right) \right] \\ &+ \frac{1}{2} \int_{I_{AV}} \dot{m}_e \bar{u}_e^2 dt - \frac{1}{2} \int_{I_{MV}} \dot{m}_i \bar{u}_i^2 dt \end{aligned} \tag{6.15}$$

Additionally, the exergy associated with the heat exchange at an average temperature of blood between temperature T_0 and T_{ml} is

$$B_{QM} = Q_M \left(1 - \frac{T_0}{T_{ml}} \right). \tag{6.16}$$

Thus, based on (HENRIQUES et al., 2017), the destroyed exergy is defined as:

$$B_d = -\Delta B - B_{QM} + B_M + W. \tag{6.17}$$

A remarkable result for the exergy analysis is the relation between the destroyed exergy B_d and the entropy generation σ given by the Guoy-Stodola theorem (NEVERS; SEADER, 1980), and expressed in Equation (6.18):

$$B_d = T_0\sigma, \tag{6.18}$$

which will be used to validate the consistency of the thermal model.

The advantage of the exergy analysis in relation solely of the Second Law of Thermodynamics is the possibility to propose performance parameters based on the maximum available work, lost work and the desired effect. For the heart, two efficiencies may be considered, according to Equations (6.19) and (6.20):

$$\eta_1 = \frac{\Delta B}{B_M}, \tag{6.19}$$

$$\eta_2 = \frac{B_M + W - B_d}{B_M + W}. \tag{6.20}$$

While the First Law of Thermodynamics may evaluate the efficiency based only on the performed work of the heart and the metabolism, therefore defined as the ratio of W to B_M.

6.4 Results

In this section, the simulation outputs for the Laws of Thermodynamics (Sections 6.2.1 and 6.2.2) and for the exergy analysis (Section 6.3) are presented together with the conclusions.

6.4.1 Calculation of the integrals

In order to calculate the integrals that appear on the Laws of Thermodynamics expressions, the values of p_i, p_e, $\bar{u}_i$, and $\bar{u}_e$ were defined to be the average

on each of the valves:

$$\begin{aligned} p_i^* &= \frac{1}{\Delta x_{MV}} \int_{\Gamma_{MV}} p(\boldsymbol{x}) dl, \\ p_e^* &= \frac{1}{\Delta x_{AV}} \int_{\Gamma_{AV}} p(\boldsymbol{x}) dl, \\ \bar{u}_i^* &= \frac{1}{\Delta x_{MV}} \int_{\Gamma_{MV}} \boldsymbol{u}(\boldsymbol{x}) \cdot \boldsymbol{n} dl, \\ \bar{u}_e^* &= \frac{1}{\Delta x_{AV}} \int_{\Gamma_{AV}} \boldsymbol{u}(\boldsymbol{x}) \cdot \boldsymbol{n} dl, \end{aligned} \tag{6.21}$$

in which Δx_{AV}, and Δx_{MV} are the AV and MV lengths, $\boldsymbol{u}(\boldsymbol{x}) \cdot \boldsymbol{n}$ is the normal velocity component at each of the valves, and $p(\boldsymbol{x})$ is the pressure at point $\boldsymbol{x}$ of the space. The values of $\dot{m}_i$, and $\dot{m}_e$ were calculated as shown in Equation (6.22).

$$\begin{aligned} \dot{m}_e &= \varphi_0 \int_{\Gamma_{AV}} \rho \boldsymbol{u}(\boldsymbol{x}) \cdot \boldsymbol{n} dl, \\ \dot{m}_i &= \varphi_0 \int_{\Gamma_{MV}} \rho \boldsymbol{u}(\boldsymbol{x}) \cdot \boldsymbol{n} dl. \end{aligned} \tag{6.22}$$

Then, the results calculated for each integral are:

$$\begin{aligned} &\int_{I_{MV}} \dot{m}_i p_i^* dt = 79.4596\,\mathrm{J m^3 kg^{-1}}, \\ &\int_{I_{AV}} \dot{m}_e p_e^* dt = 1128.2980\,\mathrm{J m^3 kg^{-1}}, \\ &\int_{I_{MV}} \dot{m}_i (\bar{u}_i^*)^2 d = 4.7486\,\mathrm{J}, \\ &\int_{I_{AV}} \dot{m}_e (\bar{u}_e^*)^2 dt = 5.6275\,\mathrm{J}. \end{aligned} \tag{6.23}$$

6.4.2 Metabolism

The systolic pressure-volume area (PVA) was approximated to be the area of the PV-diagram (Figure 20a) plus the area of the triangle defined by the vertices: the origin of the Cartesian system, and the two closest vertices of the $P \times V$ cycle to the origin. Then, PVA was used to calculate the myocardial oxygen consumption V_{O_2}, consequently, the oxygen consumption m_{O_2}, and the carbon dioxide production m_{CO_2} were obtained. Hence, from Equations (6.4), and (6.5),

it was possible to obtain the heart metabolism in energy (M), entropy (S_M), and exergy (B_M) bases. All results are shown in Equations (6.24), (6.25), and (6.26).

$$M = 3.1786\,\text{J}, \tag{6.24}$$

$$S_M = -0.0007\,\text{J}, \tag{6.25}$$

$$B_M = 2.9536\,\text{J}. \tag{6.26}$$

Remember that it was expected that $B_M \approx M$, and, in fact, the relative error between them is relatively small:

$$100\left(\frac{B_M - M}{B_M}\right) \approx 7\%. \tag{6.27}$$

6.4.3 First Law of Thermodynamics

Subsequently, the rest of the terms appearing in the First Law of Thermodynamics (Equation 6.6) were calculated. Starting with the work done by the left ventricle during one cardiac cycle:

$$W = 0.9292\,\text{J}, \tag{6.28}$$

from which, together with the metabolism value (Expression (6.24)), it was possible to determine the heat released to the body:

$$Q_M = 4.1077\,\text{J}. \tag{6.29}$$

Since the stroke volume is 70ml, then, multiplying it by the specific mass given in Chapter 5, it turns out that the "stroke mass" is $m = 0.0741\text{kg}$. Having those results on hand together with the integrals' results shown earlier, it was possible to determine the blood temperature increase from the moment it is pulled into the chamber until the moment it is pumped out to the body:

$$T_e - T_i = 0.0108\,\text{K}, \tag{6.30}$$

and setting $T_i = 310.1500\,\text{K} = 37.0000\,^\circ\text{C}$ to be the average body temperature, it turns out that

$$\begin{aligned} T_e &= 310.1608\,\text{K} \\ &= 37.0108\,^\circ\text{C}. \end{aligned} \tag{6.31}$$

These temperatures values were left with four more decimals, because they show that the increase in the temperature of the blood is almost negligible, which is justified by the small period that the blood remains in the organ. Another point is that the heart is one of the organs with highest metabolism and highest temperature, justifying its temperature assumption to be 37 ^{o}C (FERREIRA; YANAGIHARA, 2009).

6.4.4 Second Law of Thermodynamics

Moving forward to the Second Law of Thermodynamics, the calculation results for all the parameters that appear in Equation (6.14) were already presented above, but the logarithm mean temperature that is:

$$\begin{aligned} T_{ml} &= 310.1554\,\mathrm{K} \\ &= 37.0054\,^{\circ}\mathrm{C}. \end{aligned} \tag{6.32}$$

Consequently, the entropy generation resulted in

$$\sigma = 0.0056\,\mathrm{J/K}. \tag{6.33}$$

6.4.5 Exergy analysis

Now, in order to determine the exergy destruction, it is necessary to discover the exergy variation of the flow rate from (6.15). This result indicates an increase in the physical exergy (bearing in mind that this is the objective of the heart).

$$\Delta B = 2.0878\,\mathrm{J}. \tag{6.34}$$

In the following, the exergy associated with the heat exchange between blood at different temperatures T_0, and T_{ml} is

$$B_{QM} = 0.1590\,\mathrm{J}. \tag{6.35}$$

This value indicates the quality of the energy related to heat, therefore, it is the maximum work that is possible to obtain from the metabolic heat transfer. Observe that this amount is one order of magnitude lower than the physical exergy.

Consequently, from the two values above together with the value of metabolism in exergy basis (Expression (6.26)), the left ventricle exergy destruction during a cardiac cycle — calculated using Equation (6.17) — is

$$B_d = 1.6337\,\text{J}. \tag{6.36}$$

Hence, comparing with the result obtained from Equation (6.18):

$$T_0\sigma = 1.6576\,\text{J}. \tag{6.37}$$

The relative error can be calculated:

$$100\left(\frac{B_d - T_0\sigma}{B_d}\right) \approx -1.46\% \tag{6.38}$$

which indicates that these values are very close, as expected.

According to Henriques et al. (2017), the predicted destroyed exergy in the whole cardiovascular system for a healthy individual in basal conditions is 7.86W, while the destroyed exergy only in the heart for the same conditions is 7.53W. Then, it is possible to conclude that at least 25% of the cardiovascular exergy destruction is due to the left ventricle.

Figures 32 and 33 show the Sankey and Grassmann diagrams. The first depicts energy efficiency of the left ventricle: the arrows start from the energy contained in the system to the forms in which it is transformed, while the latter illustrates the exergy diagram for the system: the arrows start from the "available" exergy to its components losses and useful effects. One interesting result is that the destroyed exergy is almost in the same order of magnitude of the heat transfer on an energy basis, indicating that the metabolism is one of the most irreversible processes of the human heart. Moreover, from these diagrams it is possible to define the exergy efficiency.

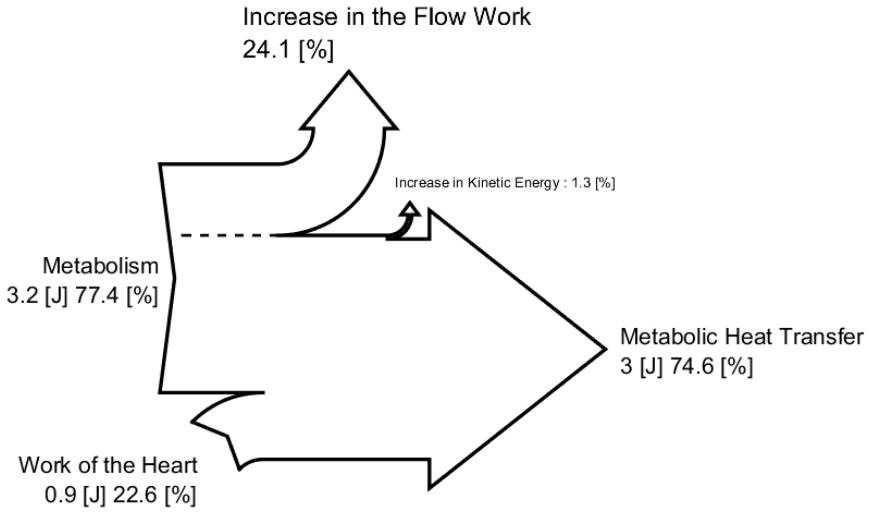

Figure 32 – Sankey diagram.

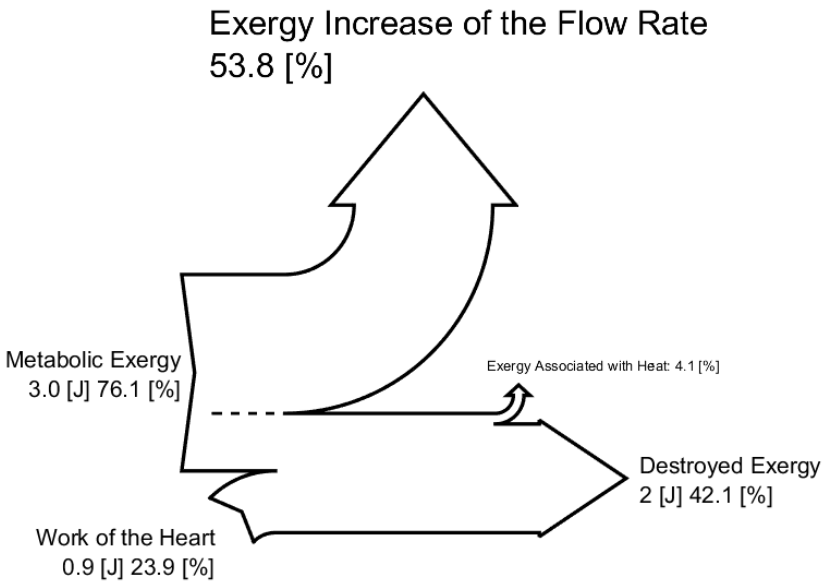

Figure 33 – Grassmann diagram.

Observe that, from the point of view of the First Law, the useful work accounts to less than 30% of the available energy, being approximately 3/4 of the energy reversed in metabolic heat transfer. While the main contributions of exergy in the left ventricle, and consequently in the heart, are the metabolic exergy (B_M)

and the cardiac work (W). Whereas the exergy destruction associated with the usefulness of the heart counts as more than half of the final exergy.

Additionally, Mady e Oliveira (2013) concluded that only 5% of the exergy metabolism is due to thermal portion of metabolism, and the maximum available work from ATP hydrolysis is approximately 60% of exergy metabolism, which assures that our results are consistent.

The efficiencies calculated from Equations (6.19), and (6.20) are, respectively:

$$\eta_1 = 0.7072, \tag{6.39}$$

$$\eta_2 = 0.5790. \tag{6.40}$$

Note that the useful effect from the point of view of exergy (Equations (6.39) and (6.40)) is much larger when compared to the efficiency of 24.1% based on the First Law (Sankey diagram) because the former considers exergy variation of the flow, while the latter only takes into account work divided by the metabolism.

7 Final remarks and conclusions

This dissertation presented bidimensional mathematical and numerical models to represent a heart chamber, specifically, the human left ventricle. To this aim, the blood was assumed to be Newtonian, isotropic, and incompressible. In order to simulate the volume change during a cardiac cycle, it was found necessary to introduce a capacitance function to describe the mass distribution on the domain over time. Then, the final model was governed by a modified version of the incompressible Navier-Stokes equations. They were considered modified because, even though the fluid is incompressible, the equations are similar to the Navier-Stokes equations for compressible fluids: nevertheless, for the sake of simplicity, they are not the same since the constitutive equation was the one for incompressible fluids.

Numerical models of steady-state forms of the Navier-Stokes equations, such as the classical Stokes problem, were presented and evolved to the complete problem. The employed numerical method stands on a Stable Galerkin Mixed Finite Element Method for the Stokes problem (BREZZI; FORTIN, 2012), constructed from the use of quadrilateral elements Q_2P_1. The choice of discontinuous spaces for the pressure assured the conservation of mass between the elements. To reach the optimal convergence in L^2, the global pressure approach was employed, combined with a local one for velocity. The boundary conditions were discussed for each of the cases presented. Some data points were used to describe the variation of pressure and volume with time. The pressure was imposed weakly on the valves of the heart, while the volume variation was prescribed with the capacitance function. The results for the left ventricle, such as velocity in the valves, were consistent when compared to medical data. Moreover, it was possible to extract information to use in the next step, which is the thermodynamic analysis.

Further, a thermodynamic model of a heart chamber that takes into account heat exchanges with the rest of the body was presented. The energy equation was solved in its integral form in order to give a clue of its necessity

in this phenomenological problem. As a closing equation, the Second Law of Thermodynamics and the exergy analysis of the system were also explored in their integral forms. This last one has a prior role in the efficiency analysis of a thermodynamic system. Two efficiencies were proposed. The one based on the First Law of thermodynamics turned out to be around 58%, and the other from the exergy point of view was about 71%.

The thermodynamic results can be more accurate and detailed if the energy conservation and the Second Law of Thermodynamic equations are used in their differential forms. Another improvement in the model could be done using an elastance relation between volume, pressure and time so that the capacitance function would be determined from pressure and time, rather than prescribed. Hence, pressure-volume diagrams could be generated from the use of some pressure measurements over the cycle. Consequently, the exergy analysis could be performed using noninvasive patient-specific data.

Bibliography

American Heart Association. *All About Heart Rate (Pulse)*. 2018. <http://www.heart.org/en/health-topics/high-blood-pressure/the-facts-about-high-blood-pressure/all-about-heart-rate-pulse>. Accessed: 2018-11-15. Citado na página 68.

ANNAMALAI, K.; SILVA, C. Entropy stress and scaling of vital organs over life span based on allometric laws. *Entropy*, Multidisciplinary Digital Publishing Institute, v. 14, n. 12, p. 2550–2577, 2012. Citado na página 83.

ARNOLD, D.; BOFFI, D.; FALK, R. Approximation by quadrilateral finite elements. *Mathematics of computation*, v. 71, n. 239, p. 909–922, 2002. Citado na página 39.

ARNOLD, D. N.; BOFFI, D.; FALK, R.; GASTALDI, L. Finite element approximation on quadrilateral meshes. *Communications in Numerical Methods in Engineering*, Wiley Online Library, v. 17, n. 11, p. 805–812, 2001. Citado na página 36.

ARNOLD, D. N.; BOFFI, D.; FALK, R. S.; GASTALDI, L. Finite element approximation on quadrilateral meshes. *Communications in Numerical Methods in Engineering*, Wiley Online Library, v. 17, n. 11, p. 805–812, 2001. Citado na página 39.

BATATO, M.; BOREL, L.; DERIAZ, O.; JEQUIER, E. Analyse exergétique théorique et expérimentale du corps humain. *entropie: énergétique et dynamique des systèmes complexes: la revue internationale des sciences et techniques en énergétique, génie chimique, génie biologique*, v. 153, n. LENI-ARTICLE-1989-009, p. 1, 1990. Citado 2 vezes nas páginas 20 and 83.

BECKER, E. B.; CAREY, G.; ODEN, J. T. *Finite elements: An introduction*. Austin: Prentice-Hall, 1981. (Texas finite element series). Citado na página 41.

BLICK, E.; STEIN, P. Work of the heart: A general thermodynamics analysis. *Journal of Biomechanics*, Elsevier, v. 10, n. 9, p. 589–595, 1977. Citado 4 vezes nas páginas 11, 17, 18, and 68.

BOFFI, D.; BREZZI, F.; FORTIN, M. *Mixed Finite Element Methods and Applications*. Pavia: Springer Berlin Heidelberg, 2013. (Springer Series in Computational Mathematics). Citado 5 vezes nas páginas 20, 36, 39, 40, and 46.

BOFFI, D.; GASTALDI, L. On the quadrilateral q2–p1 element for the stokes problem. *International Journal for Numerical Methods in Fluids*, Wiley Online Library, v. 39, n. 11, p. 1001–1011, 2002. Citado 4 vezes nas páginas 20, 39, 45, and 46.

BORON, W.; BOULPAEP, E. *Medical Physiology*. [S.l.]: Elsevier Health Sciences, 2012. Citado 4 vezes nas páginas 13, 19, 68, and 69.

BREZZI, F. On the existence, uniqueness and approximation of saddle-point problems arising from lagrangian multipliers. *Revue française d'automatique, informatique, recherche opérationnelle. Analyse numérique*, EDP Sciences, v. 8, n. R2, p. 129–151, 1974. Citado na página 37.

BREZZI, F.; FORTIN, M. *Mixed and hybrid finite element methods*. [S.l.]: Springer Science & Business Media, 2012. v. 15. Citado 4 vezes nas páginas 20, 34, 36, and 95.

CAVAGNA, G.; KANEKO, M. Mechanical work and efficiency in level walking and running. *The Journal of physiology*, Wiley Online Library, v. 268, n. 2, p. 467–481, 1977. Citado na página 81.

CHEN, M. M.; HOLMES, K. R. Microvascular contributions in tissue heat transfer. *Annals of the New York Academy of Sciences*, Wiley Online Library, v. 335, n. 1, p. 137–150, 1980. Citado na página 17.

CIARLET, P. G. *The Finite Element Method for Elliptic Problems*. [S.l.]: North-Holland Publishing Company, 1978. (Studies in Mathematics and its Applications). Citado 2 vezes nas páginas 34 and 36.

CONCEICAO, D. *Balancing Domain Decomposition Preconditioners for Non-symmetric Problems*. Tese (Doutorado) — Instituto Nacional de Matemática Pura e Aplicada, 2006. Citado na página 50.

CORREA, M.; LOULA, A. A unified mixed formulation naturally coupling stokes and darcy flows. *Computer Methods in Applied Mechanics and Engineering*, Elsevier, v. 198, n. 33, p. 2710–2722, 2009. Citado na página 21.

CORREA, M. R. *Métodos de Elementos Finitos Estabilizados para Escoamentos de Darcy e de Stokes-Darcy Acoplados*. Tese (Doutorado) — Laboratório Nacional de Computação Científica, 2006. Citado 2 vezes nas páginas 21 and 33.

DALAND, G. A.; ISAACS, R. Cell respiration studies: Ii. a comparative study of the oxygen consumption of blood from normal individuals and patients with increased leucocyte counts (sepsis; chronic myelogenous leucemia). *The Journal of*

experimental medicine, The Rockefeller University Press, v. 46, n. 1, p. 53, 1927. Citado na página 83.

FERREIRA, M.; YANAGIHARA, J. I. A transient three-dimensional heat transfer model of the human body. *International Communications in Heat and Mass Transfer*, Elsevier, v. 36, n. 7, p. 718–724, 2009. Citado na página 91.

FOUCHET-INCAUX, J. Artificial boundaries and formulations for the incompressible navier–stokes equations: applications to air and blood flows. *SeMA Journal*, Springer, v. 64, n. 1, p. 1–40, 2014. Citado na página 60.

FUNG, Y. C. *Biomechanics: Circulation*. 2. ed. [S.l.]: Springer-Verlag New York, 1997. Citado na página 19.

GAO, H.; WANG, H.; BERRY, C.; LUO, X.; GRIFFITH, B. E. Quasi-static image-based immersed boundary-finite element model of left ventricle under diastolic loading. *International journal for numerical methods in biomedical engineering*, Wiley Online Library, v. 30, n. 11, p. 1199–1222, 2014. Citado 2 vezes nas páginas 19 and 20.

GARCIA, D.; KADEM, L. What do you mean by aortic valve area: geometric orifice area, effective orifice area, or gorlin area? *Journal of Heart Valve Disease*, ICR PUBLISHERS CRISPIN HOUSE, 12/A SOUTH APPROACH, MOOR PARK, NORTHWOOD HA6 2ET, ENGLAND, v. 15, n. 5, p. 601, 2006. Citado na página 29.

GRAVEMEIER, V.; COMERFORD, A.; YOSHIHARA, L.; ISMAIL, M.; WALL, W. A. A novel formulation for neumann inflow boundary conditions in biomechanics. *International Journal for Numerical Methods in Biomedical Engineering*, Wiley Online Library, v. 28, n. 5, p. 560–573, 2012. Citado na página 60.

GUYTON, A.; HALL, J. *Textbook of Medical Physiology*. [S.l.: s.n.], 2006. (Guyton Physiology Series). ISBN 9780808923176. Citado 3 vezes nas páginas 11, 66, and 67.

HALL, J.; GUYTON, A. *Tratado de fisiologia médica*. [S.l.]: Elsevier Brasil, 2011. Citado 4 vezes nas páginas 66, 69, 70, and 83.

HAYNIE, D. T. *Biological thermodynamics*. Cambridge, UK: Cambridge University Press, 2008. Citado na página 82.

HENRIQUES, I.; MADY, C.; JUNIOR, S. O.; ROLL, J. Exergy analysis of the cardiovascular system. In: *Proceedings of the 30th international conference on*

efficiency, cost, optimization, simulation and environmental impact of energy systems. [S.l.: s.n.], 2017. Citado 4 vezes nas páginas 21, 27, 87, and 92.

HENRIQUES, I.; MADY, C.; OLIVEIRA-JUNIOR, S. Exergy model of the human heart. *Energy*, Elsevier, 2016. Citado 4 vezes nas páginas 11, 27, 28, and 81.

HEYWOOD, J. G.; RANNACHER, R.; TUREK, S. Artificial boundaries and flux and pressure conditions for the incompressible navier–stokes equations. *International Journal for Numerical Methods in Fluids*, Wiley Online Library, v. 22, n. 5, p. 325–352, 1996. Citado na página 60.

HUGHES, T. J. R. *The finite element method: linear static and dynamic finite element analysis*. Mineola: [s.n.], 2000. Citado na página 35.

HUO, Y.; KASSAB, G. Governing equations of blood flow and respective numerical methods. *Computational Cardiovascular Mechanics: Modeling and Applications in Heart Failure*, Springer, 2010. Citado na página 28.

JACOBSEN, J. M.; ADELER, P. T.; KIM, W. Y.; HOULIND, K.; PEDERSEN, E. M.; LARSEN, J. K. Evaluation of a 2d model of the left side of the human heart against magnetic resonance velocity mapping. *Cardiovascular Engineering: An International Journal*, Springer, v. 1, n. 2, p. 59–76, 2001. Citado 3 vezes nas páginas 70, 71, and 72.

KOTAS, T. *The exergy method of thermal plant analysis*. [S.l.]: Butterworths, 1985. ISBN 9780408013505. Citado na página 87.

MADY, C.; FERREIRA, M.; YANAGIHARA, J.; SALDIVA, P.; OLIVEIRA-JUNIOR, S. Modeling the exergy behavior of human body. *Energy*, Elsevier, v. 45, n. 1, p. 546–553, 2012. Citado na página 21.

MADY, C.; OLIVEIRA, S. Human body exergy metabolism. *International Journal of Thermodynamics*, v. 16, n. 2, p. 73–80, 2013. Citado 5 vezes nas páginas 20, 21, 82, 83, and 94.

MADY, C. E. K.; OLIVEIRA-JUNIOR, S. Human body exergy metabolism. *International Journal of Thermodynamics (IJoT)*, v. 16, n. 2, p. 73–80, 2013. Citado 2 vezes nas páginas 81 and 83.

MURPHY, M.; O'NEAL, L. *O que é vida? 50 anos depois*. [S.l.]: Unesp, 1997. Citado na página 16.

NEVERS, N. D.; SEADER, J. Lost work: A measure of thermodynamic efficiency. *Energy*, Elsevier, v. 5, n. 8-9, p. 757–769, 1980. Citado 2 vezes nas páginas 87 and 88.

OMRAN, A.; ARIFI, A.; MOHAMED, A. Echocardiography in mitral stenosis. *Journal of the Saudi Heart Association*, Elsevier, v. 23, n. 1, p. 51–58, 2011. Citado na página 29.

OTTESEN, J.; OLUFSEN, M.; LARSEN, J. *Applied Mathematical Model in Human Physiology*. [S.l.: s.n.], 2004. v. 405. Citado 6 vezes nas páginas 19, 27, 28, 70, 72, and 73.

PENNES, H. H. Analysis of tissue and arterial blood temperatures in the resting human forearm. *Journal of applied physiology*, v. 1, n. 2, p. 93–122, 1948. Citado na página 16.

PESKIN, C. S. The immersed boundary method. *Acta numerica*, Cambridge University Press, v. 11, p. 479–517, 2002. Citado 2 vezes nas páginas 19 and 20.

PRIGOGINE, I.; WIAME, J.-M. Biologie et thermodynamique des phénomènes irréversibles. *Experientia*, Springer, v. 2, n. 11, p. 451–453, 1946. Citado na página 16.

SALTZMAN, W. *Biomedical Engineering: Bridging Medicine and Technology*. [S.l.]: Cambridge University Press, 2009. (Cambridge Texts in Biomedical Engineering). Citado na página 27.

SMITH, N. P.; BARCLAY, C. J.; LOISELLE, D. S. The efficiency of muscle contraction. *Progress in biophysics and molecular biology*, Elsevier, v. 88, n. 1, p. 1–58, 2005. Citado na página 81.

STEENDIJK, P.; ELLEN, A. Invasive assessment of cardiac efficiency. *Heart and metabolism*, Servier, n. 39, p. 33–36, 2008. Citado 2 vezes nas páginas 12 and 84.

SZARGUT, J. Exergy analysis. *The Magazine of Polish Academy of Sciences*, v. 3, n. 7, p. 31–33, 2005. Citado na página 18.

TAKAOKA, H.; TAKEUCHI, M.; ODAKE, M.; YOKOYAMA, M. Assessment of myocardial oxygen consumption (vo2) and systolic pressure–volume area (pva) in human hearts. *European heart journal*, Oxford University Press, v. 13, n. suppl_E, p. 85–90, 1992. Citado na página 83.

WERNER, J.; BUSE, M. Temperature profiles with respect to inhomogeneity and geometry of the human body. *Journal of Applied Physiology*, v. 65, n. 3, p. 1110–1118, 1988. Citado 2 vezes nas páginas 68 and 86.

WHITE, F. *Fluid Mechanics*. [S.l.]: McGraw Hill, 2011. (McGraw-Hill series in mechanical engineering). ISBN 9780073529349. Citado na página 48.

APPENDIX A – Implementation details

The program was implemented in Fortran 90 using data structure. The number of nodes of each element can be chosen by means of the variable m, which, consequently, determines the element type, generated mesh, basis functions, array dimensions, matrix band, etc. The boundary conditions were inserted into the local matrices and load vectors. An *assemble* routine has coupled the local arrays and vectors into a global system. By means of the physical interpretation of the problem and the finite element bases used, it is possible to verify that the coefficient matrix is in a band-form. Thus, the solver `dgbsv` was used — which is based on the LU factorization and is suitable for this type of linear system — available in *Linear Algebra PACKage* (LAPACK). Regarding the integrals used to find the array's entries, the Gaussian quadrature scheme was used.